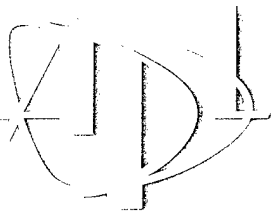


High-Frequency Acoustic Volume Scattering from Biologically Active Marine Sediments

by Christopher D. Jones

Technical Report
APL-UW TR 9903
October 1999



Applied Physics Laboratory - University of Washington
Seattle, Washington 98109-6698

DTIC QUALITY INSPECTED 2

19991213 088

Approved for public release; distribution is unlimited.

High-Frequency Acoustic Volume Scattering from Biologically Active Marine Sediments

by Christopher D. Jones

Technical Report
APL-UW TR 9903
October 1999



Applied Physics Laboratory University of Washington
1013 NE 40th Street Seattle, Washington 98105-6698

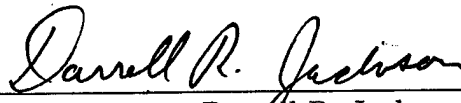
University of Washington
Graduate School

This is to certify that I have examined this copy of a doctoral dissertation by

Christopher D. Jones

and have found that it is complete and satisfactory in all respects,
and that any and all revisions required by the final
examining committee have been made.

Chair of Supervisory Committee:



Darrell R. Jackson

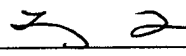
Reading Committee:



Peter A. Jumars



Eric I. Thorsos



Leung Tsang

Date: _____

6/11/99

FOREWARD

This report is a slightly revised version of the dissertation submitted in partial fulfillment of the requirements for the Doctor of Philosophy degree at the University of Washington in June 1999. Dr. Darrell R. Jackson was the chair of the supervisory committee.

University of Washington

Abstract

High-Frequency Acoustic Volume Scattering from
Biologically Active Marine Sediments

by Christopher D. Jones

Chair of Supervisory Committee

Professor Darrell R. Jackson
Electrical Engineering

A thesis on high-frequency acoustic volume scattering from marine sediments with application to remote sensing of benthic biological activity is presented. Small perturbation theory is used to describe bistatic volume scattering in a sediment half-space. The sediment is modeled as an acoustic fluid with random fluctuations in density and compressibility. Insight into determining whether single or multiple scattering is significant in the medium is gained by using the bilocal approximation to Dyson's equation. An alternative analysis of volume scattering is made using exact numerical simulations, and a numerical method for two-dimensional volume scattering using the method of moments is presented. Both periodic and nonperiodic random media are considered. Scattering theory is compared with numerical Monte-Carlo simulations, and the validity of the small perturbation method is discussed. The effects of the half-space scattering geometry on the coherent field within the sediment and on the bistatic scattering cross-section are investigated.

Benthic biological activity creates temporal and spatial variations in the sediment physical properties that result in temporal and spatial variations in sediment

volume scattering. This acoustic variability is used as a remote sensing tool to infer parameters of biological activity, or bioturbation. To develop a forward model that relates bioturbation to density fluctuations in the sediment and, therefore, to acoustic scattering, a new stochastic model of bioturbation is presented that describes biological mixing as an inhomogeneous (two scale) biodiffusion process. Nonlocal mixing (due to macrofauna) is described as a filtered Poisson process, and local mixing (due to meiofauna) is described as diffusive. Modeling issues such as the spatial stationarity of bioturbation are discussed.

The bioturbation and acoustic scattering models are then combined to produce a model for the decorrelation in time of acoustic backscatter. Model predictions are compared with experimental data collected over a two month period during the Orcas Island experiment. The observed decorrelation of acoustic backscattering from the sediment at the Orcas site is compared to model predictions of temporal decorrelation, and the feasibility of using acoustic remote sensing to detect and study benthic biological activity is discussed.

TABLE OF CONTENTS

List of Figures	iv
Glossary	ix
Chapter 1: Introduction	1
1.1 Volume Scattering in Sediment	4
1.2 Benthic Biological Activity	7
Chapter 2: Sediment Volume Scattering	14
2.1 Sediment Physical Properties	16
2.2 Volume Scattering Integral Equation	21
2.3 Small Perturbation Method	25
2.4 Temporal and Spatial Correlation of the Scattered Field	32
2.5 Scattering Cross-Section	35
2.6 Scattering of a Narrow Band Pulse	38
2.7 Volume Scattering from a Periodic Random Medium	43
Chapter 3: Numerical Methods for Volume Scattering	48
3.1 Method of Moments	50
3.2 Discretization and Selection of Basis/Testing Functions	53
3.3 Monte-Carlo Simulations	63
3.4 Summary and Conclusions	74

Chapter 4: Validity of the Small Perturbation Method	77
4.1 Multiple Scattering Theory	78
4.2 A Comparison with Numerical Methods	91
4.3 Summary and Conclusions	98
Chapter 5: Biological Sources of Heterogeneity in Sediments	103
5.1 Mixing of Sediments by Benthic Organisms	104
5.2 Classical Diagenetic Models	105
5.3 Inhomogeneous Biodiffusion of Sediment Bulk Properties	112
5.4 Spectrum of a Biodiffusional Process	128
5.5 Inhomogeneous Biodiffusion of Sediment Microtopography	130
5.6 Summary and Conclusions	132
Chapter 6: Remote Sensing of Benthic Activity	134
6.1 Forward Model of Scattering	135
6.2 Inverse Model of Scattering	137
6.3 Orcas Island Experiment	141
6.4 Summary and Conclusions	149
Bibliography	152
Appendix A: Half-Space Green's Function	163
Appendix B: Far-field Half-Space Green's Function	166
Appendix C: Auto-Regressive Spectral Estimation	169
Appendix D: FFT Evaluation of the Half-Space Green's Function	171
Appendix E: Generating Gaussian Random Media	173

LIST OF FIGURES

1.1	Examples of benthic epifauna and infauna that create bioturbation in marine sediments (from Berner 1980)	8
1.2	Examples of sediment X-radiographs of cores that show volume heterogeneity created by benthic organisms (from R. Wheatcroft)	9
1.3	Decorrelation of the backscattered field due to biological activity at various shallow water locations.	11
1.4	Spectrum of the equivalent spherical diameter body size of benthic organisms in marine sediments (from Jumars 1993).	12
2.1	Geometry for volume scattering from a half-space random medium.	15
2.2	Composition of marine sediment near sediment-water interface.	16
2.3	Small perturbation method for volume scattering from a random half-space: (a) first-order scattering; (b) second-order scattering.	30
2.4	Half-space windowing in the difference coordinates.	33
2.5	Scattering of a pulse of duration T_0 from a random half-space.	42
3.1	Simulation of volume scattering in a non-periodic medium: (a) The tapered incident field $ p_0(x, z) $; (b) a realization of a Gaussian random medium $\gamma_p(x, z)$; and (c) the solution for the total scattered field $ p(x, z) $. The incident field is above critical at $\theta_i = 35^\circ$, $l_c = 0.5\lambda$, $\sigma_p = 0.10$, $\mu = -1.1$, $\bar{\rho}/\rho_0 = 2.0$, $\bar{c}/c_0 = 1.1$, $\delta = 0.02$, with 10 points per wavelength. All coordinates are normalized by the wavelength.	66

3.2	Simulation of volume scattering in a periodic medium: (a) The plane incident field $ p_0(x, z) $; (b) a realization of a Gaussian random medium $\gamma_\rho(x, z)$; and (c) the solution for the total scattered field $ p(x, z) $. The incident field is subcritical at $\theta_i = 20^\circ$, $l_c = 1.0\lambda$, $\sigma_\rho = 0.10$, $\mu = -2.0$, $\bar{\rho}/\rho_0 = 2.0$, $\bar{c}/c_0 = 1.1$, $\delta = 0.02$, with 10 points per wavelength. All coordinates are normalized by the wavelength.	67
3.3	Monte-Carlo convergence with respect to: (a) the number of points per wavelength; and (b) the size of the medium. The symbol * represents $l_c = 0.2\lambda$, the o represents $l_c = 0.5\lambda$, and the \times represents $l_c = 1.0\lambda$. A total of 50 realizations was used to estimate the ensemble average.	70
3.4	Monte-Carlo convergence with respect to the number of realizations ($N_x\lambda/L_x = 10$ and $L_x/\lambda = 6.4$).	71
3.5	Fields within a half-space medium with a linear wavenumber profile ($\bar{c}/c_0 = 1.2$, $\bar{\rho}/\rho_0 = 2.0$, $a = -0.05$, $b = 0.1$) for a tapered incident field: (a) Contour plot of magnitude of the tapered field MoM solution; (b) Real component of the MoM solution (stepped curve) compared with the analytic solution (solid curve) and the incident field (dashed curve); (c) Imaginary components of the solutions. . . .	72
3.6	Fields within a half-space medium with a linear wavenumber profile ($\bar{c}/c_0 = 1.2$, $\bar{\rho}/\rho_0 = 2.0$, $a = -0.05$, $b = 0.1$) for a periodic medium and plane wave incident field: (a) Real components of the MoM solution (stepped curve) compared with the analytic solution (solid curve) and the incident field (dashed curve); (b) Imaginary components of the solutions.	73

3.7	Comparisons of MoM solutions for the volume scattering strength found using the iterative SPM method and the exact matrix inversion method. The circles (o) are the exact solutions, and the solid dots (·) are the SPM solutions including terms up the specified order: (a) second-order SPM using (2.82); (b) third-order SPM using (2.84); (c) fourth-order SPM using (2.86); and (4) fifth-order SPM. The incident field is subcritical at $\theta_i = 10^\circ$, $l_c = 1.0\lambda$, $\sigma_\rho = 0.10$, $\mu = -2.0$, $\bar{\rho}/\rho_0 = 2.0$, $\bar{c}/c_0 = 1.1$, $\delta = 0.02$, with 10 points per wavelength. . . .	75
4.1	Contours of γ'_e as a function of l_c/λ , μ , and α_λ . All contours are calculated with $\sigma_\rho^2 = 0.01$ using (4.31).	89
4.2	Contours of γ''_e as a function of l_c/λ , μ , and α_λ . Solid contours are found using a perturbation method, and the dashed contours are found numerically. All contours are calculated with $\sigma_\rho^2 = 0.01$	90
4.3	First-order multiple scattering compared to the bilocal approximation: Contours of γ''_e as a function of l_c/λ , μ , and α_λ . The solid contour lines are found using first-order multiple scattering, the dashed contours (nearly hidden below the solid contours) are found using the bilocal approximation with a small variance. All contours are calculated with $\sigma_\rho^2 = 0.01$	92
4.4	Cases for which effective wavenumber are estimated. $\rho/\rho_0 = 2.0$, $c/c_0 = 1.2$, $\alpha_\lambda = 1.0$, $\sigma_\rho^2 = 0.01$	94

4.5	The magnitude of: (a) the incident field; (b) the mean field; and (c) the horizontally averaged real components of the incident field (dashed line) and mean field (solid line) within the scattering volume of a periodic medium. Sediment parameters correspond to case <i>B</i> in Figure 4.4. The incident field is normal to the interface at $z = 0$. All coordinates are normalized by the wavelength.	95
4.6	Estimate of γ_e'' as a function of depth for different values of μ and l_c/λ defined in Figure 4.4.	97
4.7	Bistatic scattering strength for various angles of incidence for case <i>B</i> of Figure 4.4. Critical angle of 24.6°	99
4.8	Contours of γ_e'' for several sites. The * indicates the values of l_c/λ and μ estimated from core data at each site. Eckernfoerde: $\alpha_\lambda = 0.1, \sigma_\rho = 0.01$, Panama City: $\alpha_\lambda = 0.9, \sigma_\rho = 0.03$, Key West: $\alpha_\lambda = 0.5, \sigma_\rho = 0.045$, Orcas: $\alpha_\lambda = 0.1, \sigma_\rho = 0.045$	100
5.1	Local and non-local mixing between layers of sediment.	109
5.2	Discrete nonlocal mixing between two layered regions of sediment. Sediment is removed from a volume defined by the sink function h and deposited in a volume defined by the source function g	115
5.3	Examples of cylindrical and spheroidal source/sink shape functions that represent idealized nonlocal mixing of macrofauna: (a) head-down deposit feeding; (b) burrow hole infilling; and (c) arbitrary movements of sediment.	118
5.4	Spherical shape functions that are homogeneously distributed in the horizontal (a) and nonhomogeneously distributed in depth (b). The Poisson point density in space and time decreases with depth, concentrating activity near the sediment-water interface.	119

6.1	Spherical shape functions that are: (a) homogeneously distributed in the horizontal; and (b) nonhomogeneously distributed in depth. The Poisson point density in space and time decreases exponentially with depth with a scale defined by the rework depth L , concentrating activity near the sediment-water interface.	141
6.2	Scattering geometry of Orcas experiment. The shaded area is a radial scan for a single pulse transmission.	143
6.3	Spatial variability in (a) the mean backscatter strength, and (b) the variance of the backscatter strength at the Orcas site. Data estimated from 50 consecutive scans using 40 kHz backscatter, and plotted on a uniform grid with 1.5 meter spacing.	144
6.4	Comparison of measured backscatter with model predictions for the Orcas site.	147
6.5	Sound speed fluctuations in the water during the Orcas experiment. .	148
6.6	Comparison of measured backscatter correlation and model predictions, (a) $\theta = 14.7^\circ$, (b) $\theta = 9.4^\circ$, (c) $\theta = 7.6^\circ$, (d) $\theta = 6^\circ$	150
B.1	Complex contour in the θ plane.	167

GLOSSARY

BENTHIC: Pertaining to the bottom of the sea or lake.

EPIFAUNA: Benthic organisms that live on the surface of the sediment-water interface.

INFAUNA: Benthic organisms that live within the sediment.

MACROFAUNA: Benthic organisms that fall with the size category of approximately 1 cm and larger.

MEIOFAUNA: Benthic organisms that fall within the size category of approximately 0.00001 to 0.001 meters.

DIAGENESIS: The sum total of processes that bring about change in a sediment or sedimentary rock subsequent to deposition in water.

BIOTURBATION: The mixing of sediment by the activities of benthic organisms.

EGESTION: To discharge or excrete from the body.

SURFICIAL: On the surface of the sediment

PLANKTON: Plant and animal organisms, generally microscopic, that float or drift in great numbers in salt and fresh water.

NEKTON: The total population of marine animal organisms that swim independently of currents ranging in size from microscopic to large.

STRATIGRAPHY: The study of rock or sediment strata

DEDICATION

To Soula and my son Stefan for their endless support, patience, and motivation.

In memory of Julia Jones.

ACKNOWLEDGMENTS

The author wishes to express sincere appreciation to Darrell Jackson, Pete Jumar, Eric Thorsos, and Leung Tsang for helpful comments, guidance, and input. Special appreciation is given to Darrell Jackson for his creative input and careful review. The author also wishes to express appreciation to DJ Tang, Kevin Williams, Dan Rouseff, and many other individuals at APL/UW for their many helpful discussions and ideas. This work was supported by ONR.

Chapter 1

INTRODUCTION

Acoustic wave propagation and scattering have been widely used to study processes and detect objects in the ocean. The principal reasons are the desire to monitor and collect environmental data over a large area and the limited usefulness of optical and electromagnetic wave propagation underwater. For a wide range of scientific and engineering problems dealing with the ocean environment, acoustic wave propagation and scattering is the only remote sensing technology available.

The ocean, however, is a highly stochastic environment. For many practical applications of underwater acoustics, there is inadequate oceanographic information about the spatial and temporal variability in the medium to adequately model acoustic propagation and scattering. In some cases, even the mechanisms by which sound is scattered are not well understood and must be highly idealized. The problem is further complicated by the low frequency and phase velocity of acoustic waves (relative to electromagnetic waves). In many cases, the ocean environment fluctuates on spatial scales comparable to the acoustic wavelength, especially at higher frequencies. Consequently, the modeling of underwater acoustics for high-frequency remote sensing in the ocean is inherently linked to stochastic modeling of ocean processes that affect propagation and scattering.

In general, there are two very different reasons for studying acoustic interaction with the ocean environment. One reason is to remove the negative effects of the random environment on acoustic systems, such as underwater communication de-

vices and object detection sonars. The goal of understanding the environment is to provide better forward models of propagation and scattering that can be used to improve the systems' performance. The other reason is to facilitate the use of acoustics as a remote sensing tool for studying the ocean environment. A comprehensive understanding of the physics of scattering in the ocean will lead to improved inverse models of scattering and propagation. With reliable acoustic models, over a range of frequencies, underwater acoustics can be used to study the ocean on spatial and temporal scales that are unattainable using other technologies.

Some aspects of the ocean acoustics problem have been investigated for many years, especially low frequency propagation in the deep water environment. In recent years, considerable attention has focused on coastal environments and shallow water processes, and the use of high frequency acoustics in the 10-500 kHz range. Propagation and scattering at these frequencies are sensitive to small-scale ocean processes including: air-sea interactions that create bubbles and surface roughness; internal wave structures and turbulence that create index of refraction fluctuations in the water column; and biological and hydrodynamic processes in the water and sediment. Seafloor processes, such as bioturbation and sediment transport, create sediment-water interface roughness and sediment volume heterogeneity.

The topic of this thesis is the use of high-frequency acoustic volume scattering in marine sediments as a remote sensing tool. Two issues in seafloor scattering will be addressed in detail: 1) the more general issue of modeling volume scattering from the seafloor; and 2) the specific application of acoustic remote sensing of biological processes in the seafloor - in particular, the biological processes that create spatial and temporal variability in the volume of the sediment. The second chapter of this thesis will address the problem of modeling acoustic volume scattering from a fluid half-space random medium. Half-space refers to the geometry created by the discrete interface between the sediment and the overlaying water. The small perturbation method will be used to formulate analytic expressions for the first and

second moments of the scattered field due to a time-harmonic (CW) excitation.

In chapter three, a numerical method for volume scattering from a fluid half-space will be presented. The numerical solutions are exact in that they attempt to solve the complete integral equation formulation of the problem, including attenuation in the medium, multiple scattering, and half-space effects. Approximations to the wave solution are only numerical. With increased computational resources, the numerical solution will improve and approach the exact solution.

Statistical parameters such as the scattering cross section and field correlation are found by generating random realizations of sediment heterogeneity and performing Monte-Carlo simulations of the scattered field. Only the time harmonic (CW) solution is considered. Numerical results will be presented, and the computational problems and convergence issues associated with performing exact two-dimensional calculations of volume scattering will be discussed.

In chapter four, the validity of the small perturbation method for scattering from typical sediments will be discussed. Multiple scattering theory, in the context of the bilocal approximation to Dyson's equation, will be used to investigate scattering due to density and compressibility fluctuation. Numerical simulations (guided by the multiple scattering theory) will also be used to investigate multiple scattering and half-space effects. Numerical results will be compared with the perturbation solution, and inferences will be drawn as to when the approximations are valid.

The last two chapters (five and six) comprise the second issue of this thesis: an application of sediment volume scattering to the remote sensing of benthic biological activity. In chapter five, a new stochastic model of bioturbation is presented in which the spatial and temporal fluctuations of sediment physical properties are related to biological activity. Existing models of sediment diagenesis are reviewed and the mechanisms by which biological activity creates sediment heterogeneity are discussed. Then, in chapter six, a model of acoustic scattering due to bioturbation is discussed. By coupling the sediment bioturbation model with the scattering model,

a model for the decorrelation in time of the scattered field due to biological activity is developed. This model is then compared with acoustic field data and sediment physical data obtained in a biologically active shallow-water environment.

1.1 Volume Scattering in Sediment

An acoustic field incident upon a random medium will interact with heterogeneities within the volume to create a scattered field. The solution for the volume scattered field begins by examining the scales and interrelationships between various parameters of the problem at hand. The most essential of these parameters are: 1) the magnitude of the random physical properties of the medium that give rise to scattering; 2) the characteristic length scales of the randomness in the medium relative to the wavelength of the incident field; and 3) the absorption in the medium which defines the characteristic distance over which scattering occurs. Typically, some type of analytic or heuristic criterion is applied to these parameters, and a solution strategy is chosen.

There are two general approaches to the solution of wave scattering in a random medium: analytic theory and radiative transport theory. Analytic wave scattering theories are solution methodologies applied directly to the wave equation for the field quantity of interest. They can be broadly categorized as either *single* or *multiple* scattering theories. Radiative transport theory is based on phenomenological observations of the transport characteristics of the wave field intensity [17, 30]. The relationship between transport theory and multiple scattering theory has been well established [80, 30]. However, this thesis will focus mainly on analytical approaches to random medium scattering, and attention will be given to the criteria for determining which type of analytic solution methodology is applicable to sediment volume scattering.

A single (or weak) scattering medium is one in which the total perturbations

experienced by the incident field are small, and single scattering dominates the scattered field. Weak scattering methods can provide analytical solutions to problems where general solutions are not attainable. They can also provide intuition into the scattering phenomena. First-order perturbation methods, such as the Born and Rytov approximations, are classical examples of weak scattering methods.

Multiple scattering occurs if the perturbation of the incident field by the medium is comparable to the incident field itself and there is scattering between the differential elements of the volume. Higher-order perturbation methods can be used to provide insight into multiple scattering. In general, however, they are complicated and are difficult to extend to higher moment solutions of the scattered field. Effective medium theories can be used to define renormalized parameters of the medium that account for multiple scattering. For example, Dyson's equation describes the coherent (mean) field within a scattering medium. It can be used to define a complex effective wavenumber, where the wave speed and attenuation include the effects of multiple scattering [10, 75]. However, effective medium methods are also difficult to extend to higher moments and in general do not provide analytic solutions for interesting problems.

Single scattering approximations are used in many ocean acoustics applications. For volume scattering from marine sediments, the Born approximation is widely assumed [34, 26, 88]. However, the validity of the weak scattering assumption for typical marine sediments is not well established. Typically, sediment core sampling [13, 34] or *in situ* analyses [74, 87] are used to estimate density and sound speed fluctuations in the sediment. The measured sediment fluctuations are then used to estimate backscatter strength using single scattering models.

Experimentally measured backscatter strengths have been compared with the predictions of first-order perturbation models for volume scattering [34]. Some data show reasonable agreement with models, within the confidence limits of the estimated sediment parameters used as inputs to the models. However, the results are

inconclusive. No attempt is made to investigate half-space effects or higher-order scattering effects. The disagreements in model-data comparisons are attributed to errors and resolution problems associated with the core analysis and the spectral estimation of the sediment fluctuations. Comprehensive ground-truth measurements of sediment volume heterogeneity in a wide variety of environments are not yet available.

In contrast, scattering from the sediment-water and air-water interface in the ocean has been studied in detail and the parameter space of validity determined [76, 77]. It is well established that small perturbation methods for sediment interface roughness scattering are not always applicable for the range of acoustic frequencies, grazing angles, and interface statistics encountered in the ocean. In general, a variety of surface scattering models (e.g., perturbation, tangent-plane, small-slope methods) are applied depending on the particular merits of the method and the characteristics of the surface roughness [37, 15]. Much of this evaluation was done in comparison with exact numerical solutions, the most common calculation being the computation of the scattering integral equation of an idealized one-dimensional rough surface by quadrature methods [76, 77]. More recently, efficient numerical techniques have been extended to the solution of the full three-dimensional surface problem, [78] and [22] for example.

This thesis will address the validity of small perturbation methods for volume scattering in marine sediments (where the magnitudes of the medium fluctuations are the small parameters). Insight into determining whether single or multiple scattering is significant in the sediment will be gained by using classical multiple scattering theory. Effective medium theory using the bilocal approximation to Dyson's equation will be extended to include density fluctuation (analogous with including permeability fluctuation in the EM case). An alternative analysis (guided by the results of the multiple scattering theory) will be made using "exact" numerical simulations of the scattered field. By comparing solutions of the perturbation method

with the numerical solutions, the range of validity of the perturbation methods for typical sediments can be inferred. Parameters of the sediment are limited to those of typical marine sands and muds modeled as acoustic fluid half-spaces with Gaussian random fluctuations in density and compressibility.

Numerical simulations will be limited to the solution of the volume integral equation in two dimensions and for a single frequency using the method of moments [24]. Moment methods are commonly applied to electromagnetic scattering problems (see [18] and [57] for an overview). Other solution techniques such as finite-volume methods, finite-difference and finite element methods are also applied to wave propagation and scattering (also see [57] for an overview of these and other methods). The numerical integral equation formulation provides one obvious advantage: it is the most direct and analogous solution methodology for comparison with the perturbation results. By treating the scattering integral as a matrix equation, the convergence properties of the perturbation expansion can be studied by examining the convergence properties of the solution of the matrix equation.

1.2 Benthic Biological Activity

Biologically active sediments are continually modified by epifauna and infauna. Epifauna are organisms that live on the sediment surface, and infauna are organisms living within the sediment. The collective mixing effect of these organisms is termed bioturbation. Interests in bioturbation range from applications in marine engineering to biological oceanography including the time evolution of acoustic and structural properties of seafloor sediments, and the monitoring of the effects of pollutants or other disturbances on benthic ecology. Biological interests include diagenesis in marine sediments, the study of sediment disturbance processes, deposit-feeding levels, and population dynamics, for example.

Observations of the influence of benthic biology on sediment heterogeneity are

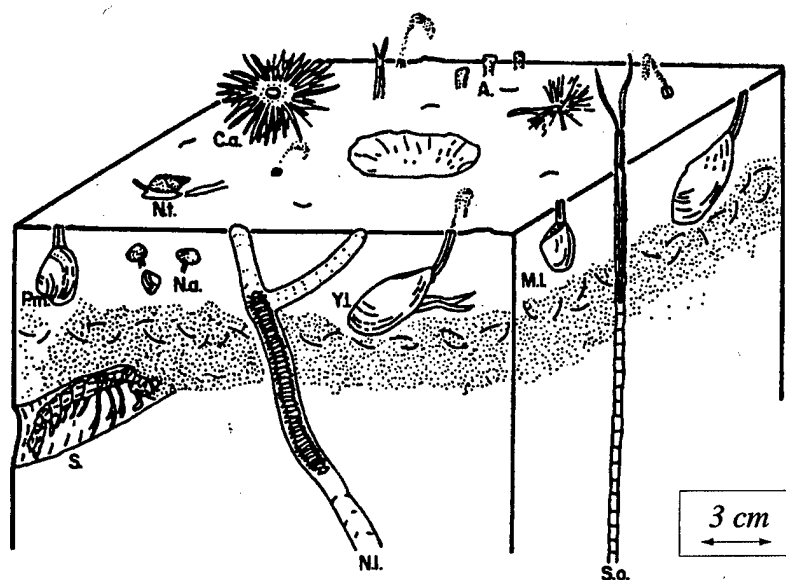


Figure 1.1: Examples of benthic epifauna and infauna that create bioturbation in marine sediments (from Berner 1980)

numerous. An overview of this topic can be found in texts on the subject [4, 40, 46] and in review articles with extensive bibliographies [56], for example. Figure 1.1 illustrates typical organisms of interest in this development. Sediment x-ray cores reveal the structure of density fluctuations (through x-ray absorption) within the volume of the sediment. Figure 1.2 shows several examples of typical X-radiographs taken in biologically active sediments. The imagery shows typical burrows and inclusions due to biological activity. These illustrations and images also clarify the spatial scales of scattering that are of primary interest in this thesis. The acoustic wavelength for frequencies of interest (10-500 kHz @@ 1500 m/s) is comparable to the scale of the heterogeneity created by biological processes.

Acoustic observations of benthic biological activity are also numerous, although

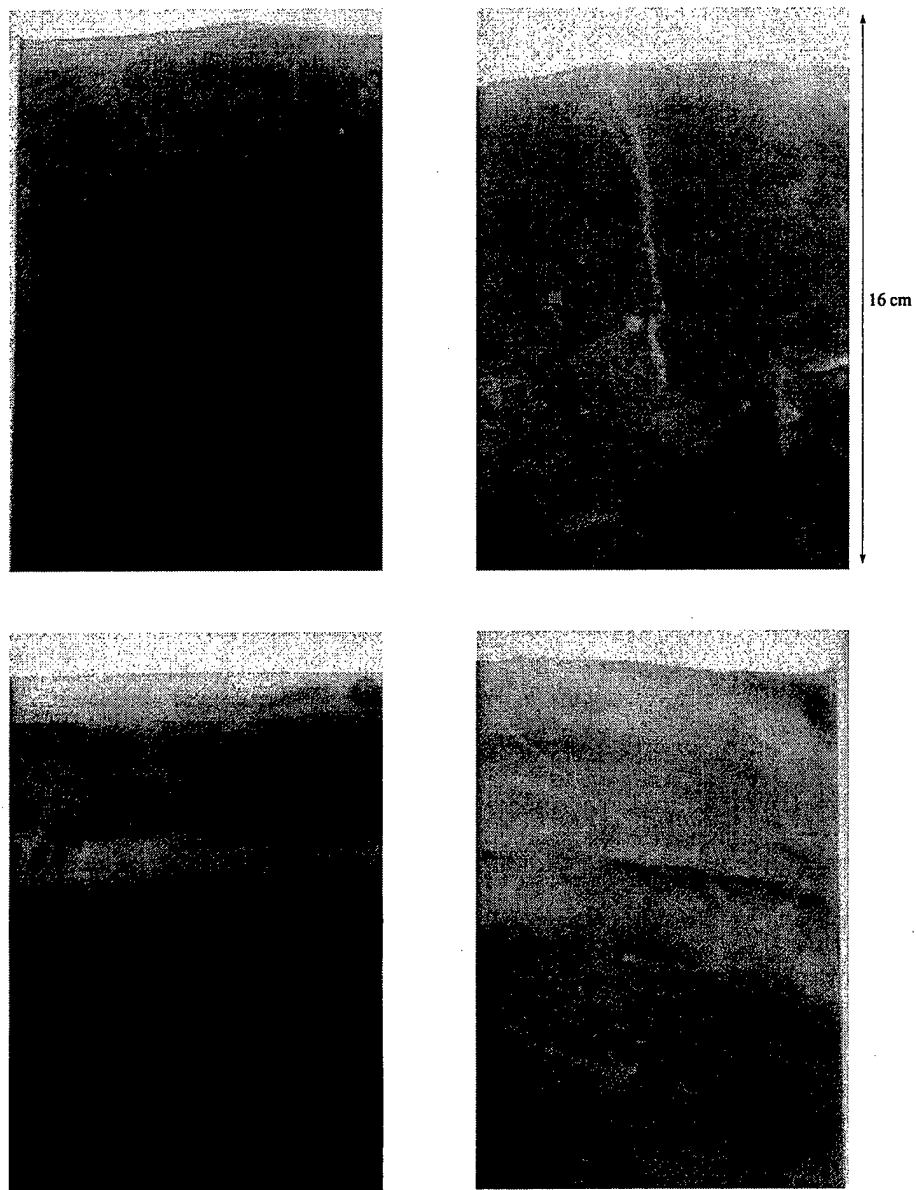


Figure 1.2: Examples of sediment X-radiographs of cores that show volume heterogeneity created by benthic organisms (from R. Wheatcroft)

the observations are not generally investigated for the purpose of understanding the biota. Of particular interest are recent experiments in which observations of sediment backscatter were made over a period of months in a variety of shallow-water environments and sediment types [20, 36, 41, 86]. The spatial and temporal evolution of scattering from the seafloor (at 40 and 300 kHz) has been attributed to biological reworking of sediment microtopography, sediment volume heterogeneity, and near-bottom volume reverberation. The correlation in time of the backscattered field shows characteristic decay that is most likely a function of the type and rate of biological activity associated with the different environments (see Figure 1.3). During the Orcas experiment, changes in the acoustic signatures of buried objects over time were observed [86]. Biological activity around the buried objects decreased the object's total scattering strength in time. During the same time period, the temporal correlation of backscatter from the area of the object showed increased decorrelation - most likely due to increased biological activity around the object.

On micro- and macroscopic scales, bioturbation affects the physical and chemical properties of the sediment. The intensity of bioturbation affects the distribution of marine chemicals which, in turn, influence the microbial activity in the sediment and the ultimate fate of marine pollutants [1, 4, 40, 83]. Epifaunal activity creates microtopography that may decrease the critical velocity necessary to erode surface layers [84]. Infaunal activity, such as tube building, is responsible for vertical and horizontal redistribution of solid material within the sediment, creating spatial and temporal heterogeneity in sediment porosity [6, 7] which leads to heterogeneity in the sediment bulk density and compressibility. Often, the traces of these mixing activities provide the only evidence of the existence of fauna in an area and may provide a measure of benthic biomass [84].

Bioturbation is pervasive and shows similar spatial characteristics across a wide variety of marine environments. The effective biological mixing depth (based on a variety of measurement methods) has a worldwide mean of approximately 10 cm

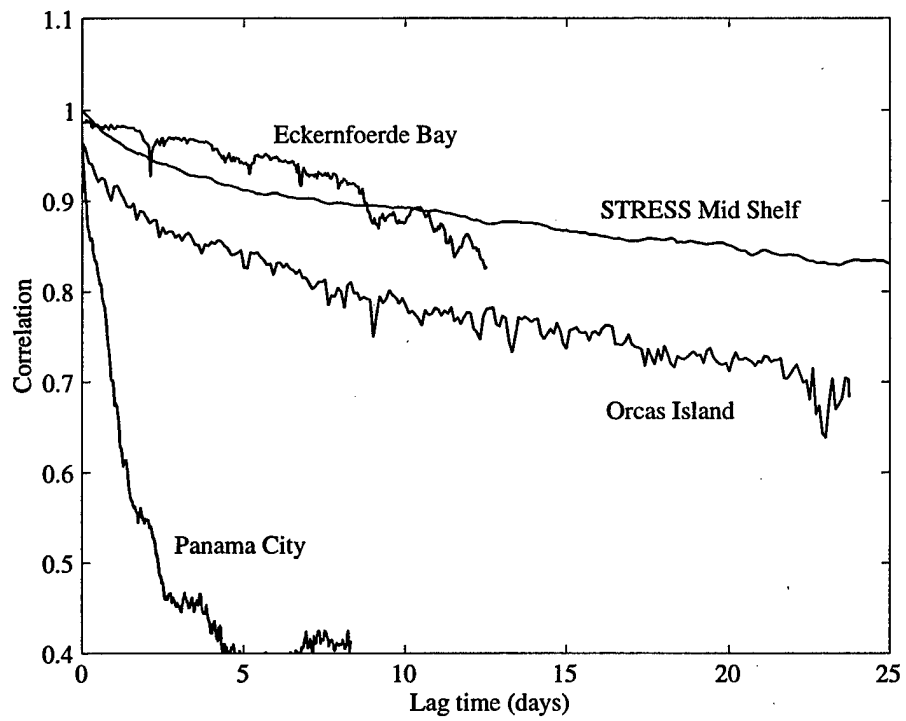


Figure 1.3: Decorrelation of the backscattered field due to biological activity at various shallow water locations.

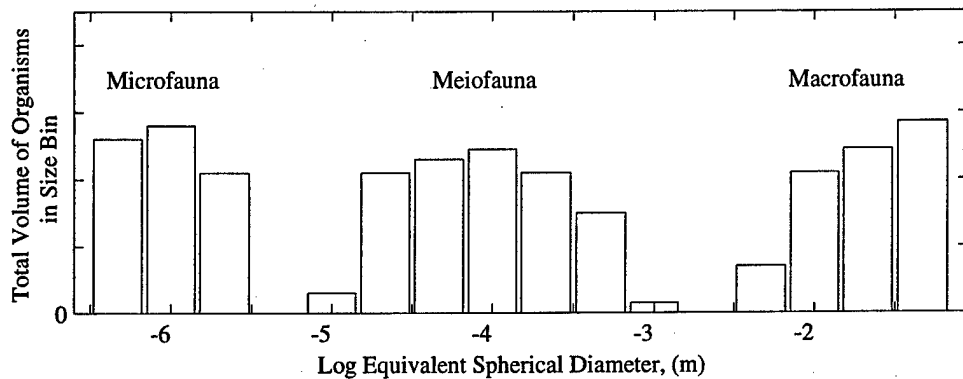


Figure 1.4: Spectrum of the equivalent spherical diameter body size of benthic organisms in marine sediments (from Jumars 1993).

[40]. In addition, the body size spectra of benthic organisms show characteristic tri-modal structure, rather than a flat spectrum observed for organisms in the ocean water column [40]. Figure 1.4 shows the typical size-abundance relationship for organisms in marine sediments. In both shallow water and deep sea sediments, there are minima in the body size spectra at about $10\ \mu\text{m}$ and $1\ \text{mm}$. In general, meiofauna collectively outweigh macrofauna, with animal and bacterial abundance declining exponentially as a function of depth into the sediment [40].

This brief introduction is given mainly to motivate interest in bioturbation from a remote sensing point of view, not as a comprehensive review of the topic. The subject of bioturbation in marine sediments is far beyond the scope and intent of this thesis. However, because one of the objects for this thesis is to address the remote sensing problem, a forward model of bioturbational mixing must be developed. The forward model in this case is a quantitative description of mixing that can relate biological parameters to acoustically detectable changes in the physical properties of the sediment. A certain level of detailed description of the biological processes is necessary, therefore, to justify the proposed modeling methodology. Furthermore, since the mixing model is used as the critical link between the observation

of sound scattered from the sediment and the estimation of parameters that describe the sediment biology, it should incorporate established variables and concepts used by benthic biologists. In addition, the mixing model should provide the physical reasoning that relates these parameters to the modeling of sound scattering.

Chapter 2

SEDIMENT VOLUME SCATTERING

In general, acoustic scattering from the seafloor is a function of the roughness at the sediment-water interface, roughness of interstitial sediment layers, the distribution of discrete particles or bubbles within the sediment, and fluctuations in the sediment volume density and sound speed. The sediment itself can be modeled as a fluid [32, 34], an elastic [35] or poro-elastic medium [72, 19], or as a system of densely packed sediment grain particles. The variety in model idealizations is due in part to the wide variety of sediment types and seafloor compositions encountered in the ocean environment and the wide range of acoustic frequencies used to interact with the seafloor.

In any particular scenario of sound interaction with the seafloor, one or more of the above mentioned scattering mechanisms or model idealizations may be applicable. Typically, one scattering mechanism is assumed to be dominant. Surface roughness scattering is likely the dominant scattering mechanism for many hard sand and rock sediments. Volume scattering is dominant in sediments composed of soft silts and mud [33]. In the case of competing scattering mechanisms, where two or more types of scattering are present and of comparable effect, single scattering is typically assumed and each scattering mechanism treated independently. This chapter will address the issues of modeling volume scattering from marine sediments.

The appropriate medium idealization to apply at a particular frequency (independent of the scattering mechanism) is still a matter of some debate. In this thesis, it will be assumed that sediment can be modeled as an effective fluid medium. No statement is made about the sediment particle-wave interaction at the frequencies

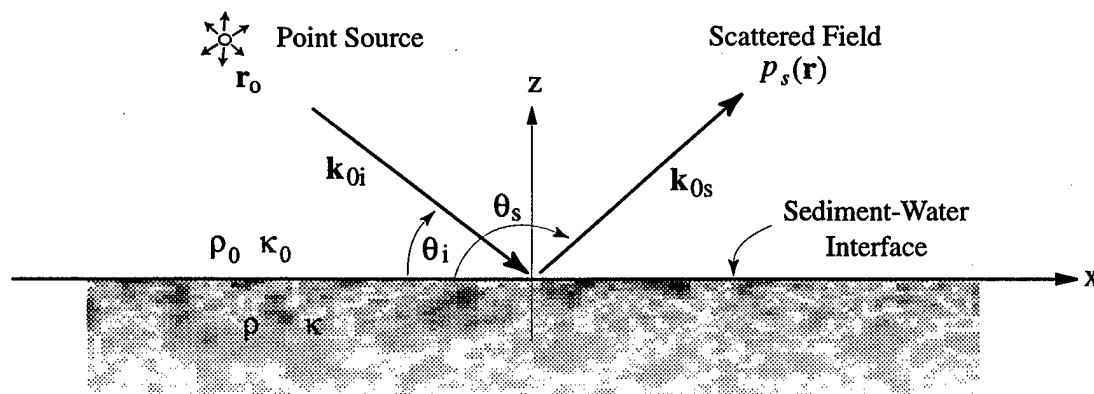


Figure 2.1: Geometry for volume scattering from a half-space random medium.

of interest, only that the net result is an effective continuum whose acoustic properties are modeled as a fluid. Scattering from larger particles such as shells and drop stones will not be considered. It is further assumed that the compressional wave attenuation of the sediment is high and acoustic penetration is limited to the region of sediment near the sediment-water interface. For highly consolidated sediments, shear properties may be significant and the medium would be modeled as an elastic solid. However, in soft sand or mud (near the sediment-water interface) the acoustic shear properties of the medium are weak, and the sediment will be treated as an acoustic fluid [35].

Figure 2.1 illustrates the fluid-fluid half-space interface and geometry for volume scattering. The grazing and scattering angles are defined relative to the plane of the interface. The upper half-space (UHS) contains the positions of the source and receiver and is assumed to be acoustically homogeneous. The lower half-space (LHS) is a continuous random medium of infinite extent in depth and in the horizontal dimension.

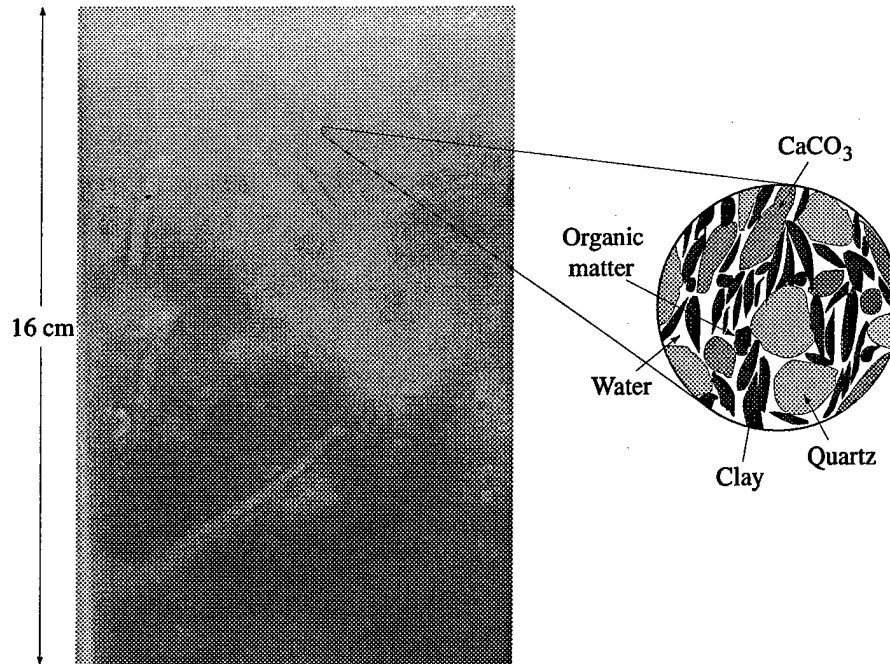


Figure 2.2: Composition of marine sediment near sediment-water interface.

2.1 Sediment Physical Properties

The sediment is assumed to be unconsolidated and composed of a mixture of solid sedimentary particles (or grains) and sea water. Figure 2.2 illustrates a typical sediment composition near the sediment-water interface. Sediment grains may consist of a mixture of silicate sand (quartz), shell fragments (CaCO_3), clay particles, and organic matter, for example. The sediment is assumed to possess no rigid frame (the shear modulus of the medium is zero) and is treated as a fluid half-space continuum. The acoustic phase velocity (c) is defined in terms of the sediment bulk density (ρ) and compressibility (κ):

$$c = \sqrt{\frac{1}{\rho\kappa}}. \quad (2.1)$$

Randomness in the sediment is characterized by fluctuations in the sediment

porosity, which lead to fluctuations in the sediment density and compressibility. Normalized fluctuations in the sediment density and compressibility are defined as

$$\begin{aligned}\gamma_{\kappa} &= (\kappa - \bar{\kappa})/\bar{\kappa}, \\ \gamma_{\rho} &= (\rho - \bar{\rho})/\bar{\rho},\end{aligned}\tag{2.2}$$

where $\bar{\rho}$ and $\bar{\kappa}$ are the mean values. In general, the sediment density is a real quantity, and the compressibility is complex representing dissipation of acoustic energy. They combine to create a complex compressional phase speed in the sediment. The fluctuations in the compressibility are assumed to have the same relative loss as the mean, or

$$\text{Im} \left[\frac{\bar{\kappa}}{\kappa} \right] = 0;\tag{2.3}$$

therefore γ_{κ} is always real. The fluctuation in sediment sound speed is defined as

$$\gamma_c = (c - \bar{c})/\bar{c},\tag{2.4}$$

where

$$\bar{c} = \sqrt{\frac{1}{\bar{\rho}\bar{\kappa}}}.\tag{2.5}$$

The sound speed fluctuations can be written in terms of the density and compressibility fluctuations:

$$\gamma_c = \sqrt{\frac{(1 - \gamma_{\rho})}{(1 + \gamma_{\kappa})}} - 1.\tag{2.6}$$

In the water, ρ_0 and κ_0 are real. The mean values of density or compressibility in both the UHS and LHS are assumed to be constant in space and time (no gradients).

In general, the real and imaginary components of the wavenumber may take any functional form that satisfies causality (i.e., they obey the Kramers-Kronig relationship). For convenience, however, the components are taken to be proportional, such that the wavenumber in the LHS is defined as

$$\bar{k} = \text{Re}[\omega/\bar{c}](1 + i\delta),\tag{2.7}$$

where ω is the acoustic frequency. The compressional loss factor δ is the ratio of the imaginary to real components of the LHS wavenumber. It is assumed to be independent of frequency. This assumption violates causality in the strict sense. However, over the frequency range of interest the resulting dispersion errors are small and can be neglected [47].

If δ is independent of frequency, and dispersion in the medium is negligible, the attenuation will scale as the first power of frequency. Extensive experimental evidence suggests the first power frequency dependence [23, 60], although the frequency dependence of attenuation in unconsolidated marine sediment is still a matter of debate. Intergranular friction and hysteresis, for example, have been proposed as a loss mechanism in which linear scaling with frequency and weak logarithmic dispersion can be explained [16]. Porous medium (Biot) models with added dissipation terms have also been proposed to explain approximately linear frequency relations [72, 19].

The attenuation coefficient in the sediment due to intrinsic absorption, with units of decibels per unit wavelength (dB/ λ), is defined as

$$\alpha_\lambda = \frac{40\pi}{\ln(10)}\delta. \quad (2.8)$$

Another attenuation coefficient that is of practical use has units of decibels per meter per kHz (dB/m/kHz), and is defined as

$$\alpha_f = \frac{1000}{\bar{c}}\alpha_\lambda. \quad (2.9)$$

A constitutive relationship between density and compressibility is not available for marine sediments composed of particles. However, a linear relation is assumed based on measured density-sound speed relationships [13, 45, 88, 32]:

$$\gamma_\kappa = \mu\gamma_\rho, \quad (2.10)$$

where μ is a constant, at least within the confidence intervals of the available data. Fluctuations in sediment sound speed are generally weak compared to fluctuations

in density and compressibility, indicating a negative correlation between density and compressibility. A negative μ also corresponds to a physical picture of sediments where porosity dictates the density and compressibility. As porosity increases, the bulk density of the sediment decreases (assuming the sediment grains are more dense than water). As the volume of water increases relative to the volume of grains, the compressibility increases (assuming that water is more compressible than the grains). As density increases, compressibility decreases. Therefore, μ is generally assumed to be negative.

2.1.1 Correlation and Scale of the Medium Fluctuations

Scattering of sound from the sediment volume depends on the spatial correlation of the density and compressibility fluctuations. The auto- and cross-correlations of the fluctuations are defined as

$$\begin{aligned} C_{\kappa\kappa}(\mathbf{r}_1, \mathbf{r}_2) &= \langle \gamma_{\kappa}(\mathbf{r}_1) \gamma_{\kappa}(\mathbf{r}_2) \rangle , \\ C_{\kappa\rho}(\mathbf{r}_1, \mathbf{r}_2) &= \langle \gamma_{\kappa}(\mathbf{r}_1) \gamma_{\rho}(\mathbf{r}_2) \rangle , \\ C_{\rho\rho}(\mathbf{r}_1, \mathbf{r}_2) &= \langle \gamma_{\rho}(\mathbf{r}_1) \gamma_{\rho}(\mathbf{r}_2) \rangle . \end{aligned} \quad (2.11)$$

For a wide-sense stationary process, the correlation is defined in terms of the difference coordinate $\mathbf{r}_d = \mathbf{r}_1 - \mathbf{r}_2$:

$$C_{\kappa\kappa}(\mathbf{r}_d) = \langle \gamma_{\kappa}(\mathbf{r} + \mathbf{r}_d) \gamma_{\kappa}(\mathbf{r}) \rangle . \quad (2.12)$$

Similarly for the other correlation functions. If it is assumed that the medium compressibility is proportional to the density using (2.10), then

$$C_{\kappa\rho}(\mathbf{r}_d) = C_{\rho\kappa}(\mathbf{r}_d) = \mu C_{\rho\rho}(\mathbf{r}_d) , \quad (2.13)$$

and

$$C_{\kappa\kappa}(\mathbf{r}_d) = \mu^2 C_{\rho\rho}(\mathbf{r}_d) . \quad (2.14)$$

Various functional forms of the correlation function can be assumed depending on the spatial scales of interest. For the acoustic frequencies of interest and the corresponding scales of the randomness in the sediment that interact with the high frequency acoustic waves (correlation scales of approximately 0.01-1.0 meters), the von Karman or the exponential correlation functions are often used [30, 2, 69]. On scales much smaller than the wavelength, the sediment is better described as a dense distribution of grain particles, and a description in terms of a continuous correlation function is not applicable. On the other end of the scale, acoustic interaction with geological features (very large spatial frequencies) can be considered deterministic and handled in the mean sediment properties. For example, large-scale sediment stratigraphy is observed on the scale of meters in deep cores. However, a high-frequency acoustic field will only penetrate a short distance into the sediment due to attenuation, and it will only interact with a single layer.

For an isotropic medium, the von Karman correlation function is defined in terms of the variance of the density fluctuations (σ_ρ^2) and the correlation length scale of the fluctuations (l_c) as

$$C_{\rho\rho}(\mathbf{r}_d) = \frac{\sigma_\rho^2 (r/l_c)^q}{2^q (q-1)!} K_q(r/l_c), \quad (2.15)$$

where $r = |\mathbf{r}_d|$, and K_q is the modified Bessel function of the second kind of order q . The exponential correlation function is a special case of the von Karman correlation function with $q = 2$:

$$C_{\rho\rho}(\mathbf{r}_d) = \sigma_\rho^2 e^{-r/l_c}. \quad (2.16)$$

The exponential correlation function is a commonly assumed form for sediment core analysis [34, 13]. The main reason for applying the exponential assumption is more a function of necessity when processing the sparsely sampled cores rather than a statement of an underlying physical process in the sediment.

The power spectral density (PSD) function of a stationary process is defined as

the Fourier transform of the correlation:

$$S_{\rho\rho}(\mathbf{k}) = \frac{1}{8\pi^3} \int C_{\rho\rho}(\mathbf{r}) e^{-i\mathbf{k}\cdot\mathbf{r}} d\mathbf{r} . \quad (2.17)$$

The corresponding *power law* PSD function for the exponential correlation function is

$$S_{\rho\rho}(\mathbf{k}) = \frac{\sigma_\rho^2 / (\pi^2 l_c)}{(1/l_c^2 + k^2)^2} . \quad (2.18)$$

For a two dimensional process, the power law PSD function is

$$S_{\rho\rho}(\mathbf{k}) = \frac{\sigma_\rho^2 / (2\pi l_c)}{(1/l_c^2 + k^2)^{3/2}} . \quad (2.19)$$

2.2 Volume Scattering Integral Equation

A pressure wave, incident upon the LHS, will interact with heterogeneity in the volume to create a scattered field. In the absence of fluctuations in the medium, the time-harmonic wave equation valid in the UHS is

$$\nabla^2 p(\mathbf{r}) + k_0^2 p(\mathbf{r}) = 0 , \quad (2.20)$$

and valid in the LHS is

$$\bar{\rho}(\mathbf{r}) \nabla \cdot \left[\frac{1}{\bar{\rho}(\mathbf{r})} \nabla p(\mathbf{r}) \right] + \bar{k}^2 p(\mathbf{r}) = 0 . \quad (2.21)$$

The boundary conditions at the interface between the two fluids (at $z = 0$) are the combined Dirichlet and Neumann conditions for a penetrable medium,

$$p(x, y, z = 0^+) = p(x, y, z = 0^-) \quad (2.22)$$

and

$$\frac{1}{\rho_0} \frac{\partial p(x, y, z = 0^+)}{\partial z} = \frac{1}{\bar{\rho}} \frac{\partial p(x, y, z = 0^-)}{\partial z} . \quad (2.23)$$

In the presence of heterogeneity in the LHS, the coefficients of the wave equation are random variables,

$$\rho(\mathbf{r})\nabla \cdot \left[\frac{1}{\rho(\mathbf{r})} \nabla p(\mathbf{r}) \right] + k^2(\mathbf{r})p(\mathbf{r}) = 0, \quad (2.24)$$

where $k^2(\mathbf{r}) = \omega^2 \rho(\mathbf{r}) \kappa(\mathbf{r})$ is the random LHS wavenumber. A single wave equation, valid in the LHS (with or without heterogeneities), can be defined by rearranging (2.24) and grouping the random terms on the right side:

$$\nabla^2 p(\mathbf{r}) + \bar{k}^2 p(\mathbf{r}) = -f(\mathbf{r}). \quad (2.25)$$

The right side represents an induced source term, f , which combines scattering due to fluctuations in the medium's compressibility and density:

$$f(\mathbf{r}) = \bar{k}^2 \gamma_\kappa(\mathbf{r}) p(\mathbf{r}) - \nabla \cdot [\gamma_\rho(\mathbf{r}) \nabla p(\mathbf{r})]. \quad (2.26)$$

The left side of (2.25) is the unperturbed Helmholtz operator. Equation (2.25) is still homogeneous in the unknown quantity p . No new energy is added into the system by the source term. The sources act to redistribute the incident wave through interactions with the heterogeneity in the medium.

The Green's function for the unperturbed system is the solution of the wave equations

$$\nabla^2 g_0(\mathbf{r}) + \bar{k}^2 g_0(\mathbf{r}) = -\delta(\mathbf{r} - \mathbf{r}') \quad (2.27)$$

in the LHS, and

$$\nabla^2 g_0(\mathbf{r}) + k_0^2 g_0(\mathbf{r}) = -\delta(\mathbf{r} - \mathbf{r}') \quad (2.28)$$

in the UHS, that satisfies the appropriate boundary conditions along the sediment-water interface (see Appendix A). With no gradients in the mean density, the spectral representation of the half-space Green's function for transmission from \mathbf{r}' in the LHS to \mathbf{r} across the interface into the UHS is

$$g_0(\mathbf{r}, \mathbf{r}') = \frac{i}{8\pi^2} \int_{-\infty}^{\infty} \frac{1}{\beta} T'(k_x, k_y) e^{i\beta_0 z - i\beta z'} e^{ik_x(x-x') + ik_y(y-y')} dk_x dk_y, \quad (2.29)$$

where

$$\beta = \sqrt{k^2 - k_x^2 - k_y^2} \quad (2.30)$$

and

$$\beta_0 = \sqrt{k_0^2 - k_x^2 - k_y^2} \quad (2.31)$$

are positive to represent a physical field. The coefficient T' is the plane-wave pressure transmission coefficient from the LHS to the UHS:

$$T' = \frac{2\rho_0\beta}{\rho_0\beta + \bar{\rho}\beta_0} \quad (2.32)$$

For \mathbf{r} and \mathbf{r}' both in the LHS, the half-space Green's function including reflection is

$$g_0(\mathbf{r}, \mathbf{r}') = \frac{i}{8\pi^2} \int_{-\infty}^{\infty} \frac{1}{\beta} \left[R(k_x, k_y) e^{i\beta|z+z'|} + e^{i\beta|z-z'|} \right] e^{ik_x(x-x') + ik_y(y-y')} dk_x dk_y, \quad (2.33)$$

where R is the plane-wave pressure reflection coefficient:

$$R = \frac{\rho_0\beta - \bar{\rho}\beta_0}{\rho_0\beta + \bar{\rho}\beta_0} \quad (2.34)$$

The volume scattering integral equation is obtained by applying the Kirchhoff-Helmholtz integral relationship with the source term (2.26):

$$p(\mathbf{r}) = \int_S \left[g_0(\mathbf{r}, \mathbf{r}') \frac{\partial p(\mathbf{r}')}{\partial n'} - p(\mathbf{r}') \frac{\partial g_0(\mathbf{r}, \mathbf{r}')}{\partial n'} \right] ds' + \int_V f(\mathbf{r}') g_0(\mathbf{r}, \mathbf{r}') d\mathbf{r}' \quad (2.35)$$

The first integral in (2.35) is a surface integral over a bounding sphere at infinity, and simply reduces to the incident field. The second integral is the superposition and propagation of the induced sources with the unperturbed Green's function. The volume integral can be simplified by integrating by parts and applying the divergence theorem such that

$$\begin{aligned} \int_V \nabla' \cdot [\gamma_\rho(\mathbf{r}') \nabla' p(\mathbf{r}')] g_0(\mathbf{r}, \mathbf{r}') d\mathbf{r}' &= \int_S \gamma_\rho(\mathbf{r}') \frac{\partial p(\mathbf{r}')}{\partial n'} g_0(\mathbf{r}, \mathbf{r}') ds' \\ &- \int_V \gamma_\rho(\mathbf{r}') \nabla' g_0(\mathbf{r}, \mathbf{r}') \cdot \nabla' p(\mathbf{r}') d\mathbf{r}' \end{aligned} \quad (2.36)$$

By applying the radiation condition at infinity, the surface integral in (2.36) vanishes. The final integral equation for the total field can be written as the sum of the unperturbed field (p_0) and the scattered field (p_s):

$$p(\mathbf{r}) = p_0(\mathbf{r}) + p_s(\mathbf{r}) . \quad (2.37)$$

The scattered field is the sum of all the fields due to the differential sources within the volume:

$$p_s(\mathbf{r}) = \int_V [\bar{k}^2 \gamma_\kappa(\mathbf{r}') g_0(\mathbf{r}, \mathbf{r}') p(\mathbf{r}') + \gamma_\rho(\mathbf{r}') \nabla' g_0(\mathbf{r}, \mathbf{r}') \cdot \nabla' p(\mathbf{r}')] d\mathbf{r}' . \quad (2.38)$$

Equation (2.38) is similar to the well-known integral equation [54] which uses the free-space Green's function. However, now the half-space boundary conditions are included by the use of the half-space Green's functions. The first term in the volume integral represents monopole scattering due to compressibility fluctuations at a point in the volume. The second term represents dipole scattering due to the dot product of gradients in the field and Green's function at a point in the volume. The integration is over the volume of the LHS medium. With significant attenuation in the lower medium, the scattered field will penetrate only a limited distance into the medium so that the acoustic energy from the incident field will be confined to a layer near the surface of the LHS. Therefore, the depth dimension of the volume is finite and for many practical problems will be relatively small.

If the medium is fluctuating in time, the scattered field will fluctuate in time, as well as in space. If the medium is fluctuating slowly compared to the frequency of the acoustic wave, the time dependence of the medium carries through into the scattering integral equation:

$$p_s(\mathbf{r}, t) = \int_V [\bar{k}^2 \gamma_\kappa(\mathbf{r}', t) g_0(\mathbf{r}, \mathbf{r}') p(\mathbf{r}', t) + \gamma_\rho(\mathbf{r}', t) \nabla' g_0(\mathbf{r}, \mathbf{r}') \cdot \nabla' p(\mathbf{r}', t)] d\mathbf{r}' . \quad (2.39)$$

Here, the time dependence is a function of the medium only. The pressure field is still assumed to be time-harmonic, and this time dependence is suppressed.

If the medium density and compressibility are known, the scattered field inside and outside the scattering medium can be found uniquely using the appropriate Green's function. However, analytic solutions to (2.38) and (2.39) for a random medium are generally not available.

2.3 Small Perturbation Method

If the fluctuations in the medium are small, the solution for the perturbed system will be similar to the solution of the unperturbed system. Therefore, assume that the unknown scattered field can be expanded as a *perturbation series* in powers of some small and dimensionless quantity ϵ , such that

$$p(\mathbf{r}) = \phi_0 + \epsilon\phi_1(\mathbf{r}) + \epsilon^2\phi_2(\mathbf{r}) + \dots, \quad (2.40)$$

where ϵ is of the order of magnitude of the medium fluctuations:

$$O(\epsilon) = O(\gamma_\kappa) = O(\gamma_\rho). \quad (2.41)$$

The perturbation series is defined as an asymptotic series with respect to the sequence $1, \epsilon, \epsilon^2, \dots$ and the basis functions ϕ_n having the property

$$p - \sum_{n=0}^N \epsilon^n \phi_n = O(\epsilon^N) \text{ as } \epsilon \rightarrow 0. \quad (2.42)$$

This property does not guarantee that the series will converge. Therefore, increasing the number of terms in (2.40) does not necessarily improve the solution. Even if the series does seem to converge, it may not necessarily converge towards the correct result. The reason for this is that the asymptotic expansion only makes a statement about the series in the limit as $\epsilon \rightarrow 0$, not as $N \rightarrow \infty$. Therefore, as the small parameter ϵ increases (as the medium fluctuations grow larger), the perturbation solution is unpredictable. However, if the parameter ϵ is "small", the higher-order terms in the series will often decay rapidly [42]. Therefore, a relatively small number

of terms can be used to accurately represent the behavior of the solution. Each higher-order term in the series then corresponds to a higher-order correction to the true field.

The consecutive terms of the perturbation series are obtained by substituting (2.40) into the integral equation (2.37) and balancing terms by powers of ϵ :

$$\begin{aligned} p &= \phi_0 + \epsilon\phi_1 + \epsilon^2\phi_2 + \cdots \\ &= p_0 + L[\phi_0] + L[\epsilon\phi_1] + L[\epsilon^2\phi_2] + \cdots \end{aligned} \quad (2.43)$$

The operator L is the linear integral operator of (2.38) or (2.39). Since only single powers of γ_κ or γ_ρ are present in the operator, L is first-order in ϵ . The zeroth-order term (corresponding to no randomness in the medium) is found to be

$$\phi_0 = p_0 . \quad (2.44)$$

This is the known solution to the unperturbed problem, and for a unit point source is simply the Green's function (2.29) or (2.33). The first-order term in the perturbation series is found, by substituting in the zeroth-order solution, to be

$$\epsilon\phi_1 = L[\phi_0] = L[p_0] . \quad (2.45)$$

The second-order term is similarly found to be

$$\epsilon^2\phi_2 = L[\epsilon\phi_1] = L^2[p_0] . \quad (2.46)$$

Continuing in this manner, the perturbation series for the total field is

$$p = p_0 + L[p_0] + L^2[p_0] + L^3[p_0] + \cdots . \quad (2.47)$$

Redefining the scattered field as a series of higher-order correction terms,

$$p_s = p^{(1)} + p^{(2)} + p^{(3)} + \cdots , \quad (2.48)$$

where $p^{(1)}$ is of order ϵ , $p^{(2)}$ is of order ϵ^2 , and so on, it follows that each higher-order correction can be found uniquely in terms of the preceding order correction:

$$p^{(n+1)} = L[p^{(n)}]. \quad (2.49)$$

Using equation (2.39), the perturbation terms for the volume scattering integral representation are found to be

$$p^{(n+1)}(\mathbf{r}, t) = \int_V [\bar{k}^2 \gamma_\kappa(\mathbf{r}', t) g_0(\mathbf{r}, \mathbf{r}') p^{(n)}(\mathbf{r}', t) + \gamma_\rho(\mathbf{r}', t) \nabla' g_0(\mathbf{r}, \mathbf{r}') \cdot \nabla' p^{(n)}(\mathbf{r}', t)] d\mathbf{r}' \quad (2.50)$$

for $n = 0, 1, 2, \dots$. If the fluctuations are within the range of validity of the perturbation solution, a low-order approximation will sufficiently represent the scattered field.

The equivalent perturbation result can also be found by direct iteration of the integral equation [67]. It can also be found by substituting the perturbation series directly into the wave equation for the LHS and satisfying boundary conditions along the interface [42]. The methods are equivalent and need not be repeated.

2.3.1 First-Order Perturbation Method

For a source and receiver positioned in the UHS and in the far-field of the interface (see Figure 2.1), the *first-order* scattered field can be found in terms of a convenient Fourier integral over the scattering volume. Using the method of stationary phase to evaluate the Green's function (2.29) in the far field (see Appendix B), the half-space Green's function for transmission from the lower to the upper medium is approximated as

$$g_0(\mathbf{r}, \mathbf{r}') = \frac{\rho_0 T(\theta_s)}{\rho} \frac{e^{ik_0 r}}{4\pi r} e^{-i\mathbf{k}_s \cdot \mathbf{r}'} \quad (2.51)$$

Similarly, the incident field at \mathbf{r}' in the LHS due to a source at \mathbf{r}_0 is

$$p_0(\mathbf{r}') = g_0(\mathbf{r}', \mathbf{r}_0) = \frac{T(\theta_i)}{4\pi r_0} e^{ik_0 r_0} e^{i\mathbf{k}_i \cdot \mathbf{r}'} \quad (2.52)$$

The position vectors \mathbf{r} and \mathbf{r}_0 lie in the water, and \mathbf{r}' lies in the sediment. The wave vectors \mathbf{k}_i and \mathbf{k}_s are oriented in the incident and scattering directions in the LHS, respectively. They are defined as

$$\begin{aligned}\mathbf{k}_i &= k_{xi}\hat{x} + k_{yi}\hat{y} - \beta_i\hat{z}, \\ \mathbf{k}_s &= k_{xs}\hat{x} + k_{ys}\hat{y} + \beta_s\hat{z},\end{aligned}\tag{2.53}$$

with β_i and β_s defined analogously to (2.30). The horizontal components of the incident and scattered field wavevectors are defined as $k_{xi} = k_0x_0/r_0$, $k_{xs} = k_0x/r$, $k_{yi} = k_0y_0/r_0$, and $k_{ys} = k_0y/r$. The coefficient T is the pressure transmission coefficient for a plane wave incident upon the interface from the water at the incident and scattering angles, θ_i and θ_s respectively:

$$\begin{aligned}T(\theta_i) &= \frac{2\bar{\rho}\beta_0}{\rho_0\beta_i + \bar{\rho}\beta_0}, \\ T(\theta_s) &= \frac{2\bar{\rho}\beta_0}{\rho_0\beta_s + \bar{\rho}\beta_0}.\end{aligned}\tag{2.54}$$

Using (2.50), (2.51) and (2.52), the *first-order* bistatic field at position \mathbf{r} is found to be

$$p^{(1)}(\mathbf{r}, t) = \Gamma(\mathbf{r}) \int_V d\mathbf{r}' [\bar{k}^2 \gamma_\kappa(\mathbf{r}', t) + \gamma_\rho(\mathbf{r}', t)(\mathbf{k}_i \cdot \mathbf{k}_s)] e^{i(\mathbf{k}_i - \mathbf{k}_s) \cdot \mathbf{r}'}, \tag{2.55}$$

where

$$\Gamma(\mathbf{r}) = \frac{\rho_0}{\rho} \frac{T(\theta_i)T(\theta_s)}{(4\pi)^2 r_0 r} e^{ik_0(r_0+r)}.\tag{2.56}$$

Figure 2.3a illustrates the first-order result graphically. The incident field is refracted into the lower medium and interacts with the inhomogeneities. The scattered field is an integral over all the monopole (γ_κ) and dipole (γ_ρ) sources in the volume shifted in phase by the factor related to the incident and scattered directions. The integral results in a Fourier transform of the medium fluctuations over the volume of the medium. Since the volume of the scattering medium is the half-space, the Fourier integral must be windowed in the depth direction.

The equivalent result for a two-dimensional medium is found using the two-dimensional far-field Green's functions

$$g_0(\mathbf{r}, \mathbf{r}') = -i \frac{\rho_0}{\rho} \frac{T(\theta_s)}{\sqrt{8\pi k_0 r}} e^{ik_0 r} e^{-i\mathbf{k}_s \cdot \mathbf{r}'} e^{-i\pi/4} \quad (2.57)$$

and incident field

$$p_0(\mathbf{r}') = -i \frac{T(\theta_i)}{\sqrt{8\pi k_0 r_0}} e^{ik_0 r_0} e^{i\mathbf{k}_i \cdot \mathbf{r}'} e^{-i\pi/4}, \quad (2.58)$$

where $\mathbf{r} = (x, z)$ (see Appendix A). The two-dimensional integral equation for the scattered field is the same as (2.55) except the geometric factor is redefined as

$$\Gamma(\mathbf{r}) = \frac{\rho_0}{\rho} \frac{T(\theta_i)T(\theta_s)}{8\pi k_0 \sqrt{r_0 r}} e^{ik_0(r_0+r)}, \quad (2.59)$$

and the integration is over the two-dimensional medium.

2.3.2 Higher-Order Perturbation Fields

The scattered fields represented by higher-order terms in the perturbation series can be interpreted physically by examining the recursive nature of (2.50). The second-order perturbation result, which contains a double integral operation, is found by substituting the first-order result into (2.50):

$$\begin{aligned} p^{(2)}(\mathbf{r}) = & \bar{k}^4 \iint \gamma_\kappa(\mathbf{r}_2) \gamma_\kappa(\mathbf{r}_1) g_0(\mathbf{r}, \mathbf{r}_2) g_0(\mathbf{r}_2, \mathbf{r}_1) g_0(\mathbf{r}_1, \mathbf{r}_0) d\mathbf{r}_1 d\mathbf{r}_2 \\ & + \bar{k}^2 \iint \gamma_\kappa(\mathbf{r}_2) \gamma_\rho(\mathbf{r}_1) g_0(\mathbf{r}, \mathbf{r}_2) \nabla_1 g_0(\mathbf{r}_2, \mathbf{r}_1) \cdot \nabla_1 g_0(\mathbf{r}_1, \mathbf{r}_0) d\mathbf{r}_1 d\mathbf{r}_2 \\ & + \bar{k}^2 \iint \gamma_\rho(\mathbf{r}_2) \gamma_\kappa(\mathbf{r}_1) \nabla_2 g_0(\mathbf{r}, \mathbf{r}_2) \cdot \nabla_2 g_0(\mathbf{r}_2, \mathbf{r}_1) g_0(\mathbf{r}_1, \mathbf{r}_0) d\mathbf{r}_1 d\mathbf{r}_2 \\ & + \iint \gamma_\rho(\mathbf{r}_2) \gamma_\rho(\mathbf{r}_1) \nabla_2 g_0(\mathbf{r}, \mathbf{r}_2) \cdot [\nabla_2 \nabla_1 g_0(\mathbf{r}_2, \mathbf{r}_1)] \cdot \nabla_1 g_0(\mathbf{r}_1, \mathbf{r}_0) d\mathbf{r}_1 d\mathbf{r}_2. \end{aligned} \quad (2.60)$$

The operator ∇_1 is the gradient with respect to \mathbf{r}_1 ; ∇_2 is the gradient with respect to \mathbf{r}_2 ; and $\nabla_2 \nabla_1$ is a dyad operator. The time variable t is suppressed for convenience.

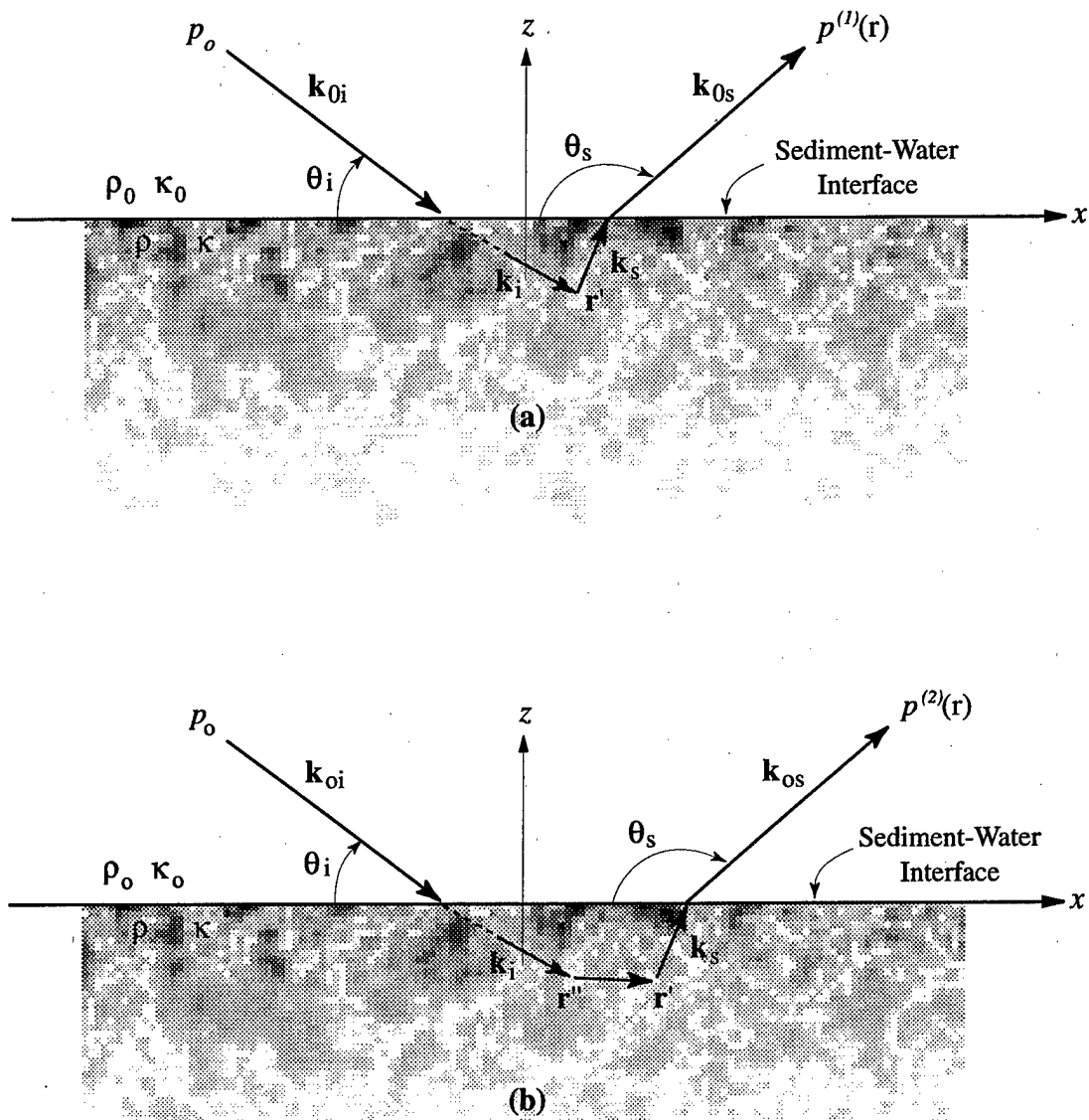


Figure 2.3: Small perturbation method for volume scattering from a random half-space: (a) first-order scattering; (b) second-order scattering.

Consider the double integrals in the second-order expression. The presence of the Green's function $g_0(\mathbf{r}_2, \mathbf{r}_1)$ represents the interaction between the elemental volumes $d\mathbf{r}_1$ and $d\mathbf{r}_2$. Therefore, the second-order term in the perturbation series represents the field due to second-order scattering in the medium, that is, scattering due to the interaction of two elemental volumes. The first integral is double scattering due to compressibility fluctuations. The second and third integrals are double scattering between compressibility and density fluctuations. The fourth integral is double scattering due to density fluctuations. The dot products of the gradients of the Green's functions can be thought of as creating a dipole directivity of the scattered field. In the far-field, the gradient in the Green's function creates dipole patterns oriented in the direction of propagation. Figure 2.3b illustrates the second-order interactions due to scattering by density and compressibility fluctuations. The third-order perturbation term includes third-order scattering. Similarly, higher-order terms of the perturbation series represent higher-order scattering in the medium. The scattered field (for each higher order) will be composed of all the possible compressibility and density interactions.

Scattering diagrams (due to Feynman) are a useful method of expressing the higher-order terms [68, 80]. Let $g_0(\mathbf{r}_1, \mathbf{r}_0)$ be represented by a straight line segment:

$$g_0(\mathbf{r}_2, \mathbf{r}_1) \sim \frac{\quad}{\mathbf{r}_2 \quad \mathbf{r}_1} . \quad (2.61)$$

The vertices of the line segment represent the integration variables. Several new symbols are defined to represent the medium and derivatives of the Green's function. A filled vertex represents a compressibility fluctuation, and a hollow vertex represents a density fluctuation:

$$\begin{aligned} \bar{k}^2 \gamma_\kappa(\mathbf{r}) &\sim \bullet , \\ \gamma_\rho(\mathbf{r}) &\sim \circ . \end{aligned} \quad (2.62)$$

An arrow on the line segment represents the gradient of the Green's function with

respect to the integration variable the arrow is pointing towards:

$$\begin{aligned} \nabla_1 g_0(\mathbf{r}_2, \mathbf{r}_1) &\sim \overrightarrow{\text{---}}_{\mathbf{r}_2 \quad \mathbf{r}_1}, \\ \nabla_2 g_0(\mathbf{r}_2, \mathbf{r}_1) &\sim \overleftarrow{\text{---}}_{\mathbf{r}_2 \quad \mathbf{r}_1}. \end{aligned} \tag{2.63}$$

The second-order perturbation term can now be expressed in diagrams as

$$\begin{aligned} p^{(2)}(\mathbf{r}) = & \overline{\text{---}}_{\mathbf{r} \quad \mathbf{r}_2 \quad \mathbf{r}_1 \quad \mathbf{r}_0} + \overrightarrow{\text{---}}_{\mathbf{r} \quad \mathbf{r}_2} \text{---} \overleftarrow{\text{---}}_{\mathbf{r}_1 \quad \mathbf{r}_0} + \\ & \overrightarrow{\text{---}}_{\mathbf{r} \quad \mathbf{r}_2} \overleftarrow{\text{---}}_{\mathbf{r}_1 \quad \mathbf{r}_0} + \overrightarrow{\text{---}}_{\mathbf{r} \quad \mathbf{r}_2} \overleftarrow{\text{---}}_{\mathbf{r}_1 \quad \mathbf{r}_0} \overleftarrow{\text{---}}_{\mathbf{r}_1 \quad \mathbf{r}_0}. \end{aligned} \tag{2.64}$$

The diagrams can be simplified by dropping the coordinates of the inner vertices. Noting also that the hollow vertices are always bracketed by arrows representing the gradient operation, the arrows will be dropped and the derivatives implied. The third-order perturbation result is represented as follows:

$$\begin{aligned} p^{(3)}(\mathbf{r}) = & \overline{\text{---}}_{\mathbf{r} \quad \bullet \quad \bullet \quad \bullet \quad \mathbf{r}_0} + \overline{\text{---}}_{\mathbf{r} \quad \bullet \quad \bullet \quad \circ \quad \mathbf{r}_0} + \\ & \overline{\text{---}}_{\mathbf{r} \quad \bullet \quad \circ \quad \bullet \quad \mathbf{r}_0} + \overline{\text{---}}_{\mathbf{r} \quad \circ \quad \bullet \quad \bullet \quad \mathbf{r}_0} + \\ & \overline{\text{---}}_{\mathbf{r} \quad \bullet \quad \circ \quad \circ \quad \mathbf{r}_0} + \overline{\text{---}}_{\mathbf{r} \quad \circ \quad \bullet \quad \circ \quad \mathbf{r}_0} + \\ & \overline{\text{---}}_{\mathbf{r} \quad \circ \quad \circ \quad \bullet \quad \mathbf{r}_0} + \overline{\text{---}}_{\mathbf{r} \quad \circ \quad \circ \quad \circ \quad \mathbf{r}_0}. \end{aligned} \tag{2.65}$$

2.4 Temporal and Spatial Correlation of the Scattered Field

As the sediment fluctuates randomly in space and time, the scattered field will fluctuate. Thus, the scattered field is a random process, which can be characterized by the cross-correlation of p_s at two different locations and times:

$$C_{pp} = \langle p_s(\mathbf{r}_1, t_1) p_s^*(\mathbf{r}_2, t_2) \rangle. \tag{2.66}$$

Using the perturbation result (2.55) and considering only the case where $\mathbf{r}_1 = \mathbf{r}_2$, the correlation of the first-order bistatic scattered field can be found. Assuming the randomness in the medium is stationary in space and time and making the

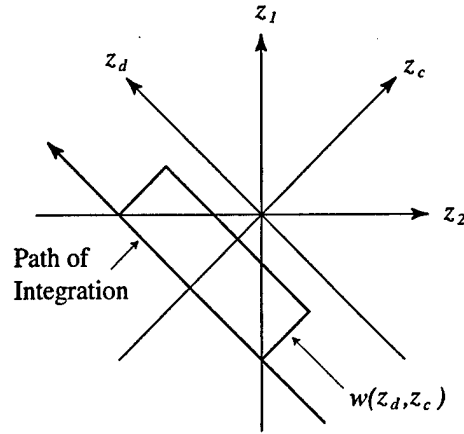


Figure 2.4: Half-space windowing in the difference coordinates.

change of integration variables to the difference and center coordinates, defined as $\mathbf{r}'_d = \mathbf{r}'_1 - \mathbf{r}'_2$, and $\mathbf{r}'_c = (\mathbf{r}'_1 + \mathbf{r}'_2)/2$, respectively, and the difference in time $\tau = t_1 - t_2$, the correlation function is found to be

$$C_{pp}(\tau) = A |\Gamma(\mathbf{r})|^2 \int_{-\infty}^0 dz'_c \int_{hs} d\mathbf{r}'_d C(\mathbf{r}'_d, \tau) e^{-i\mathbf{k}_d \cdot \mathbf{r}'_d} e^{-2\alpha z'_c}. \quad (2.67)$$

The difference between the incident and scattered wave vectors is the Bragg wave vector, $\mathbf{k}_d = \text{Re}[\mathbf{k}_i - \mathbf{k}_s]$. The area of the scattering region is A , and α is the imaginary part of the vertical component of the difference between the incident and scattered wave vectors:

$$\alpha \equiv \text{Im}[(\mathbf{k}_i - \mathbf{k}_s) \cdot \hat{z}] = -\text{Im}[\beta_i + \beta_s]. \quad (2.68)$$

The integral on the difference coordinate is over the windowed half-space volume (see Figure 2.4) defined as

$$\int_{hs} d\mathbf{r}'_d = \int_{-\infty}^{\infty} dx'_d \int_{-\infty}^{\infty} dy'_d \int_{2z_c}^{-2z_c} dz'_d. \quad (2.69)$$

The combined sediment correlation function is

$$C(\mathbf{r}_d, \tau) = |\bar{k}|^4 C_{\kappa\kappa}(\mathbf{r}_d, \tau) + 2\text{Re}[\bar{k}^2 (\mathbf{k}_i \cdot \mathbf{k}_s)] C_{\kappa\rho}(\mathbf{r}_d, \tau) + |\mathbf{k}_i \cdot \mathbf{k}_s|^2 C_{\rho\rho}(\mathbf{r}_d, \tau). \quad (2.70)$$

The functions $C_{\kappa\kappa}$, $C_{\kappa\rho}$, and $C_{\rho\rho}$ are the auto- and cross-correlations of the zero-mean functions defined in Section 2.1.1.

If it is assumed that the medium compressibility is proportional to the density using (2.14), then the correlation function is simplified to

$$C(\mathbf{r}_d, \tau) = |\mu \bar{k}^2 + (\mathbf{k}_i \cdot \mathbf{k}_s)|^2 C_{\rho\rho}(\mathbf{r}_d, \tau). \quad (2.71)$$

The effect of the half-space geometry on the correlation function (2.67) is to create a sliding windowing in the z_d direction, as defined in Figure 2.4. The half-space windowing function is a depth-dependent rectangular window,

$$w(z_d, z_c) = \begin{cases} 1 & \text{if } |z_d| \leq 2z_c, \\ 0 & \text{otherwise,} \end{cases} \quad (2.72)$$

having the Fourier transform

$$W(k_z, z_c) = \frac{\sin(2k_z z_c)}{\pi k_z}. \quad (2.73)$$

Applying the Wiener-Khintchin theorem and the Fourier windowing theorem, the correlation function (2.67) can be expressed in terms of the time-domain spatial-spectrum of density fluctuations:

$$C_{\rho\rho}(\tau) = 8\pi^3 A |\Gamma(\mathbf{r})|^2 |\mu \bar{k}^2 + (\mathbf{k}_i \cdot \mathbf{k}_s)|^2 \tilde{S}_{\rho\rho}(\mathbf{k}_d, \tau). \quad (2.74)$$

The density spectrum, $\tilde{S}_{\rho\rho}$, is not the true spectrum but rather the convolution of the true density spectrum and the Fourier transform of the half-space window, defined as

$$\tilde{S}_{\rho\rho}(\mathbf{k}_d, \tau) = \int_{-\infty}^0 dz_c \int_{-\infty}^{\infty} dk'_{dz} S_{\rho\rho}(k_{dx}, k_{dy}, k'_{dz}, \tau) W(k'_{dz} - k_{dz}, z_c) e^{-2\alpha z_c}. \quad (2.75)$$

The convolution integration of (2.75) is only over the z -component of the Bragg wavenumber. Using (2.73), the integration over z_c in (2.75) can be performed to find the modified spectrum:

$$\tilde{S}_{\rho\rho}(\mathbf{k}_d, \tau) = \frac{2}{\pi} \int_{-\infty}^{\infty} \frac{S_{\rho\rho}(k_{dx}, k_{dy}, k'_{dz}, \tau)}{2\pi[\alpha^2 + (k'_{dz} - k_{dz})^2]} dk'_{dz}. \quad (2.76)$$

The modified spectrum can also be shown to be the Fourier transform of the true density correlation function windowed in depth by the medium attenuation:

$$\tilde{S}_{\rho\rho}(\mathbf{k}_d, \tau) = \frac{1}{8\pi^3} \int_{-\infty}^{\infty} \left[C_{\rho\rho}(\mathbf{r}_d, \tau) \frac{e^{-\alpha|z_d|}}{2\alpha} \right] e^{-i\mathbf{k}_d \cdot \mathbf{r}_d} d\mathbf{r}_d . \quad (2.77)$$

Therefore, the half-space effectively modifies the correlation structure of the medium in the depth direction. If attenuation in the medium is low, the half-space effects will be minimized. The incident field will penetrate a significant depth into the medium, relative to the correlation length of the fluctuations, and scattering from the half-space medium can be modeled using the true spectrum. If the attenuation is high, the field will be limited to a layer near the interface. If the penetration depth is smaller or comparable in dimension to the correlation scale of the medium, the half-space effects will be significant.

2.5 Scattering Cross-Section

The scattering cross-section is defined in terms of the incoherent intensity of the scattered far-field. If the penetration distance into the sediment is small compared to the distance traveled in water, it is typical to describe volume scattering in terms of an equivalent surface scattering strength. For a pressure wave incident on the surface of area A , the bistatic surface scattering cross-section (per unit area per unit solid angle) is defined as

$$\sigma_s = \frac{I_s(r)r^2}{I_i A} , \quad (2.78)$$

where r is the distance to the receiver in the far-field (Figure 2.1), and

$$I_i = \frac{k_0}{2\rho_0\omega} |p_0|^2 \quad (2.79)$$

is the incident intensity immediately above the interface. For convenience, σ_s will simply be referred to as the cross-section. The scattering strength is defined as $10 \log_{10}(\sigma_s)$ in units of dB.

The incoherent scattered intensity is defined in terms of the zero-lag covariance of the scattered field as

$$I_s(r) = \frac{k_0}{2\rho_0\omega} [\langle p_s(r)p_s^*(r) \rangle - |\langle p_s(r) \rangle|^2] . \quad (2.80)$$

The scattered field covariance can be found using the perturbation expansion for the scattered field (2.48). By consistently grouping terms in the resulting covariance expansion by powers of the small parameter, the scattering cross-section is found as the perturbation series

$$\sigma_s = \sigma_s^{(1)} + \sigma_s^{(2)} + \sigma_s^{(3)} + \sigma_s^{(4)} + \dots . \quad (2.81)$$

Each higher-order term in the cross-section series corresponds to the complete grouping of like orders from the scattered field covariance. The first-order cross-section is zero. The second-order cross-section is found to be

$$\sigma_s^{(2)} = \frac{r^2}{A|p_0|^2} [\langle |p^{(1)}|^2 \rangle - \eta_s^{(2)}] , \quad (2.82)$$

which is second-order in the scattered field, and

$$\eta_s^{(2)} = |\langle p^{(1)} \rangle|^2 . \quad (2.83)$$

The third-order cross-section is

$$\sigma_s^{(3)} = \frac{r^2}{A|p_0|^2} [\langle p^{(1)}p^{*(2)} + p^{(2)}p^{*(1)} \rangle - \eta_s^{(3)}] , \quad (2.84)$$

where

$$\eta_s^{(3)} = \langle p^{(1)} \rangle \langle p^{*(2)} \rangle + \langle p^{(2)} \rangle \langle p^{*(1)} \rangle . \quad (2.85)$$

The fourth-order cross-section is

$$\sigma_s^{(4)} = \frac{r^2}{A|p_0|^2} [\langle |p^{(2)}|^2 + p^{(1)}p^{*(3)} + p^{(3)}p^{*(1)} \rangle - \eta_s^{(4)}] , \quad (2.86)$$

where

$$\eta_s^{(4)} = |\langle p^{(2)} \rangle|^2 + \langle p^{(1)} \rangle \langle p^{*(3)} \rangle + \langle p^{(3)} \rangle \langle p^{*(1)} \rangle . \quad (2.87)$$

Note that $\langle p^{(1)} \rangle = 0$, and for a Gaussian process all odd-order cross-sections are also zero.

Using (2.55) for the first-order scattered field, and using (2.52) to find the incident intensity, the second-order surface scattering cross-section as a function of the incident and scattering angles is found to be

$$\sigma_s^{(2)}(\theta_i, \theta_s) = \frac{\pi}{2} \frac{\rho_0^2}{\rho^2} |T(\theta_i)|^2 |T(\theta_s)|^2 |\mu \bar{k}^2 + (\mathbf{k}_i \cdot \mathbf{k}_s)|^2 \tilde{S}_{\rho\rho}(\mathbf{k}_d) . \quad (2.88)$$

Defining a depth-dependent volume cross-section as

$$\sigma_s = \int_{-\infty}^0 \sigma_v(z_c) dz_c , \quad (2.89)$$

and using (2.75), the second-order volume cross-section is found as

$$\sigma_v^{(2)}(z_c) = \frac{\pi}{2} |\mu \bar{k}^2 + (\mathbf{k}_i \cdot \mathbf{k}_s)|^2 \int_{-\infty}^{\infty} S_{\rho\rho}(\mathbf{k}'_d) W(k'_z - k_z, z_c) dk'_z . \quad (2.90)$$

This expression for cross-section is similar to those derived by [32, 34, 26], except half-space effects are included.

The total scattering cross-section of the volume is defined as

$$\sigma_{tv} = \int_{4\pi} \sigma_v d\omega , \quad (2.91)$$

where $d\omega$ is the differential solid angle. The total surface scattering cross-section is defined as

$$\sigma_{ts} = \int_{2\pi} \sigma_s d\omega , \quad (2.92)$$

where $d\omega$ is the differential solid angle over the UHS hemisphere.

In two dimensions, the second-order, bistatic, surface-scattering cross-section is defined as

$$\sigma_s(\theta_i, \theta_s) = \frac{I_s(r)r}{I_i L} , \quad (2.93)$$

where L is the length of the horizontal scattering region. The two-dimensional first-order scattering cross-section, using (2.57) and (2.58), is found to be

$$\sigma_s^{(2)}(\theta_i, \theta_s) = \frac{\pi \rho_0^2}{2 \rho^2} \frac{1}{k_0} |T(\theta_i)|^2 |T(\theta_s)|^2 |\mu \bar{k}^2 + (\mathbf{k}_i \cdot \mathbf{k}_s)|^2 \tilde{S}_{\rho\rho}(\mathbf{k}_d, \tau), \quad (2.94)$$

where $\tilde{S}_{\rho\rho}$ is now the two-dimensional half-space spectrum.

2.6 Scattering of a Narrow Band Pulse

In many practical applications of scattering from a random medium, it is necessary to use a finite duration pulse as the incident field and consider the time-domain scattered field. The scattered field is typically time-gated to correspond to scattering from an isolated and finite region of the scattering medium. This is especially true for scattering from the seafloor where multipath propagation can create complicated interactions of different scattering mechanisms. It is necessary, therefore, to relate the time-independent scattering of a continuous wave field to the time-dependent scattering of a pulsed field. In this section, the classical narrow-band approximation for a time-varying medium [30] is applied to the half-space volume scattering problem.

Consider the scattered field $p_s(t)$ at a point in space due to a pulsed input field $p_i(t)$, suppressing the spatial dependence of the field for a moment. The fields are defined as the real component of the complex envelope functions modulating the carrier at frequency ω_0 :

$$\begin{aligned} p_s(t) &= \text{Re} [u_s(t)e^{-i\omega_0 t}] , \\ p_i(t) &= \text{Re} [u_i(t)e^{-i\omega_0 t}] . \end{aligned} \quad (2.95)$$

The envelope functions can be expressed in terms of a time-varying amplitude and phase:

$$\begin{aligned} u_s(t) &= A_s(t)e^{i\phi_s(t)} , \\ u_i(t) &= A_i(t)e^{i\phi_i(t)} . \end{aligned} \quad (2.96)$$

For a narrow band input signal, $A_i(t)$ and $\phi_i(t)$ are slowly varying functions of time relative to the carrier frequency.

Since the scattering medium is linear, the scattered output field can be related to the input field by the integral

$$p_s(t) = \int_{-\infty}^t p_i(t')h(t, t')dt' , \quad (2.97)$$

where $h(t, t')$ is the response of the medium at time t due to an impulse input at t' . Equivalently, the output envelope function can be expressed in terms of the Fourier transform of the input envelope function and the system frequency response:

$$u_s(t) = 2\pi \int_{-\infty}^{\infty} U_i(\omega)H(\omega_0 + \omega, t)e^{-i\omega t}d\omega \quad (2.98)$$

where

$$U_i(\omega) = \frac{1}{2\pi} \int_{-\infty}^{\infty} u_i(t')e^{i\omega t'} dt' , \quad (2.99)$$

and

$$H(\omega, t) = \frac{1}{2\pi} \int_0^{\infty} h(t, t-t')e^{i\omega t'} dt' . \quad (2.100)$$

The function $H(\omega, t)$ is the time-varying transfer function of the medium (see [30] Chapter 6). By definition, it is the scattered output field when the input field is a time-harmonic function. Therefore, $H(\omega, t)$ is simply the CW solution (found using perturbation or exact methods, for example). Using the first-order perturbation result from Section 2.3.1, the response of the volume scattering medium is

$$H(\omega, t) = \Gamma(\mathbf{r}) \int_V [\bar{k}^2 \gamma_{\kappa}(\mathbf{r}', t) + \gamma_{\rho}(\mathbf{r}', t)(\mathbf{k}_i \cdot \mathbf{k}_s)] e^{i(\mathbf{k}_i - \mathbf{k}_s) \cdot \mathbf{r}'} d\mathbf{r}' . \quad (2.101)$$

If the medium is time-invariant, $H(\omega, t)$ is time-invariant. For the cases of interest in this thesis, the medium is varying in time much slower than the acoustic frequency, and $H(\omega, t)$ can be considered a constant in time over the duration of the pulse scattering.

As the input pulse propagates through the scattering medium and interacts with spatial inhomogeneities, the scattered output field becomes a random function of time. Temporal statistics of the output field reflect the temporal and spatial statistics of the medium and the characteristics of the input pulse. The pulse characteristics include the receiver and transmitter beam patterns, the pulse duration and bandwidth. For backscattering at any instant in time, the region enveloped by half (round trip) the spatial extent of the pulse becomes the effective scattering volume that contributes to the scattered field at that instant in time. This region is called the "ensonified volume."

A fundamental statistical descriptor that shows the influence of the ensonified volume is the correlation of the complex envelope of the scattered field:

$$C_{uu}(t_1, t_2) = \langle u_s(t_1)u_s^*(t_2) \rangle . \quad (2.102)$$

In this case, the scattered field is the response of the medium to a single pulse, and the times t_1 and t_2 both occur during the scattering from the same input pulse. Between the correlation times t_1 and t_2 , the medium is assumed to be time-invariant. Using equation (2.98) with the time-dependence of the medium removed, the output correlation is

$$C_{uu}(t_1, t_2) = 4\pi^2 \int_{-\infty}^{\infty} d\omega_1 \int_{-\infty}^{\infty} d\omega_2 U_i(\omega_1)U_i^*(\omega_2)C_{HH}(\omega_1, \omega_2)e^{-i\omega_1 t_1 + i\omega_2 t_2} , \quad (2.103)$$

where C_{HH} is the two-frequency correlation function of the medium, defined as

$$C_{HH}(\omega_1, \omega_2) = \langle H(\omega_0 + \omega_1)H^*(\omega_0 + \omega_2) \rangle . \quad (2.104)$$

For volume scattering, using (2.101), and applying the narrow bandwidth approximation for the input pulse, such that

$$(\omega_0 + \omega)^2 \approx \omega_0^2 , \quad (2.105)$$

the two-frequency correlation function can be approximated as

$$C_{HH}(\omega_1, \omega_2) = 4\pi^2 A |\Gamma(\mathbf{r})|^2 e^{-i(\omega_1 - \omega_2)(r_0 - r)/c_0} \int_{-\infty}^0 dz_c \int_{hs} d\mathbf{r}_d \times \quad (2.106)$$

$$C(\mathbf{r}_d) e^{-2\alpha z_c} e^{-i\text{Re}[\mathbf{k}_d] \cdot \mathbf{r}_d} e^{-i\mathbf{k}_{d1} \cdot (\mathbf{r}_c + \mathbf{r}_d/2)} e^{-i\mathbf{k}_{d2} \cdot (\mathbf{r}_c + \mathbf{r}_d/2)},$$

where \mathbf{r}_c is the location of the center of a patch of area A . Note that A is a small area (defined by performing the x_c and y_c integrations in (2.106)), not the entire ensonified area of the seafloor as the pulse travels in time [47]. As in section 2.4, the function $C(\mathbf{r}_d)$ is the correlation function of the stationary random fluctuations in the medium. The wave vector \mathbf{k}_d is defined in terms of the carrier frequency ω_0 . The wave vectors \mathbf{k}_{d1} and \mathbf{k}_{d2} are defined in terms of ω_1 and ω_2 , respectively.

The correlation of the output signal is then found using (2.103) and (2.106) and performing the integrations with respect to ω_1 and ω_2 :

$$C_{uu}(t_1, t_2) = 4\pi^2 A |\Gamma(\mathbf{r})|^2 \int_{-\infty}^0 dz_c \int_{hs} d\mathbf{r}_d \times \quad (2.107)$$

$$u_i(t_1 - t') u_i^*(t_2 - t'') C(\mathbf{r}_d) e^{-2\alpha z_c} e^{-i\text{Re}[\mathbf{k}_d] \cdot \mathbf{r}_d}.$$

The time delays t' and t'' are functions of the distance traveled through the UHS and into the LHS medium,

$$t' = (\hat{\mathbf{i}} - \hat{\mathbf{s}}) \cdot (\mathbf{r}_c + \mathbf{r}_d/2)/c - t_0 \quad (2.108)$$

$$t'' = (\hat{\mathbf{i}} - \hat{\mathbf{s}}) \cdot (\mathbf{r}_c - \mathbf{r}_d/2)/c - t_0,$$

where

$$t_0 = (r_0 - r)/c_0. \quad (2.109)$$

The delay times are complex due to attenuation in the LHS. The unit vectors $\hat{\mathbf{i}}$ and $\hat{\mathbf{s}}$ define the incident and scattering directions in the medium, such that

$$(\hat{\mathbf{i}} - \hat{\mathbf{s}}) = \frac{\mathbf{k}_d}{\text{Re}[\mathbf{k}]} \quad (2.110)$$

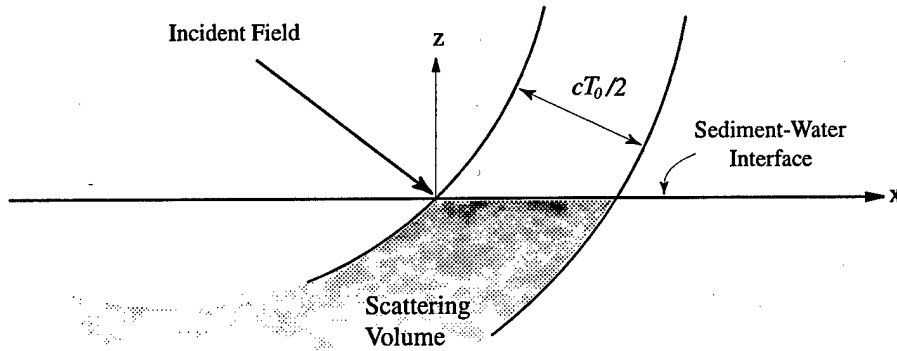


Figure 2.5: Scattering of a pulse of duration T_0 from a random half-space.

The translated and distorted pulse replica $u_i(t - t')$ in (2.107) is defined using an inverse Fourier transform with a complex time delay:

$$u_i(t - t') = \int_{-\infty}^{\infty} U_i(\omega) e^{-i\omega(t-t')} d\omega . \quad (2.111)$$

In general, equation (2.107) can be considered a convolution of the ensonified volume and the medium correlation function over the volume of the scattering region. The pulse volume can be complicated due to refraction across the interface and attenuation in the lower medium. However, if the pulse envelope is a simple square wave, the ensonified volume can be defined approximately in terms of its pulse duration T_0 (see Figure 2.5). If the ensonified volume in the sediment is large compared to the correlation scale of the medium,

$$\frac{cT_0}{2} \gg l_c , \quad (2.112)$$

the convolution can be ignored. The correlation function for the time-domain scattered field can then be approximated using the single frequency correlation result of (2.67).

2.7 Volume Scattering from a Periodic Random Medium

It is sometimes convenient to assume a plane incident wave, as opposed to a spherical wave originating at a point source such as (2.52). This will become especially apparent in Chapter 4 when numerical methods for volume scattering will be discussed. However, by assuming an incident plane wave, the horizontal extent of the scattering volume must be extended to infinity. A simple method of handling the infinite horizontal dimension is to assume periodicity of the random medium in the horizontal. This is fundamentally a different problem than volume scattering from the seafloor, since the seafloor is not periodic. However, by assuming the period is much larger than the correlation length of the medium, a single period will contain a sufficient statistical description of the medium. Then, the scattered field from the periodic medium can be assumed to be representative of a nonperiodic medium with the same statistics. This is only true at particular scattering angles (corresponding to the Floquet modes), as will be discussed.

Therefore, consider a plane wave incident on an infinite two-dimensional half-space. If the lower half-space is periodic in the x -direction with period L , such that the random fluctuations in the medium satisfy the conditions

$$\begin{aligned}\gamma_{\kappa}(x, z) &= \gamma_{\kappa}(x + L, z) , \\ \gamma_{\rho}(x, z) &= \gamma_{\rho}(x + L, z) ,\end{aligned}\tag{2.113}$$

and $l_c \ll L$, then using Floquet's theorem [29, 80] the scattered field can be written as

$$p(x, z) = \tilde{p}(x, z)e^{ik_{ix}x} ,\tag{2.114}$$

where $\tilde{p}(x, z) = \tilde{p}(x + L, z)$ and $k_{ix} = k_0 \cos \theta_i$. The integral equation for scattering

from the periodic volume, similar to (2.38), is

$$p_s(x, z) = \sum_{m=-\infty}^{\infty} \int_{-L/2+mL}^{L/2+mL} dx' \int_{-\infty}^0 dz' [\bar{k}^2 \gamma_\kappa(x', z') g_0(x, z; x', z') p(x', z') + \gamma_\rho(x', z') \nabla' g_0(x, z; x', z') \cdot \nabla' p(x', z')] . \quad (2.115)$$

With the change of variables $x'' = x' - mL$ and $z'' = z'$, and applying the periodic boundary conditions, the integral can be rewritten as

$$p_s(x, z) = \int_{-L/2}^{L/2} dx'' \int_{-\infty}^0 dz'' [\bar{k}^2 \gamma_\kappa(x'', z'') \tilde{g}_0(x, z; x'', z'') p(x'', z'') + \gamma_\rho(x'', z'') \nabla'' \tilde{g}_0(x, z; x'', z'') \cdot \nabla'' p(x'', z'')] , \quad (2.116)$$

where \tilde{g}_0 is the periodic Green's function defined as

$$\tilde{g}_0(x, z; x'', z'') = \sum_{m=-\infty}^{\infty} g_0(x, z; x'' + mL, z'') e^{ik_{ix}mL} . \quad (2.117)$$

Using the definition of the half-space Green's function in two dimensions, similar to (2.33), and applying the Poisson sum formula,

$$\sum_m e^{i(k_x - k_{ix})mL} = \frac{2\pi}{L} \sum_m \delta(k_x - k_{ix} - 2\pi m/L) , \quad (2.118)$$

the periodic half-space Green's function for the LHS is found to be

$$\tilde{g}_0(x, z; x'', z'') = \frac{i}{(2L)} \sum_{m=-\infty}^{\infty} \frac{1}{\beta_m} [R(k_{xm}) e^{i\beta_m|z+z''|} + e^{i\beta_m|z-z''|}] e^{ik_{xm}(x-x'')} , \quad (2.119)$$

where

$$k_{xm} = k_{ix} + 2\pi m/L \quad (2.120)$$

and

$$\beta_m = \sqrt{\bar{k}^2 - k_{xm}^2} \quad (2.121)$$

correspond to the Floquet modes of the periodic medium.

The periodic Green's function for transmission from the lower to the upper medium, similar to (2.29), is found to be

$$\tilde{g}_0(x, z; x'', z'') = \frac{i}{(2L)} \sum_{m=-\infty}^{\infty} \frac{T'(k_{xm})}{\beta_m} e^{i\beta_{0m}z - i\beta_m z''} e^{ik_{xm}(x-x'')}, \quad (2.122)$$

where $\beta_{0m} = \sqrt{k_0^2 - k_{xm}^2}$.

2.7.1 Scattering Cross-Section of a Periodic Random Medium

In the strict sense of the definition, the scattering strength does not exist for an infinite periodic medium because the far field of an infinite scattering region does not exist. However, in a practical sense, defining a scattering strength is still useful, especially for comparisons with non-periodic scattering. Therefore, assume the periodic medium is of some finite and large extent. The total field scattered from the finite periodic half-space can then be approximated as the sum of all the propagating Floquet modes of an infinite medium,

$$p_s(x, z) = \sum_{m=N_1}^{N_2} p_{sm} e^{ik_{xm}x + i\beta_{0m}z}, \quad (2.123)$$

where N_1 and N_2 define the range of modes for which β_{0m} is real. The scattered field for each mode p_{sm} is defined using (2.116) and the Green's function (2.122) as

$$p_{sm} = \int_{-L/2}^{L/2} dx' \int_{-\infty}^0 dz' [k^2 \gamma_\kappa(x', z') \check{g}_m(x', z') p(x', z') + \gamma_\rho(x', z') \nabla' \check{g}_m(x', z') \cdot \nabla' p(x', z')], \quad (2.124)$$

with

$$\check{g}_m(x', z') = \frac{i}{2L} \frac{T'(k_{xm})}{\beta_m} e^{-i\beta_m z' - ik_{xm}x'}. \quad (2.125)$$

The differential scattering cross-section as a function of scattering angle is found by relating the total scattered field (2.123) to the total scattering cross-section.

The total equivalent surface scattering cross-section for the region is defined as the integral of the differential cross-section over the scattering directions,

$$\begin{aligned}\sigma_{ts} &= \int_0^\pi \sigma_s(\theta_s) d\theta_s \\ &= \int_{-k_0}^{k_0} \frac{\sigma_s(k_x)}{k_0 \sin \theta_s} dk_x ,\end{aligned}\quad (2.126)$$

with $k_x = k_0 \cos \theta_s$. For the periodic medium, the integral is replaced by a summation over the propagating modes,

$$\sigma_{ts} = \sum_{m=N_1}^{N_2} \frac{\sigma_s(k_{xm})}{k_0 \sin \theta_{sm}} \frac{2\pi}{L} ,\quad (2.127)$$

with $dk_x = 2\pi/L$, and with θ_{sm} being the scattering angles in the far-field associated with the propagating modes.

Equivalently, the total scattering cross-section can be defined in terms of the incident and scattered power flux density [29] as

$$\sigma_{ts} = \frac{\int_{S_0} \mathbf{I}_s \cdot d\mathbf{a}}{I_i L} ,\quad (2.128)$$

where the area S_0 is an arbitrary surface enclosing the UHS, and $d\mathbf{a}$ is the differential area vector normal to the surface. The area integral will be rewritten as an integral of the normal component of the power flux over a line just above the interface,

$$\sigma_{ts} = \frac{\int_{-\infty}^{\infty} \mathbf{I}_s \cdot \hat{z} dx}{I_i L} ,\quad (2.129)$$

where

$$\mathbf{I}_s \cdot \hat{z} = \frac{1}{2\rho_0\omega} \text{Im} \left[\langle p_s \frac{\partial p_s^*}{\partial z} \rangle \right] .\quad (2.130)$$

Using the plane wave intensity of the incident field,

$$I_i = \frac{1}{2\rho_0 c_0} ,\quad (2.131)$$

and exploiting the orthogonality of the Floquet modes in (2.123) to perform the integration over x , the total scattering cross-section is found in terms of a summation over propagating modes:

$$\sigma_{ts} = \sum_{m=N_1}^{N_2} \langle |p_{sm}|^2 \rangle \sin \theta_{sm} . \quad (2.132)$$

Equating expressions (2.132) and (2.127), it is evident that the discrete differential cross-section for a periodic medium can be found as a function of the discrete scattering directions associated with each Floquet mode:

$$\sigma_s = \frac{L}{2\pi} k_0 \sin^2 \theta_{sm} \langle |p_{sm}|^2 \rangle . \quad (2.133)$$

Chapter 3

NUMERICAL METHODS FOR VOLUME SCATTERING

The basic solution strategy of most numerical methods is to reduce the equations governing a particular problem into a matrix equation, and then solve for the unknowns using efficient matrix inversion techniques. Such methods are widely applied to wave propagation and scattering problems: finite difference, finite element, finite volume, etc. Each method begins by formulating the wave solution as either a partial differential equation with specified boundary and initial conditions or by formulating an integral equation solution. In this chapter, the discussion of numerical solutions to the volume scattering problem will be limited to the single frequency integral equation solution using the *method of moments*. Overviews of this and other numerical methods for wave scattering can be found in texts on the subject [24, 57] and in review articles with extensive bibliographies [18, 81], for example. For an application of a finite-difference time-domain solution to surface scattering, see [25], and for finite-volume methods for volume scattering see [44].

The selection of a particular numerical method should follow from the geometry and boundary conditions of the problem at hand and the type of solution desired (time or frequency domain, far-field, etc.). Without presenting a review of merits and weaknesses of other common numerical methods, the method of moments (MoM) is chosen for several reasons. For one, sediment volume scattering is generally confined to a layer near the sediment-water interface (due to loss in the medium). Therefore, the size of the scattering volume and the resulting number of unknowns in the numerical solution is limited. This allows a MoM solution of the volume scattering integral equation to be used. In general, a numerical solution using an integral equa-

tion formulation would not be well-suited for volume scattering problems because of the size of the solution domain.

Since it can be used, the MoM solution benefits from the integral equation formulation of the problem. The integral operator contains the Green's function and therefore the complete boundary conditions of the problem. There is no need to approximate the discontinuity and boundary conditions at the half-space interface by discretization. The half-space Green's function is calculated separately to any desired accuracy using standard numerical wavenumber integration techniques. This eliminates the problems of grid dispersion suffered by FD and FEM methods [57]. The use of the Green's function in the CW integral equation also properly accounts for absorption in the medium. Absorption is more difficult to model in the time domain. Finally, the integral equation MoM solution only requires the discretization of the scattering volume rather than the entire volume enclosing the scattering medium.

Perhaps the most important benefit, for purposes of this thesis, is that the MoM solution of scattering using the IE formulation is easily compared with the small perturbation solution. The small perturbation method for volume scattering is also formulated as an integral equation (see Chapter 2), which can then be handled numerically using the MoM strategy. The resulting matrix operator is identical to the matrix operator of the exact solution. The perturbation solution is found to various orders by iteration, while the exact solution is found by inversion. Thus, the MoM solution is ideal for studying the accuracy and validity of the perturbation method.

3.1 Method of Moments

To formulate a numerical solution for volume scattering, the integral equation (2.37) is rewritten in operator notation,

$$p(\mathbf{r}) = p_0(\mathbf{r}) + Lp(\mathbf{r}) , \quad (3.1)$$

where L is the linear integro-differential operator of equation (2.38). The operator L has a weakly singular kernel due to the Green's function. The unknown is the field variable $p(\mathbf{r})$. Assume that a solution exists and is given by

$$p(\mathbf{r}) = (I - L)^{-1}p_0(\mathbf{r}) . \quad (3.2)$$

The basic solution strategy is to reduce the linear system into a matrix equation, and then solve for the unknowns using efficient matrix inversion techniques. When the field position \mathbf{r} on both sides of the equality is inside the scattering volume, (3.1) represents an inhomogeneous Fredholm integral equation of the second kind. In general, solution techniques are stable and the resulting matrix equations well-conditioned. In addition, the kernel of the integral operator containing the Green's function (2.33) is a smooth function that decays with distance due to attenuation in the medium. These properties provide a solution matrix which in general will be diagonally dominant and potentially sparse. Efficient numerical methods for matrix operations and storage can then be exploited. After solving for the unknown field inside the volume, the field outside is found by evaluating the integral equation directly using quadrature methods, for example.

The numerical solution begins by expanding the unknown field in a series of suitably chosen *basis* functions f_n :

$$p(\mathbf{r}) = \sum_{n=1}^{\infty} p_n f_n(\mathbf{r}) . \quad (3.3)$$

The function set $\{f_n\}$ forms a true basis if the inner product space forms an orthogonal set,

$$\langle f_m, f_n^* \rangle = 0, \quad n \neq m, \quad (3.4)$$

where $\langle \rangle$ is the inner product integral, and if the basis set satisfies completeness. Completeness in this context means that any well-behaved function can be represented by the series to any degree of accuracy [24], or

$$\|p(\mathbf{r}) - \sum_{n=1}^{\infty} p_n f_n(\mathbf{r})\| = 0. \quad (3.5)$$

Approximate representations of the field are found by choosing a finite-dimensional subspace of the basis functions,

$$p(\mathbf{r}) \cong \sum_{n=1}^N p_n f_n(\mathbf{r}), \quad (3.6)$$

and solving for the unknown coefficients (p_n) by minimizing the residual

$$R(\mathbf{r}) = p_0(\mathbf{r}) - \sum_{n=1}^N p_n [f_n(\mathbf{r}) - Lf_n(\mathbf{r})]. \quad (3.7)$$

Using the method of weighted residuals and choosing a set of weighting or *testing* functions w_m , the unknown coefficients can be found by forcing the residuals to be orthogonal to the testing functions with the inner product integral [57, 24],

$$\int_V w_m(\mathbf{r}) R(\mathbf{r}) d\mathbf{r} = 0, \quad m = 1, 2, \dots, M. \quad (3.8)$$

The testing functions do not necessarily take the same form as the basis functions.

The problem now reduces to the solution of a system of linear equations, and (3.8) can be rewritten as the matrix equation

$$[\lambda - \mathbf{Z}]\mathbf{p} = \mathbf{p}_0. \quad (3.9)$$

The matrices $\mathbf{Z} = [Z_{mn}]$ and $\boldsymbol{\lambda} = [\lambda_{mn}]$ are of size $M \times N$ with elements

$$\begin{aligned} Z_{mn} &= \int_V w_m(\mathbf{r}) L f_n(\mathbf{r}) d\mathbf{r} , \\ \lambda_{mn} &= \int_V w_m(\mathbf{r}) f_n(\mathbf{r}) d\mathbf{r} . \end{aligned} \quad (3.10)$$

The vector $\mathbf{p}_0 = [p_{0,m}]$ has elements

$$p_{0,m} = \int_V w_m(\mathbf{r}) p_0(\mathbf{r}) d\mathbf{r} . \quad (3.11)$$

The solution vector $\mathbf{p} = [p_n]$ is comprised of the unknown coefficients of the basis function expansion. The matrix \mathbf{Z} will be referred to as the scattering matrix. The major complexity in finding the solution now lies in the calculation of these so called moment integrals (hence the name of the solution method) and the inversion of the resulting matrix $\boldsymbol{\lambda} - \mathbf{Z}$. The complexity involved is a direct consequence of the choice of basis and testing functions.

3.1.1 Perturbation Solution

The small perturbation solution of Section 2.3 can also be written in terms of a matrix equation. Rewrite the perturbation integral equation (2.50) in operator notation as

$$p^{(i+1)}(\mathbf{r}) = L p^{(i)}(\mathbf{r}) , \quad (3.12)$$

where L is the same operator as above. Each lower-order term in the perturbation series is then expanded as a series of basis functions:

$$p^{(i)}(\mathbf{r}) \cong \sum_{n=1}^N p_n^{(i)} f_n(\mathbf{r}) . \quad (3.13)$$

The solution for each higher-order term in the perturbation series involves the multiplication of the scattering matrix and the unknown coefficients of the preceding order:

$$\mathbf{p}^{(i+1)} = \mathbf{Z} \cdot \mathbf{p}^{(i)} . \quad (3.14)$$

The solution vector $\mathbf{p}^{(i+1)} = [p_m^{(i+1)}]$ has elements

$$p_m^{(i+1)} = \int_V w_m(\mathbf{r}) p^{(i+1)}(\mathbf{r}) d\mathbf{r} . \quad (3.15)$$

The scattered field for the perturbation solution can then be found by iteration, where

$$\mathbf{p}_s = \mathbf{p}^{(1)} + \mathbf{p}^{(2)} + \dots . \quad (3.16)$$

Using (3.14) with $M = N$, the total scattered field is found in terms of the scattering matrix:

$$\mathbf{p} = \sum_{n=0}^{\infty} \mathbf{Z}^n \cdot \mathbf{p}_0 . \quad (3.17)$$

For a weakly fluctuating medium, the series will converge rapidly and can be truncated to approximate the complete solution found from (3.9).

3.2 Discretization and Selection of Basis/Testing Functions

The discretization of the volume scattering integral operator into a finite-dimensional subspace of basis functions requires approximations that compromise the solution accuracy for the purpose of computational efficiency. The choice of basis functions is the principal issue in implementing the MoM solution, as discussed in [57] and [24]. The selection influences the accuracy of the approximate solution, the complexity of the computation of the matrix elements, and the size of the scattering matrix. While the solution with the best accuracy is always desired, computational limitations may motivate a less optimal formulation. In some cases, computational resources (memory) put an upper limit on the matrix size. In other cases, the time required to perform computations that create the scattering matrix limits the problem.

The choice of basis and testing functions is, in general, a function of the geometry and boundary conditions of the problem, the expected form of the solution,

and resources at hand. Formally, the basis functions should satisfy conditions of orthogonality and completeness, as discussed previously. However, approximate solutions can still be found regardless of whether w_n and f_n form true basis sets. In practice, the functions are often not orthogonal. This creates difficulties in deriving analytic statements about the numerical convergence of the approximation [57]. Convergence is usually shown numerically by comparing the approximate solution with exact solutions as $N \rightarrow \infty$.

Many types of basis functions are applied in the current literature: Dirac delta functions, rectangular pulse functions, triangle or roof-top functions, quadratic splines, and Lagrangian polynomials, for example. Some of these form orthogonal bases and others do not. In general, lower interpolation error is achieved with higher-order basis functions (e.g., high polynomial order). However, in practice a trade-off must be made between accuracy, computational efficiency, and general applicability of the solution method to a range of problem geometries. For volume scattering, this trade-off is especially noticeable. The number of unknowns required to provide sufficient accuracy can become very large (compared to similar numerical methods used to solve surface scattering problems). Alternatively, reducing the number of unknowns by selecting higher-order or full-domain basis functions can create numerical complexities that give rise to excessive computation time.

Consider the calculation of (3.10) for volume scattering using (2.38) in two dimensions where $\mathbf{r} = (x, z)$:

$$Z_{mn} = \int_V \int_V w_m(\mathbf{r}) \left[\bar{k}^2 \gamma_\kappa(\mathbf{r}') g_0(\mathbf{r}, \mathbf{r}') f_n(\mathbf{r}') + \gamma_\rho(\mathbf{r}') \nabla' g_0(\mathbf{r}, \mathbf{r}') \cdot \nabla' f_n(\mathbf{r}') \right] d\mathbf{r} d\mathbf{r}' . \quad (3.18)$$

One characteristic of (3.18) that can be exploited is the translational invariance of the half-space Green's function g_0 in the x -direction. This will be used to reduce the number of times g_0 must be calculated. It would also be desirable to simplify the integration in (3.18) such that the integration of the Green's function over the volume

is decoupled from the medium. This would allow the computation for the Green's function (for a specific geometry) to be performed once and then used repeatedly for different realizations of a random medium. These techniques will be apparent in the details of the derivations to follow.

In this section, two types of basis and testing functions will be used to approximate volume scattering. First, *subsectional* basis functions that approximate the field and medium as piecewise-constant over a grid of rectangular cells will be used. Then Fourier basis and testing functions will be used as an example of the use of *full-domain* functions. The subsectional basis functions are non-zero only over a subsection of the domain of L , and usually provide analytically simpler solutions than full-domain functions. Alternatively, full-domain basis functions exist over the entire domain of the operator.

With knowledge of the solution of a particular problem, the choice of full-domain basis functions can provide solutions that have fewer unknowns and are computationally more efficient. The trade-off is usually the generality of the numerical method. In this chapter, the subsectional basis functions will provide the most useful method of solving the half-space volume scattering problem at hand. All numerical results shown will be found using this method. The full-domain solution will be presented only as an example of other alternative and interesting choices that can reduce the complexity of the problem for specific geometries.

3.2.1 Point Matching and Pulse Basis Functions

The most direct solution using MoM is found by choosing testing and basis functions that provide the simplest evaluation of the scattering matrix elements. One choice of testing functions is to require that the solution be satisfied at discrete points in the region of interest. This is accomplished by using Dirac delta functions,

$$w_m(x, z) = \delta(x - x_m)\delta(z - z_m) , \quad (3.19)$$

where x_m and z_m are the discrete points of interest. In doing so, one integral required to evaluate the matrix element is eliminated. This method is referred to as *point matching*.

The simplest choice of basis functions (that also satisfy orthogonality) is the *pulse basis function*,

$$f_n(x, z) = \begin{cases} 1 & \text{if } |x - x_n| \leq \Delta x/2 \text{ and } |z - z_n| \leq \Delta z/2, \\ 0 & \text{otherwise,} \end{cases} \quad (3.20)$$

which exists only over a small rectangle with sides Δx and Δz centered at the n th discretized point. This is equivalent to dividing the scattering volume into small cells over which the field and the medium fluctuations are assumed to be constant:

$$\begin{aligned} p(x, z) &= \sum_{n=1}^{\infty} p(x_n, z_n) f_n(x, z), \\ \gamma_{\kappa}(x, z) &= \sum_{n=1}^{\infty} \gamma_{\kappa}(x_n, z_n) f_n(x, z), \\ \gamma_{\rho}(x, z) &= \sum_{n=1}^{\infty} \gamma_{\rho}(x_n, z_n) f_n(x, z). \end{aligned} \quad (3.21)$$

The coefficient p_n in (3.6) is simply the value of the unknown field over the n th cell, $p_n = p(x_n, z_n)$.

To ensure a meaningful numerical solution, it is necessary to employ a combination of basis and testing functions that have finite and well-defined coefficients throughout the domain of the solution [57]. This heuristic constraint imposes a differentiability requirement on the chosen set of functions - the polynomial degree of a subsectional basis function must increase in proportion to the number of derivatives in the operator. Because the volume scattering operator contains a first derivative, the basis and testing functions must have continuous first derivatives.

To satisfy this requirement and still be able to apply point matching/pulse basis functions, a *weak form* of the volume scattering operator must be used. The first

derivative of the field in (3.18) cannot be eliminated, but can be approximated with finite-difference operators

$$\begin{aligned}\frac{\partial}{\partial x}p(x_n, z_n) &= \frac{1}{2\Delta x}(s_x - s_x^{-1})p(x_n, z_n) \\ &= \frac{1}{2\Delta x}[p(x_{n+1}, z) - p(x_{n-1}, z)]\end{aligned}\quad (3.22)$$

and

$$\begin{aligned}\frac{\partial}{\partial z}p(x_n, z_n) &= \frac{1}{2\Delta z}(s_z - s_z^{-1})p(x_n, z_n) \\ &= \frac{1}{2\Delta z}[p(x, z_{n+1}) - p(x, z_{n-1})],\end{aligned}\quad (3.23)$$

where s_x and s_z and their inverses are shift operators. The matrix elements can then be expressed as

$$\begin{aligned}Z_{mn} &= \iint_{\text{cell}} dx' dz' \left\{ \bar{k}^2 \gamma_\kappa(x', z') g_0(x_m, z_m; x', z') + \right. \\ &\quad \left. \gamma_\rho(x', z') \left[\frac{\partial}{\partial x'} g_0(x_m, z_m; x', z') \frac{1}{2\Delta x} (s_x - s_x^{-1}) + \right. \right. \\ &\quad \left. \left. \frac{\partial}{\partial z'} g_0(x_m, z_m; x', z') \frac{1}{2\Delta z} (s_z - s_z^{-1}) \right] \right\},\end{aligned}\quad (3.24)$$

and

$$\lambda_{mn} = \delta_{mn}, \quad (3.25)$$

where δ_{mn} is the Kronecker delta function. The vector \mathbf{p}_0 contains the unperturbed field points, and the solution vector \mathbf{p} contains the unknown field points: $\mathbf{p}_0 = [p_0(x_m, z_m)]$ and $\mathbf{p} = [p(x_m, z_m)]$. The integral in Z_{mn} is now evaluated over a cell centered at the points of the discretized field.

The elements of the \mathbf{Z} matrix represent the interaction between cells of the discretized field. For cells far apart from each other (off-diagonal elements, $m \neq n$) it is expected that the interaction will be weak due to spreading loss and attenuation in the medium. Elements closer to the matrix diagonal represent the interaction

between neighboring points and are expected to be larger in magnitude than the off-diagonal elements.

Rearranging the order of the finite difference operators and redefining the Green's function, the matrix elements take the form

$$\begin{aligned} Z_{mn} = & \bar{k}^2 \gamma_\kappa(x_n, z_n) \hat{g}_0(x_m, z_m; x_n, z_n) \\ & - \frac{1}{2\Delta x} (s_x - s_x^{-1})_n \left[\gamma_\rho(x_n, z_n) \frac{\partial}{\partial x_n} \hat{g}_0(x_m, z_m; x_n, z_n) \right] \\ & - \frac{1}{2\Delta z} (s_z - s_z^{-1})_n \left[\gamma_\rho(x_n, z_n) \frac{\partial}{\partial z_n} \hat{g}_0(x_m, z_m; x_n, z_n) \right]. \end{aligned} \quad (3.26)$$

The modified Green's function (\hat{g}_0) is the integration of the half-space Green's function over the aperture of the cell:

$$\begin{aligned} \hat{g}_0(x_m, z_m; x_n, z_n) &= \iint_{\text{cell}} g_0(x_m, z_m; x', z') dx' dz' \\ &= \int_{x_m - \frac{\Delta x}{2}}^{x_m + \frac{\Delta x}{2}} \int_{z_m - \frac{\Delta z}{2}}^{z_m + \frac{\Delta z}{2}} g_0(x_m, z_m; x', z') dx' dz'. \end{aligned} \quad (3.27)$$

The finite difference operators in (3.26) operate on the index n of the quantities in the square brackets only.

The integration over each cell in the modified Green's function (3.27) can be performed analytically or numerically. For matrix elements "far from" the diagonal elements, the Green's function in the integrand will vary slowly over each small cell, and the integrand can be assumed to be approximately constant. For matrix elements "near to" the diagonal or on the diagonal, the integrand of (3.27) cannot be assumed to be constant. In this thesis, a simple trapezoid rule numerical integration was found to be sufficiently accurate to approximate the cell integration. The definition of "near to" and "far from" the diagonal is a function of the behavior of the half-space Green's function and the cell size. In general, this must be defined for the specific geometry and medium properties of the problem at hand.

For diagonal elements ($m = n$), the Green's function is singular at the center of the cell. A useful approximation to solve the cell integration is found by first

dividing the Green's function into the direct path and reflected path components,

$$g_0(\mathbf{r}, \mathbf{r}') = -\frac{i}{4} H_0^{(1)}(k(r-r')) + g_r(\mathbf{r}, \mathbf{r}') , \quad (3.28)$$

where $H_0^{(1)}$ is the zeroth-order Hankel function of the first kind. The reflected path Green's function is

$$g_r(\mathbf{r}, \mathbf{r}') = \frac{i}{4\pi} \int_{-\infty}^{\infty} \frac{1}{\beta} R(k_x) e^{i\beta|z+z'|} e^{ik_x(x-x')} dk_x . \quad (3.29)$$

The singularity only exists in the direct path. A simple analytic approximation for the direct path is to replace the integral of the direct path Green's function over the rectangular cell with an integral over an equivalent circular cell [29]. The equivalent circular cell will have radius $a = \sqrt{\Delta x \Delta z / \pi}$. Then, using the identities

$$\int r H_0^{(1)}(kr) dr = \frac{r}{k} H_1^{(1)}(kr) \quad (3.30)$$

and

$$H_1^{(1)}(kr) \approx -i \frac{2}{\pi kr} \quad (3.31)$$

as $r \rightarrow 0$, where $H_1^{(1)}$ is the Hankel function of the first kind and first order, the diagonal matrix elements can be approximated as

$$Z_{mm} = -\frac{i\pi}{2k} \left[a H_1^{(1)}(ka) + \frac{i2}{k\pi} \right] \gamma_\kappa(x_m, z_m) + \left\{ k^2 \gamma_\kappa(x_m, z_m) \hat{g}_r(z_m) - \frac{1}{2\Delta z} (s_z - s_z^{-1})_m \left[\gamma_\rho(x_m, z_m) \frac{\partial}{\partial z_m} \hat{g}_r(x_m, z_m) \right] \right\} , \quad (3.32)$$

where

$$\hat{g}_r(x_m, z_m) = \iint_{\text{cell}} g_r(x_m, z_m; x', z') dx' dz' . \quad (3.33)$$

The integral over the cell of the x -derivative of the reflected path and the x - and z -derivatives of the direct path Green's functions are zero due to symmetry. Again, the cell integration in the reflected path Green's function can be performed numerically

or analytically. However, now the integration over the singularity in the direct path is performed analytically.

For a periodic random medium, the matrix equations and the calculation of the matrix elements remain the same, except for the Green's function. The wavenumber integration in the half-space Green's function for the non-periodic case is replaced by a summation over Floquet modes. The cell integration is performed in the same manner, and equations (3.26) and (3.32) are unchanged. However, equation (3.27) is now defined in terms of the periodic Green's function

$$\hat{g}_0(x_m, z_m; x_n, z_n) = \int_{\text{cell}} \tilde{g}_0(x_m, z_m; x', z') dx' dz' . \quad (3.34)$$

Also, equation (3.33) is replaced by

$$\hat{g}_r(x_m, z_m) = \iint_{\text{cell}} \tilde{g}_r(x_m, z_m; x', z') dx' dz' , \quad (3.35)$$

where (3.29) is replaced by

$$\tilde{g}_r(x_m, z_m; x', z') = \frac{i}{2L} \sum_{j=-\infty}^{\infty} \frac{1}{\beta_j} R(k_{xj}) e^{ik_{xj}(x_m-x')} e^{i\beta_j|z_m+z'|} . \quad (3.36)$$

3.2.2 Fourier Testing and Basis Functions

When using the point matching method to evaluate realistic volume scattering problems the number of unknowns can become very large. An alternative choice of testing and basis functions is one that reduces the size of the problem, the general strategy being to sacrifice the simplicity of evaluating the matrix elements in return for reducing the dimension of the matrix equation. One way this can be accomplished is by using full-domain basis functions. If the basis functions are chosen such that the unknown field is well defined by a smaller set of unknowns (compared to point matching), then the dimension of the problem can be greatly reduced.

A convenient choice, at least in the case of a periodic random medium, is to use Fourier basis and testing functions,

$$p(x, z) = \sum_{l=-N_k/2}^{N_k/2-1} P_l(z) e^{ik_{xl}x}, \quad (3.37)$$

$$w_m(x, z) = W_i(z) e^{-ik_{xj}x},$$

where N_k is the number of terms in the Fourier series. The field is expanded in the x -direction only where $k_{xl} = 2\pi l/L + k_{ix}$, and P_l is the depth-dependent Fourier coefficient. The testing function w_m is also an x -direction Fourier component with depth dependence. The indexing is defined over two dimensions such that $m = (i, j)$. In addition to expanding the unknown field, the medium is also expanded as a Fourier series:

$$\gamma_\kappa(x, z) = \sum_{v=-N_k/2}^{N_k/2-1} A_v(z) e^{i2\pi vx/L}, \quad (3.38)$$

$$\gamma_\rho(x, z) = \sum_{v=-N_k/2}^{N_k/2-1} B_v(z) e^{i2\pi vx/L}.$$

For a periodic medium with continuous fluctuation and no sharp discontinuities, the series can be limited to a finite number of terms (N_k) to sufficiently represent the unknown field.

Using the above expansions in the periodic integral equation (2.116), and exploiting the orthogonality of the Fourier components, the inner product integration of the method of moments reduces to the form

$$\int_V w_m(\mathbf{r}) Lp(\mathbf{r}) d\mathbf{r} = L^2 \int_{-\infty}^0 W_i(z) dz \int_{-\infty}^0 \sum_{l=-N_k/2}^{N_k/2-1} \left[\bar{k}^2 A_{(j-l)}(z') P_l(z') \tilde{g}_j(z, z') \right. \\ \left. - B_{(j-l)}(z') \left(k_{xl} k_{xj} P_l(z') \tilde{g}_j(z, z') - \frac{\partial P_l(z')}{\partial z'} \frac{\partial \tilde{g}_j(z, z')}{\partial z'} \right) \right] dz', \quad (3.39)$$

where

$$\tilde{g}_j(z, z') = \frac{i}{2\beta_j L} \left[R(k_{xj}) e^{i\beta_j |z+z'|} + e^{i\beta_j |z-z'|} \right]. \quad (3.40)$$

In general, W_i , P_l , A_v , and B_v are arbitrary functions of the depth coordinate z . The simplest form they can take, since the medium is not periodic in depth, is to require point matching,

$$W_i(z) = \delta(z - z_i), \quad (3.41)$$

and pulse basis functions in the z -direction,

$$\begin{aligned} P_l(z) &= \sum_{k=1}^{N_z} p_{kl} f_k(z), \\ A_v(z) &= \sum_{u=1}^{N_z} a_{uv} f_u(z), \\ B_v(z) &= \sum_{u=1}^{N_z} b_{uv} f_u(z), \end{aligned} \quad (3.42)$$

where

$$f_n(z) = \begin{cases} 1 & \text{if } |z - z_n| \leq \Delta z/2, \\ 0 & \text{otherwise.} \end{cases} \quad (3.43)$$

This is equivalent to slicing the medium at each value of z and performing a Fourier transform in the x -direction on each slice.

The unknown field and the random medium are now expressed as a two-dimensional grid of coefficients. To write the system as a matrix equation, it is necessary to arrange the unknowns as a vector. This is done by numbering the two-dimensional grid of coefficients with a single one-dimensional index defined as $m = i + jN_z$ and $n = k + lN_z$. Using the above testing and basis functions and the vector indexing of the coefficients, the elements of the \mathbf{K} matrix are found to be

$$\begin{aligned} Z_{mn} &= L^2 \Delta z \left[k^2 a_{k(j-l)} \tilde{g}_j(z_i, z_k) - k_{xl} k_{xj} b_{k(j-l)} \tilde{g}_j(z_i, z_k) \right. \\ &\quad \left. - \frac{1}{2\Delta z} (s_z - s_z^{-1})_k \left(b_{k(j-l)} \frac{\partial \tilde{g}_j(z_i, z_k)}{\partial z_k} \right) \right]. \end{aligned} \quad (3.44)$$

Again, the derivatives in the z -direction have been approximated using the finite difference operator, and the integration over each cell in the z -direction approximated as in Section 3.2.1.

3.3 Monte-Carlo Simulations

Monte-Carlo simulations of volume scattering from a two dimensional random medium are performed to develop first and second moment statistics of the scattered field. The translational invariance of the Green's function in the horizontal direction can be exploited to reduce computation and memory usage. Only a subset of the entire set of Green's function calculations is performed. Since the field points do not change position from realization to realization, the Green's function calculations are only performed once for a set of realizations. This greatly simplifies the numerical solution. In addition, since the unknown field points are discretized on a uniform grid, the wavenumber integration of the half-space Green's function (2.33) can be performed efficiently using an FFT (see Appendix D).

3.3.1 Incident Field

To avoid the interaction of volume elements at the side boundaries of a non-periodic scattering volume, a Gaussian tapered incident field is used. The incident field is defined at the interface of the half-space as a Gaussian aperture function:

$$p_0(x, z = 0) = e^{-x^2/g^2} e^{ik_0 x \cos \theta_i} . \quad (3.45)$$

The field below the interface is found by taking the inverse Fourier transform of the spectral representation of the aperture function and propagating the field in the negative z -direction:

$$p_0(x, z < 0) = \frac{g}{2\sqrt{\pi}} \int_{-\infty}^{\infty} T(k_x) e^{-(k_x - k_0 \cos \theta_i)^2 g^2 / 4} e^{ik_x x - i\beta z} dk_x . \quad (3.46)$$

The incident power, S_i , is found by integrating the normal component of the energy flux over the interface:

$$S_i = \frac{1}{2\rho_0\omega} \int_{-\infty}^{\infty} \text{Im} \left[p_0(x, z = 0^+) \frac{\partial p_0^*(x, z = 0^+)}{\partial z} \right] dx . \quad (3.47)$$

Due to the orthogonality of Fourier components, the integral over x is eliminated and the incident power is found to be a function of a single integral over the propagating wavenumbers in the upper medium:

$$S_i = \frac{g^2}{4\omega\rho_0} \int_{-k_0}^{k_0} \beta_0 e^{-(k_x - k_0 \cos \theta_i)^2 g^2 / 2} dk_x . \quad (3.48)$$

For a periodic random medium, the incident field will be taken to be a simple unit amplitude plane wave. The plane wave field is incident to the interface at the angle θ_i , and it will refract into the volume such that

$$p_0(x, z < 0) = T(k_{ix}) e^{ik_{ix}x - \beta_i z} , \quad (3.49)$$

where $k_{ix} = k_0 \cos \theta_i$, $\beta_i = \sqrt{k_0^2 - k_{ix}^2}$, and T is the plane wave transmission coefficient. The incident intensity immediately above the interface is

$$I_i = \frac{1}{2c_0\rho_0} . \quad (3.50)$$

Figures 3.1a and 3.2a illustrate typical geometries and incident fields used for the numerical simulations.

3.3.2 Realization of a Random Medium

Realizations of a two-dimensional Gaussian random medium are generated by Fourier synthesis (see Appendix E). The assumption of Gaussian statistics is made only for convenience. The medium has an exponential correlation function and power-law spectrum, as described in Section 2.1.1. The correlation function is

$$C(\mathbf{r}) = \sigma^2 e^{-r/l_c} , \quad (3.51)$$

where l_c is the correlation length and σ^2 is the variance of the media fluctuations (either density or compressibility fluctuations). The corresponding two-dimensional power law spectrum is

$$S(\mathbf{k}) = \frac{\sigma^2 / (2\pi l_c)}{(1/l_c^2 + k^2)^{3/2}} . \quad (3.52)$$

Typical realizations of density fluctuation using a power law spectrum are shown in Figures 3.1b and 3.2b. The size of the volume is constrained by the incident field and statistical convergence of the numerical solution.

3.3.3 Statistical Convergence and Accuracy

Statistical convergence with respect to the random parameters of the model must be demonstrated for the Monte-Carlo simulations. For volume scattering simulations, convergence must be shown with respect to the size of the volume (in number of wavelengths), the resolution of the volume discretization (number of points per wavelength), and the number of realizations used to form ensemble averages. The minimum size of the volume and the minimum number of discretized points is a function of the correlation length of the medium. A smaller correlation length may permit a smaller volume to adequately represent the statistics of the medium; however, it may require more discretized points per wavelength. Convergence with respect to these parameters must also be shown for a range of correlation lengths.

Three convergence tests are performed using two values of correlation lengths ($l_c/\lambda = 0.5$ and $l_c/\lambda = 1.0$), chosen to represent typical correlation lengths of marine sediments for high-frequency scattering. Figure 3.3 shows convergence of the numerically calculated total scattering strength as a function of the number of points per wavelength and the number of wavelengths in the scattering volume. The total scattering cross-section is found using a two-dimensional version of (2.92). The numerical simulations converge for the medium discretized with at least 10 points per wavelength and greater. With respect to the size of the volume (L_x/λ), the numerical estimates show good convergence even with small volumes. All of the horizontal dimensions tested ($4 < L_x/\lambda < 25$) show good convergence. Figure 3.4 shows convergence with respect to the number of realizations. A minimum of 50 realizations is necessary to form ensemble averages for the types of media used in this test ($N_x\lambda/L_x = 10$ and $L_x/\lambda = 6.4$).

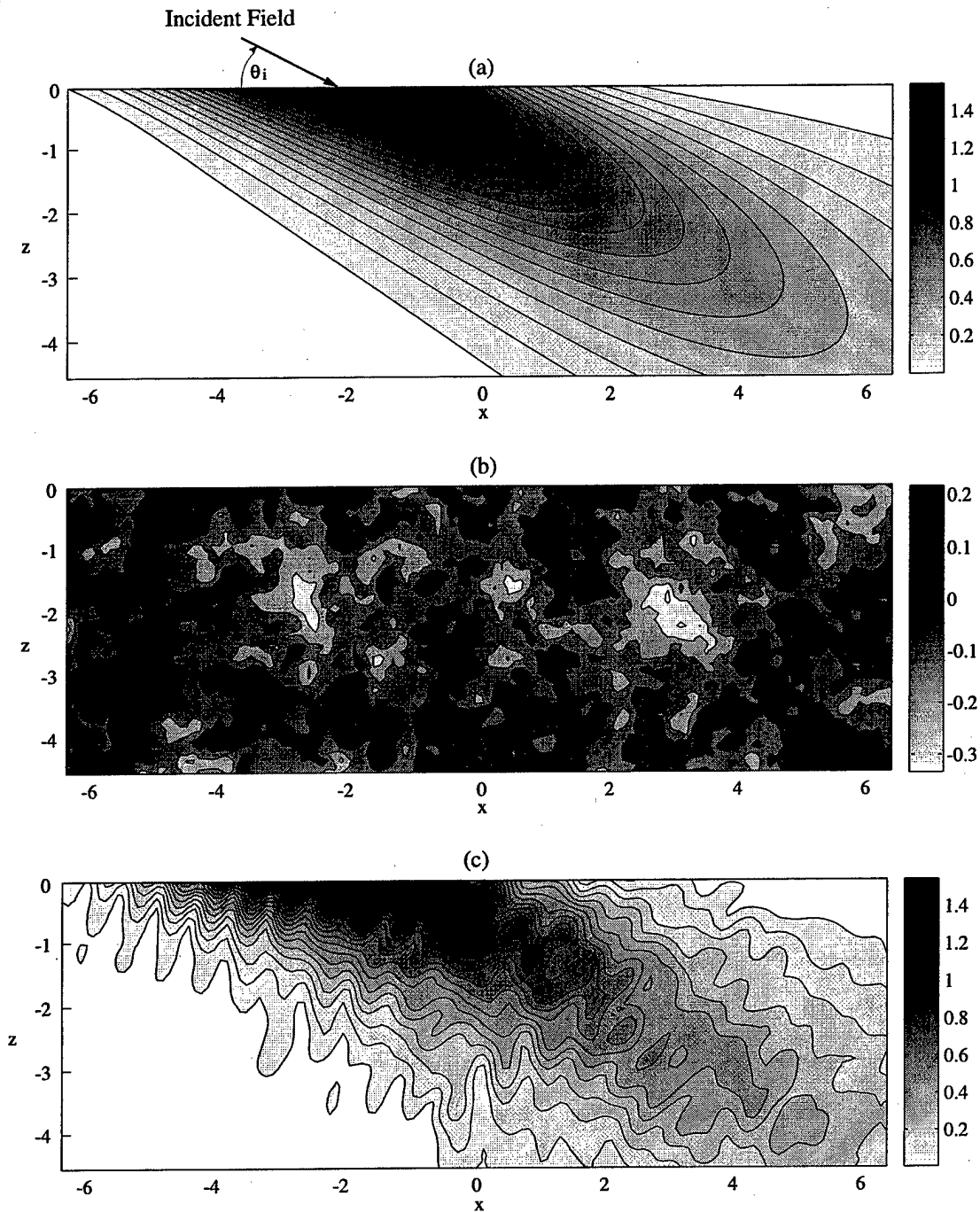


Figure 3.1: Simulation of volume scattering in a non-periodic medium: (a) The tapered incident field $|p_0(x, z)|$; (b) a realization of a Gaussian random medium $\gamma_\rho(x, z)$; and (c) the solution for the total scattered field $|p(x, z)|$. The incident field is above critical at $\theta_i = 35^\circ$, $l_c = 0.5\lambda$, $\sigma_\rho = 0.10$, $\mu = -1.1$, $\bar{\rho}/\rho_0 = 2.0$, $\bar{c}/c_0 = 1.1$, $\delta = 0.02$, with 10 points per wavelength. All coordinates are normalized by the wavelength.

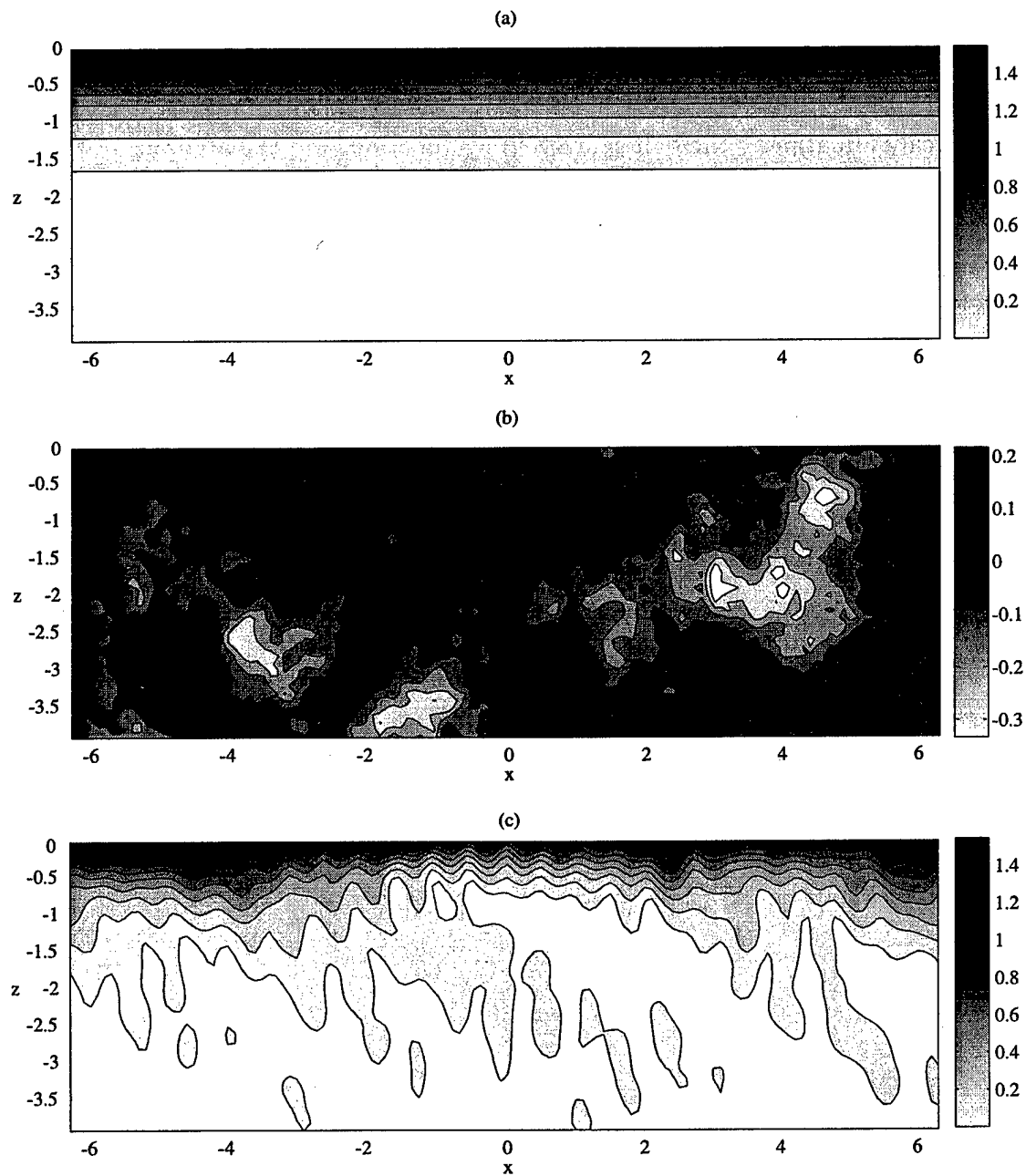


Figure 3.2: Simulation of volume scattering in a periodic medium: (a) The plane incident field $|p_0(x, z)|$; (b) a realization of a Gaussian random medium $\gamma_\rho(x, z)$; and (c) the solution for the total scattered field $|p(x, z)|$. The incident field is subcritical at $\theta_i = 20^\circ$, $l_c = 1.0\lambda$, $\sigma_\rho = 0.10$, $\mu = -2.0$, $\bar{\rho}/\rho_0 = 2.0$, $\bar{c}/c_0 = 1.1$, $\delta = 0.02$, with 10 points per wavelength. All coordinates are normalized by the wavelength.

The accuracy of the simulation method can be evaluated by comparing the numerical results with the solution of problems that can be solved analytically. The comparison will test applicability of the choice of basis functions, the accuracy of the numerical evaluation of the half-space Green's function, and the accuracy of the cell integration methods. Simulating the phase matching conditions required to model perfect reflection and transmission in a non-random medium will provide an upper bound on the numerical errors of the random medium simulations.

Consider the transmission of an incident plane wave into an infinite half-space with a linear profile (in depth) of the square of the index of refraction ($\gamma_\kappa = az$) and constant density profile ($\gamma_\rho = b$). The wave equation for this case can be written as

$$\nabla^2 \Phi(x, z) + \bar{k}^2 \left[\frac{1 + az}{1 - b} \right] \Phi(x, z) = 0, \quad (3.53)$$

where

$$\Phi(x, z) = \frac{p(x, z)}{\sqrt{\rho_0}}. \quad (3.54)$$

The solution for the field in the LHS is well known [11, 49], and is expressed as an Airy function

$$\Phi(x, z) = W(k_x) \text{Ai}[t(z)] e^{ik_x x}, \quad (3.55)$$

where

$$\begin{aligned} t(z) &= t_0 - z/H, \\ H &= (a\bar{k}^2)^{-1/3}, \\ t_0 &= H^2[k_x^2 - \bar{k}^2] \\ W(k_x) &= \frac{2i\rho\beta_0 H}{\rho_0 \text{Ai}'(t_0) + i\rho\beta_0 \text{Ai}(t_0) H}. \end{aligned} \quad (3.56)$$

Figure 3.5 shows the numerical results of the test case for a non-periodic medium with a normally incident tapered field. The analytic solution for the tapered field is found by performing a plane wave decomposition and applying (3.55) to each Fourier

component of the field. Figure 3.6 shows the results of the test case for a periodic medium with a plane incident wave. The sound speed gradient in both cases is defined with $\bar{c}/c_0 = 1.2$, $\bar{\rho}/\rho_0 = 2.0$, $a = -0.05$ and $b = 0.1$. The piecewise constant curves (stepped curves) are the numerical MoM solutions. The solid curves are the analytic results, and the dashed curves are the incident fields. A discretization of 10 points per wavelength was used in the simulations. The MoM solution compares well with the analytic results for both cases.

3.3.4 Matrix Inversion

In this thesis, an iterative conjugate gradient method was used to perform the matrix inversion [58]. No approximations were used to reduce the size of the matrix. For the problems considered, this standard method was sufficiently accurate and computationally efficient. A scattering matrix for sediment volume scattering is typically 8192×8192 matrix elements in size (corresponding to a volume of length 12.8λ and depth 6.4λ discretized with 10 points per wavelength). For larger problems, sparse matrix methods or other numerical approximations that exploit the loss in the medium in order to reduce the size of the scattering matrix could be considered [18, 78]. However, the effort required to improve the numerical efficiency of a particular solution must be weighed against the ever-increasing computational resources that are becoming available each year at decreasing costs.

An alternative to matrix inversion techniques is to use the numerical small perturbation method of Section 3.1.1. Some problems that lie outside the range of validity of first-order perturbation theory can still be solved with sufficient accuracy using higher-order perturbation approximations. The perturbation solution can be found to any higher order by efficient matrix multiplications using (3.14). An example is shown in Figure 3.7. The scattering strength (as defined in Section 2.5) is found using both the numerical perturbation method and by matrix inversion (using the conjugate gradient method). Each higher-order perturbation solution (plotted as

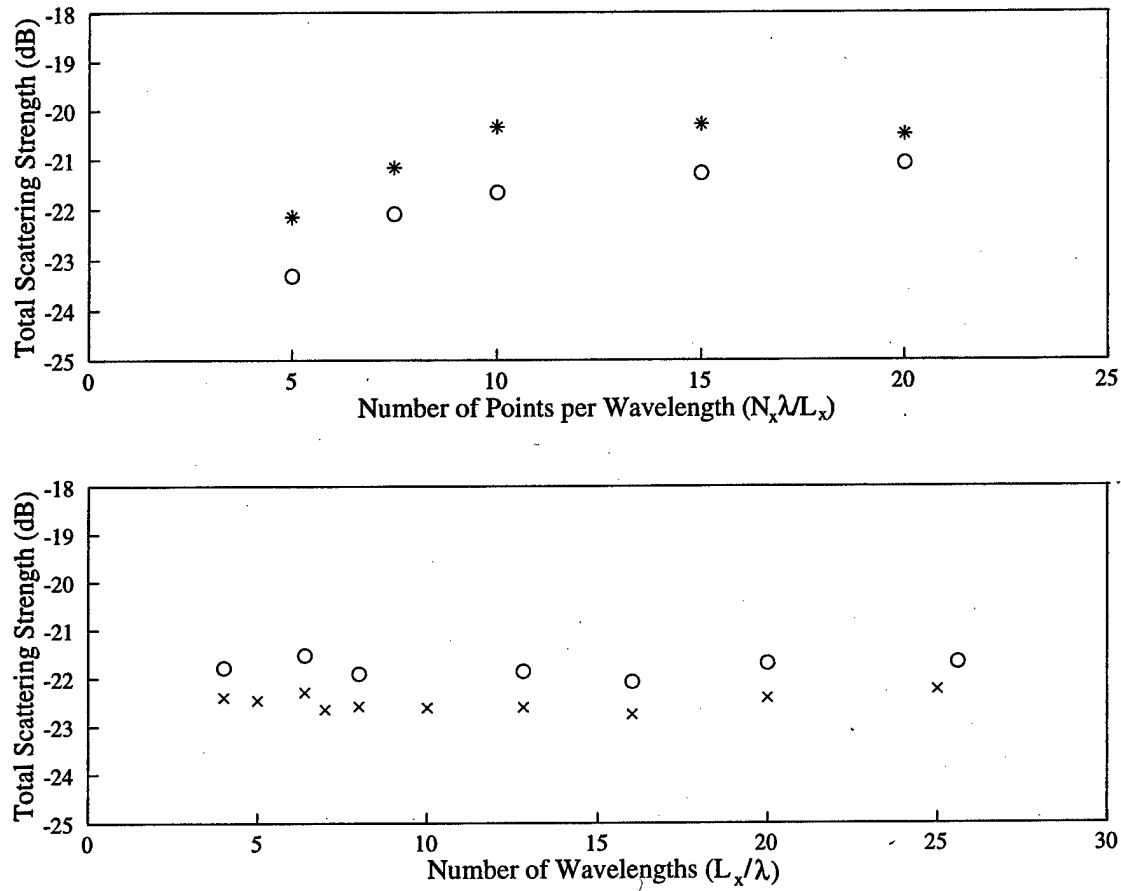


Figure 3.3: Monte-Carlo convergence with respect to: (a) the number of points per wavelength; and (b) the size of the medium. The symbol * represents $l_c = 0.2\lambda$, the o represents $l_c = 0.5\lambda$, and the \times represents $l_c = 1.0\lambda$. A total of 50 realizations was used to estimate the ensemble average.

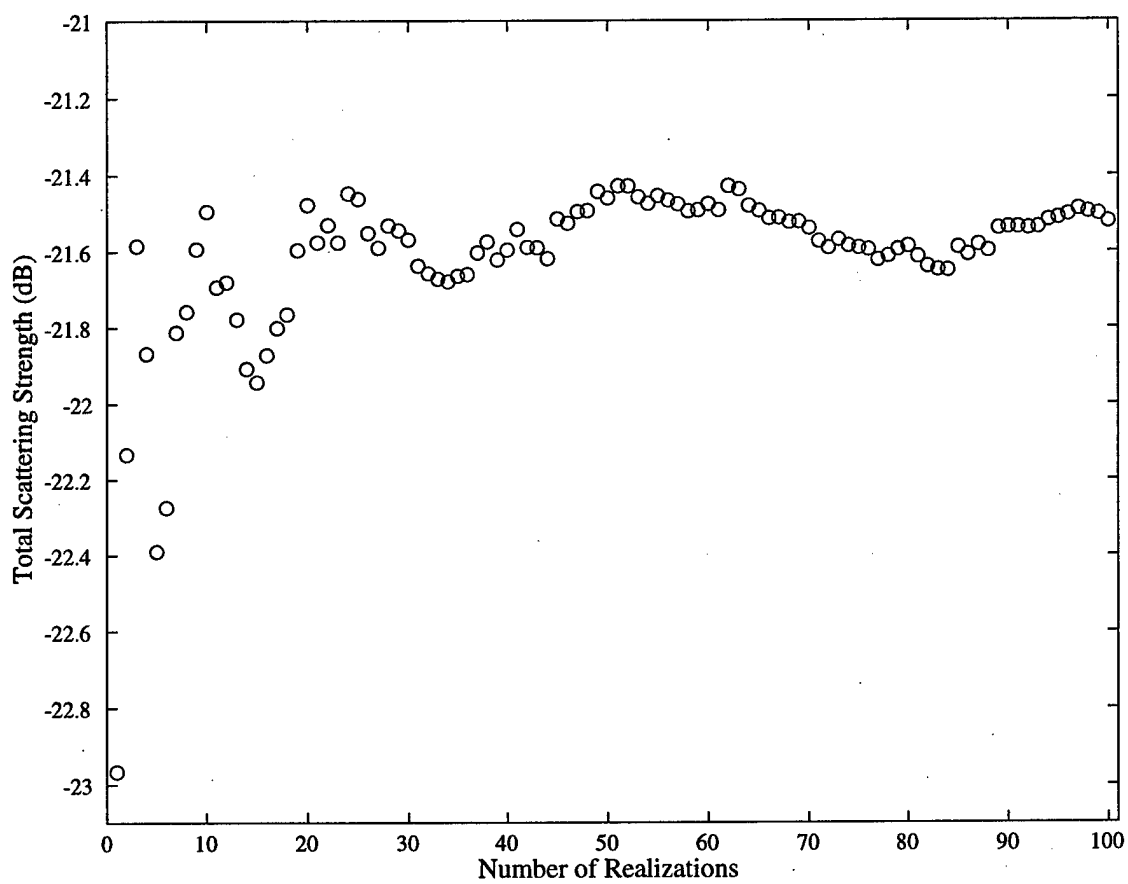


Figure 3.4: Monte-Carlo convergence with respect to the number of realizations ($N_x\lambda/L_x = 10$ and $L_x/\lambda = 6.4$).

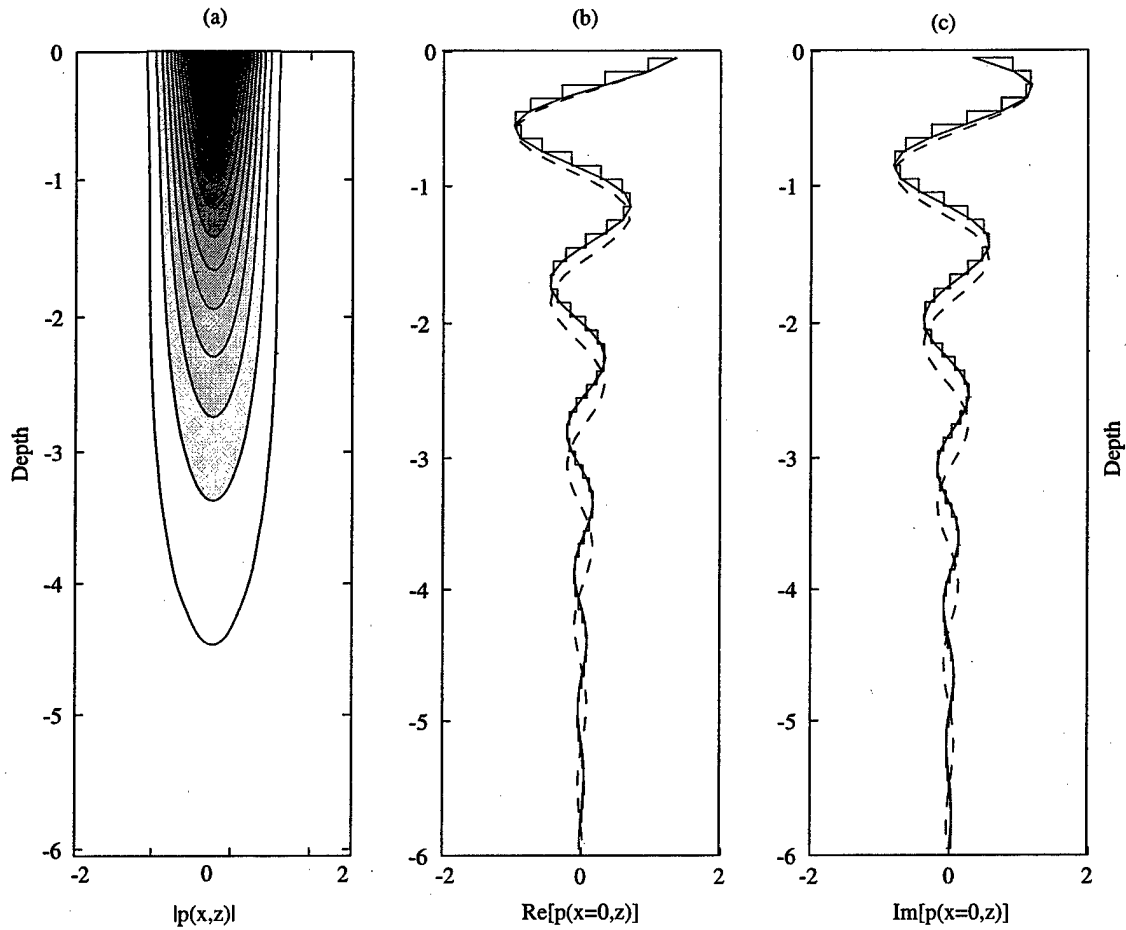


Figure 3.5: Fields within a half-space medium with a linear wavenumber profile ($\bar{c}/c_0 = 1.2$, $\bar{\rho}/\rho_0 = 2.0$, $a = -0.05$, $b = 0.1$) for a tapered incident field: (a) Contour plot of magnitude of the tapered field MoM solution; (b) Real component of the MoM solution (stepped curve) compared with the analytic solution (solid curve) and the incident field (dashed curve); (c) Imaginary components of the solutions.

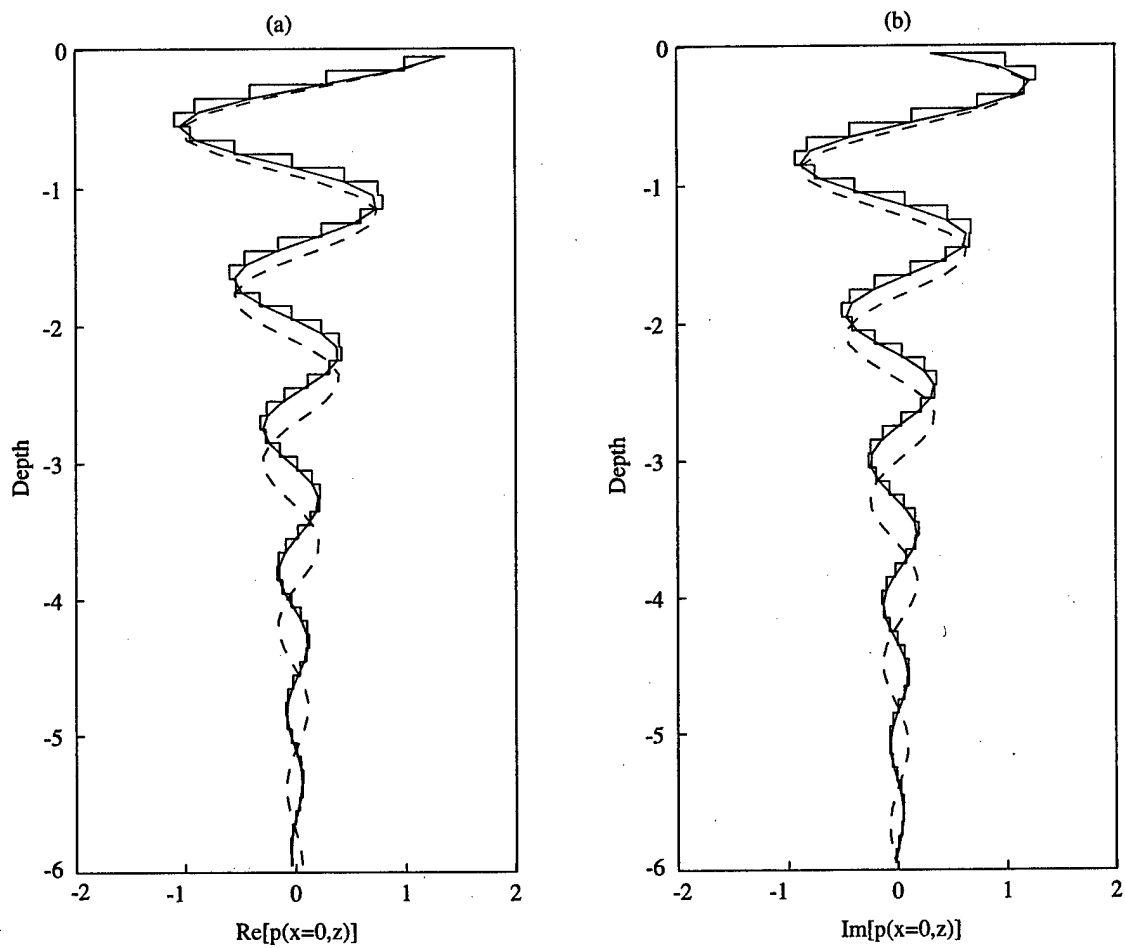


Figure 3.6: Fields within a half-space medium with a linear wavenumber profile ($\bar{c}/c_0 = 1.2$, $\bar{\rho}/\rho_0 = 2.0$, $a = -0.05$, $b = 0.1$) for a periodic medium and plane wave incident field: (a) Real components of the MoM solution (stepped curve) compared with the analytic solution (solid curve) and the incident field (dashed curve); (b) Imaginary components of the solutions.

the solid dots) is compared with the exact solution (plotted as the circles). Note that since the random medium is Gaussian the odd-order contributions to the scattering strength are zero. The perturbation series must be taken to fourth-order to model the scattering strength accurately. An ensemble of 200 realizations of the periodic random medium was used to find the scattering strength. If a problem lies outside the range of validity of the perturbation method altogether, the perturbation series may not converge towards the correct solution. Higher-order perturbation methods must be used with caution.

3.4 Summary and Conclusions

Two-dimensional acoustic volume scattering from a random medium can be simulated numerically using the Method of Moments. Compressional wave attenuation in the medium limits the size of the scattering volume. Therefore, the solution domain is limited in size, and numerical solutions can be performed without the use of excessive computational resources and time.

Two MoM solution methods are presented, in which the medium is modeled as both periodic and non-periodic. A tapered incident field is used with the non-periodic medium in order to limit the interaction of the incident field with the edges of the volume. A plane-wave incident field is used with the periodic medium. Periodicity is assumed only in the horizontal direction. In both cases, the vertical extent (depth) of the volume is defined by the distance the incident field penetrates into the lossy medium.

Point matching and pulse basis functions are demonstrated for use with both the periodic and non-periodic volumes. Full-domain Fourier basis and testing functions can be used with a periodic medium. In both cases, the scattering matrix is diagonally dominant and potentially sparse. Convergence and accuracy tests for Monte-Carlo simulations show that the medium should be minimally discretized at

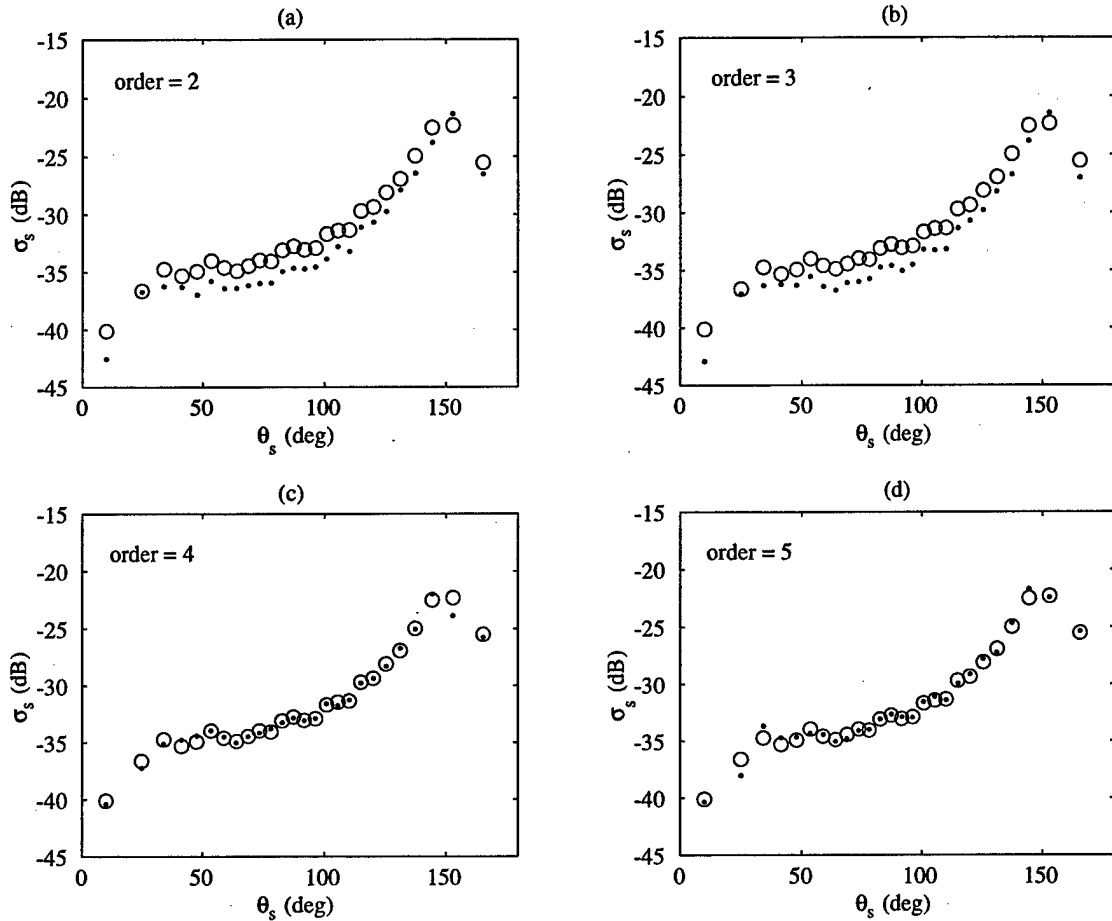


Figure 3.7: Comparisons of MoM solutions for the volume scattering strength found using the iterative SPM method and the exact matrix inversion method. The circles (o) are the exact solutions, and the solid dots (.) are the SPM solutions including terms up the specified order: (a) second-order SPM using (2.82); (b) third-order SPM using (2.84); (c) fourth-order SPM using (2.86); and (4) fifth-order SPM. The incident field is subcritical at $\theta_i = 10^\circ$, $l_c = 1.0\lambda$, $\sigma_p = 0.10$, $\mu = -2.0$, $\bar{\rho}/\rho_0 = 2.0$, $\bar{c}/c_0 = 1.1$, $\delta = 0.02$, with 10 points per wavelength.

10 points per wavelength in order to model scattering due to the medium fluctuations. The minimal size of the scattering volume required for convergence is smaller than expected. Monte-Carlo convergence was demonstrated for a horizontal dimension as small as $L_x/\lambda = 4$. Random realizations of the medium are generated by Fourier transforms assuming Gaussian statistics. The number of realizations required to estimate the ensemble average of the scattered field should be > 50 to assure statistical convergence.

Chapter 4

VALIDITY OF THE SMALL PERTURBATION METHOD

Insight into determining whether single or multiple scattering is significant in a continuous random medium can be gained by examining the scales and interrelations of various parameters of the problem. The most essential of these parameters are the wavelength of the incident field, the variance of the fluctuations in the medium, the correlation length of the fluctuations, and the characteristic length scale over which scattering occurs in the volume (due to attenuation in the medium).

In general, it is desirable to have analytic relations and criteria for predicting the occurrence of multiple scattering. For the general acoustic fluid half-space problem, however, this is difficult and not at present available. Criteria would have to properly account for the interface and reflection back into the medium of the scattered field. The effects of correlation of the medium compressibility and density fluctuations must also be considered. An alternative analysis can be made using numerical simulations. By comparing solutions of a weak scattering method, such as perturbation theory, with exact numerical methods that do not make weak scattering assumptions, the range of validity of the perturbation method can be inferred.

In this chapter, both multiple scattering theory and numerical methods (as in Chapter 3.1) will be used to investigate the applicability of perturbation methods for volume scattering from a fluid sediment half-space. Parameters of the random media are limited to those of marine sand and soft-mud sediments modeled as fluids. The physical parameters of the sediment (e.g., mean density, sound speed, and statistical properties of the medium) are selected from current publications of studies made of sediment core samples and in situ measurements [60, 23, 13].

4.1 Multiple Scattering Theory

Classical multiple scattering theory involves using diagram techniques to sum the perturbative series for the mean field (Dyson's equations) and the intensity or covariance of the field (Bethe-Salpeter equation) in the scattering medium. The Bethe-Salpeter equation is directly related to the radiative transfer equation where attenuation in the medium is a function of the intrinsic absorption of the medium and the scattering attenuation [80]. Scattering attenuation is due to incident energy diverted from the incident direction by multiple scattering.

Radiative transfer theory provides an analytic method of solving for the effects of multiple scattering on the field intensity, where, in general, there is no solution to the Bethe-Salpeter equation. Radiative transfer, on the other hand, is a phenomenological approach that does not provide insight into the scattering processes and the parametric relationships of the medium and the incident wave that dictate the occurrence of multiple scattering. To gain physical insight into multiple scattering it is more useful to study Dyson's equation. To proceed analytically, assumptions are typically made, the most basic of which is the *bilocal* approximation.

A great deal of literature is available on multiple scattering theory. The bulk of this work focuses on scattering due to the index of refraction (created by permittivity fluctuations) in an unbounded medium. The sediment problem differs in that the medium is a lossy half-space. This constrains the incident and scattered fields to a region near the interface. The sediment problem also differs in that density fluctuations, as well as compressibility fluctuations, must be considered. In general, bistatic scattering into the UHS is of greater interest than forward scattering into the LHS. Therefore, the correlation properties of the density and compressibility may have a significant role in suppressing or enhancing multiple scattering effects.

Effective medium parameters for an unbounded, statistically homogeneous fluid with strong density and compressibility fluctuations have been discussed by Zhuck

[89, 90] in the low-frequency limit ($k \rightarrow 0$). This work extends the weak scattering criterion developed in previous multiple scattering theories, which states

$$|k_0 l_\kappa \sigma_\kappa|^2 \ll 1, \quad (4.1)$$

to include density fluctuations that obey the same relation,

$$|k_0 l_\rho \sigma_\rho|^2 \ll 1. \quad (4.2)$$

The length scales l_κ and l_ρ are the correlation lengths of the compressibility and density fluctuations, respectively. The cross-correlation of density and compressibility fluctuations is not considered. In addition, larger correlation scales (comparable to the acoustic wavelength) and loss due to intrinsic attenuation are not considered.

The role of half-space effects in multiple scattering has been investigated using Dyson's equation to find a renormalized effective wavenumber of the mean field [43, 63]. The principal conclusion was that the mean field in the bounded medium cannot be modeled by defining a single effective wavenumber, as with the unbounded medium. Instead, a transition layer near the boundary must be defined in which the incoherent wave reflected from the interface affects the coherent wave to the same order as an incoherent wave generated without the interface.

In this section, the bilocal approximation will be applied to the acoustic scattering case where compressibility and density fluctuations are present and of comparable magnitude. The general acoustic scattering problem, including half-space effects, will not be considered. Compressional wave attenuation will be included as well as the effects of density and compressibility correlation. This differs from developments in the literature where only compressibility (or permittivity) fluctuations are considered. In general, the problem of scattering due to density (or permeability) fluctuations has not been widely studied. In electromagnetics, strong permeability fluctuations are rarely encountered. In ocean acoustics, multiple scattering is usually only considered in the forward direction where sound speed fluctuations are the dominant scattering mechanism and density fluctuations need not be considered.

4.1.1 Dyson's Equation

Consider the small perturbation solution for the acoustic field from Section 2.3 rewritten as

$$p(\mathbf{r}) = g(\mathbf{r}, \mathbf{r}_0) = g_0(\mathbf{r}, \mathbf{r}_0) + \sum_{n=1}^{\infty} g_n(\mathbf{r}, \mathbf{r}_0), \quad (4.3)$$

where g is the field at \mathbf{r} due to a source at \mathbf{r}_0 , and

$$g_{n+1}(\mathbf{r}, \mathbf{r}_0) = \int_V [\bar{k}^2 \gamma_{\kappa}(\mathbf{r}', t) g_0(\mathbf{r}, \mathbf{r}') g_n(\mathbf{r}', \mathbf{r}_0) + \gamma_{\rho}(\mathbf{r}') \nabla' g_0(\mathbf{r}, \mathbf{r}') \cdot \nabla' g_n(\mathbf{r}', \mathbf{r}_0)] d\mathbf{r}'. \quad (4.4)$$

Assume (for convenience only, since measurements neither support nor challenge this assumption) that the fluctuations in the medium are zero-mean Gaussian random variables such that the even moments are given by

$$\begin{aligned} \langle \gamma_{\kappa}(\mathbf{r}_1) \cdots \gamma_{\kappa}(\mathbf{r}_{2n}) \rangle &= \sum_{\text{pairs}} C_{\kappa\kappa}(\mathbf{r}_i, \mathbf{r}_j) \cdots C_{\kappa\kappa}(\mathbf{r}_k, \mathbf{r}_l), \\ \langle \gamma_{\kappa}(\mathbf{r}_1) \cdots \gamma_{\rho}(\mathbf{r}_{2n}) \rangle &= \sum_{\text{pairs}} C_{\kappa\rho}(\mathbf{r}_i, \mathbf{r}_j) \cdots C_{\kappa\rho}(\mathbf{r}_k, \mathbf{r}_l), \\ \langle \gamma_{\rho}(\mathbf{r}_1) \cdots \gamma_{\rho}(\mathbf{r}_{2n}) \rangle &= \sum_{\text{pairs}} C_{\rho\rho}(\mathbf{r}_i, \mathbf{r}_j) \cdots C_{\rho\rho}(\mathbf{r}_k, \mathbf{r}_l), \end{aligned} \quad (4.5)$$

and the odd moments are zero. For example,

$$\begin{aligned} \langle \gamma_{\kappa}(\mathbf{r}_1) \gamma_{\rho}(\mathbf{r}_2) \gamma_{\kappa}(\mathbf{r}_3) \gamma_{\rho}(\mathbf{r}_4) \rangle &= C_{\kappa\rho}(\mathbf{r}_1, \mathbf{r}_2) C_{\kappa\rho}(\mathbf{r}_3, \mathbf{r}_4) + C_{\kappa\kappa}(\mathbf{r}_1, \mathbf{r}_3) C_{\rho\rho}(\mathbf{r}_2, \mathbf{r}_4) \\ &\quad + C_{\kappa\rho}(\mathbf{r}_1, \mathbf{r}_4) C_{\rho\kappa}(\mathbf{r}_2, \mathbf{r}_3). \end{aligned} \quad (4.6)$$

The renormalized perturbation series for the *mean* field (\bar{g}) is formed by performing an ensemble average over realizations of the medium:

$$\begin{aligned} \bar{g}(\mathbf{r}, \mathbf{r}_0) &= \langle g(\mathbf{r}, \mathbf{r}_0) \rangle \\ &= g_0(\mathbf{r}, \mathbf{r}_0) + \sum_{n=1}^{\infty} \langle g_n(\mathbf{r}, \mathbf{r}_0) \rangle \\ &= g_0(\mathbf{r}, \mathbf{r}_0) + \langle g_2(\mathbf{r}, \mathbf{r}_0) \rangle + \langle g_4(\mathbf{r}, \mathbf{r}_0) \rangle + \cdots \end{aligned} \quad (4.7)$$

Odd-order terms are zero due to the Gaussian assumption.

Solving this system of equations by successive iterations, Dyson's equation for a random medium with both density and compressibility fluctuations is found to be

$$\begin{aligned}
 \bar{g}(\mathbf{r}, \mathbf{r}_0) = & g_0(\mathbf{r}, \mathbf{r}_0) + \bar{k}^4 \iint g_0(\mathbf{r}, \mathbf{r}_1) m_{\kappa\kappa}(\mathbf{r}_1, \mathbf{r}_2) \bar{g}(\mathbf{r}_2, \mathbf{r}_0) d\mathbf{r}_1 d\mathbf{r}_2 \\
 & + \bar{k}^2 \iint g_0(\mathbf{r}, \mathbf{r}_1) m_{\kappa\rho}(\mathbf{r}_1, \mathbf{r}_2) \cdot \nabla_2 \bar{g}(\mathbf{r}_2, \mathbf{r}_0) d\mathbf{r}_1 d\mathbf{r}_2 \\
 & + \bar{k}^2 \iint \nabla_1 g_0(\mathbf{r}, \mathbf{r}_1) \cdot m_{\rho\kappa}(\mathbf{r}_1, \mathbf{r}_2) \bar{g}(\mathbf{r}_2, \mathbf{r}_0) d\mathbf{r}_1 d\mathbf{r}_2 \\
 & + \iint \nabla_1 g_0(\mathbf{r}, \mathbf{r}_1) \cdot m_{\rho\rho}(\mathbf{r}_1, \mathbf{r}_2) \cdot \nabla_2 \bar{g}(\mathbf{r}_2, \mathbf{r}_0) d\mathbf{r}_1 d\mathbf{r}_2 .
 \end{aligned} \tag{4.8}$$

The operator ∇_1 is the gradient with respect to \mathbf{r}_1 ; ∇_2 is the gradient with respect to \mathbf{r}_2 ; and $\nabla_2 \nabla_1$ is a dyad operator. This form of Dyson's equation is similar to the standard Dyson's equation found in [75, 68], except the *mass operator* $m(\mathbf{r}_1, \mathbf{r}_2)$ now has four components that represent the interactions of scattering from density and compressibility fluctuations. Also, note that the integration limits in (4.8) are over the half-space volume. For now, the effects of the interface will be ignored and the limits of integration will be extended over infinity. Consequently, the unperturbed free-space Green's function can be used for g_0 instead of (2.33).

The mass operators are best described using the diagram method introduced in Section 2.3.2 with the addition of several new symbols. Represent the correlations between density and compressibility fluctuation with a dashed line:

$$\begin{aligned}
 \bar{k}^4 C_{\kappa\kappa}(\mathbf{r}_i, \mathbf{r}_j) & \sim \begin{array}{c} \bullet \text{---} \text{---} \bullet \\ \mathbf{r}_i \quad \mathbf{r}_j \end{array} , \\
 \bar{k}^2 C_{\kappa\rho}(\mathbf{r}_i, \mathbf{r}_j) & \sim \begin{array}{c} \bullet \text{---} \text{---} \circ \\ \mathbf{r}_i \quad \mathbf{r}_j \end{array} , \\
 \bar{k}^2 C_{\rho\kappa}(\mathbf{r}_i, \mathbf{r}_j) & \sim \begin{array}{c} \circ \text{---} \text{---} \bullet \\ \mathbf{r}_i \quad \mathbf{r}_j \end{array} , \\
 C_{\rho\rho}(\mathbf{r}_i, \mathbf{r}_j) & \sim \begin{array}{c} \circ \text{---} \text{---} \circ \\ \mathbf{r}_i \quad \mathbf{r}_j \end{array} .
 \end{aligned} \tag{4.9}$$

Represent the mean Green's function for the inhomogeneous medium with a double

line:

$$\bar{g}(\mathbf{r}, \mathbf{r}_0) \sim \frac{\text{---}}{\mathbf{r} \quad \mathbf{r}_0} . \tag{4.10}$$

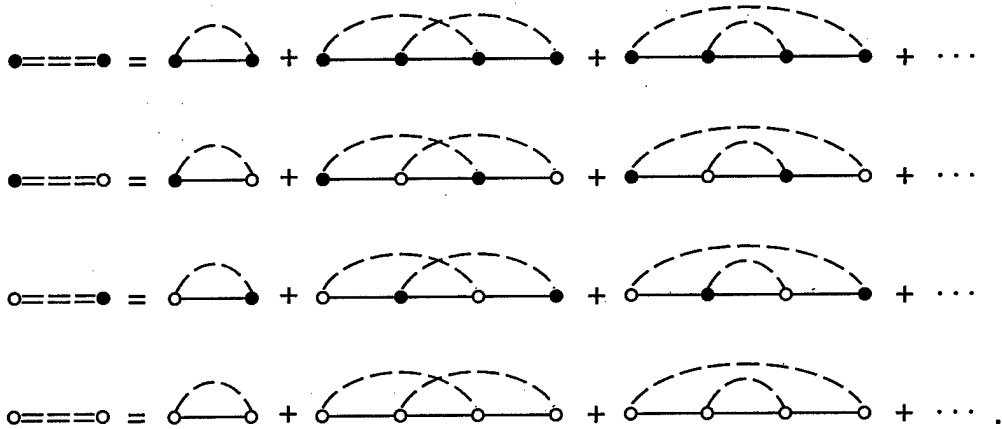
The mass operators are represented as double dashed line segments:

$$\begin{aligned} m_{\kappa\kappa}(\mathbf{r}_1, \mathbf{r}_2) &\sim \bullet \text{---} \text{---} \bullet , \\ m_{\kappa\rho}(\mathbf{r}_1, \mathbf{r}_2) &\sim \bullet \text{---} \text{---} \circ , \\ m_{\rho\kappa}(\mathbf{r}_1, \mathbf{r}_2) &\sim \circ \text{---} \text{---} \bullet , \\ m_{\rho\rho}(\mathbf{r}_1, \mathbf{r}_2) &\sim \circ \text{---} \text{---} \circ . \end{aligned} \tag{4.11}$$

Following the procedure of separating weak and strong scattering interactions [68], Dyson's equation for an acoustic fluid can then be written in diagram representation as

$$\begin{aligned} \text{---} &= \text{---} + \text{---} \bullet \text{---} \bullet \text{---} + \text{---} \bullet \text{---} \circ \text{---} \\ &+ \text{---} \circ \text{---} \bullet \text{---} + \text{---} \circ \text{---} \circ \text{---} , \end{aligned} \tag{4.12}$$

where the mass operators are defined as follows:



Consider a statistically homogeneous medium where the correlation functions, the Green's functions, and the mass operators are all functions of difference coordi-

nates only. Dyson's equation is then rewritten as a double convolution integral:

$$\begin{aligned}
\bar{g}(\mathbf{r} - \mathbf{r}_0) = & g_0(\mathbf{r} - \mathbf{r}_0) + \bar{k}^4 \iint g_0(\mathbf{r} - \mathbf{r}_1) m_{\kappa\kappa}(\mathbf{r}_1 - \mathbf{r}_2) \bar{g}(\mathbf{r}_2 - \mathbf{r}_0) d\mathbf{r}_1 d\mathbf{r}_2 \\
& + \bar{k}^2 \iint g_0(\mathbf{r} - \mathbf{r}_1) m_{\kappa\rho}(\mathbf{r}_1 - \mathbf{r}_2) \cdot \nabla_2 \bar{g}(\mathbf{r}_2 - \mathbf{r}_0) d\mathbf{r}_1 d\mathbf{r}_2 \\
& + \bar{k}^2 \iint \nabla_1 g_0(\mathbf{r} - \mathbf{r}_1) \cdot m_{\rho\kappa}(\mathbf{r}_1 - \mathbf{r}_2) \bar{g}(\mathbf{r}_2 - \mathbf{r}_0) d\mathbf{r}_1 d\mathbf{r}_2 \\
& + \iint \nabla_1 g_0(\mathbf{r} - \mathbf{r}_1) \cdot m_{\rho\rho}(\mathbf{r}_1 - \mathbf{r}_2) \cdot \nabla_2 \bar{g}(\mathbf{r}_2 - \mathbf{r}_0) d\mathbf{r}_1 d\mathbf{r}_2 .
\end{aligned} \tag{4.13}$$

The unperturbed free-space Green's function in three dimensions is

$$g_0(\mathbf{r}) = \frac{e^{i\bar{k}r}}{4\pi r} . \tag{4.14}$$

Solving for the mean Green's function using Fourier transforms with the transform of the unperturbed Green's functions,

$$G_0(\mathbf{k}) = \frac{1}{8\pi^3(k^2 - \bar{k}^2)} , \tag{4.15}$$

and the transform of the mass operators,

$$M_{\alpha\beta}(\mathbf{k}) = \int m(\mathbf{r}_1 - \mathbf{r}_2)_{\alpha\beta} e^{-i\mathbf{k}\cdot\mathbf{r}} d\mathbf{r} , \tag{4.16}$$

an expression for \bar{g} can be found explicitly as

$$\bar{g}(\mathbf{r} - \mathbf{r}_0) = \frac{1}{8\pi^3} \int \frac{e^{i\mathbf{k}\cdot(\mathbf{r}-\mathbf{r}_0)}}{k^2 - \bar{k}^2 - M(\mathbf{k})} d\mathbf{k} . \tag{4.17}$$

The function M is found in terms of the Fourier transforms of each component,

$$M(\mathbf{k}) = \bar{k}^4 M_{\kappa\kappa}(\mathbf{k}) - 2i\bar{k}^2 \mathbf{k} \cdot \mathbf{M}_{\kappa\rho}(\mathbf{k}) - \mathbf{k} \cdot \mathbb{M}_{\rho\rho}(\mathbf{k}) \cdot \mathbf{k} , \tag{4.18}$$

with $\mathbf{M}_{\kappa\rho} = \mathbf{M}_{\rho\kappa}$. The function $M_{\kappa\kappa}$ is a scalar, $\mathbf{M}_{\kappa\rho}$ is a vector pointing in the \hat{k} direction, and $\mathbb{M}_{\rho\rho}$ is a dyad whose orientation is defined by $\hat{k}\hat{k}$.

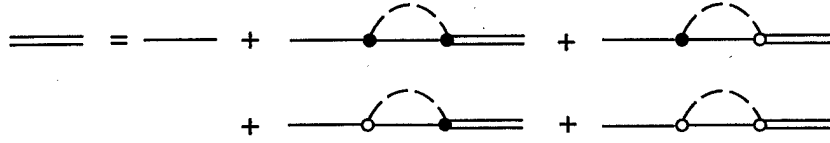
Equation (4.17) is the mean Green's function for the coherent field. In this form, (4.17) is *exact*. The expression for the mass operator, however, is an infinite expansion and is generally not obtainable in closed form. Dyson's equation is therefore only useful in that it allows approximations to be made of the mass operator that lead to insight into the behavior of \bar{g} .

4.1.2 Bilocal Approximation

The simplest approximation to Dyson's equation is the *bilocal* approximation which involves keeping only the first terms in the mass operators [10], such that

$$\begin{aligned}
 m_{\kappa\kappa}(\mathbf{r}_1, \mathbf{r}_2) &\approx \bar{k}^4 C_{\kappa\kappa}(\mathbf{r}_1, \mathbf{r}_2) g_0(\mathbf{r}_1, \mathbf{r}_2) , \\
 m_{\kappa\rho}(\mathbf{r}_1, \mathbf{r}_2) &\approx \bar{k}^2 C_{\kappa\rho}(\mathbf{r}_1, \mathbf{r}_2) \nabla_2 g_0(\mathbf{r}_1, \mathbf{r}_2) , \\
 m_{\rho\kappa}(\mathbf{r}_1, \mathbf{r}_2) &\approx \bar{k}^2 C_{\rho\kappa}(\mathbf{r}_1, \mathbf{r}_2) \nabla_1 g_0(\mathbf{r}_1, \mathbf{r}_2) , \\
 m_{\rho\rho}(\mathbf{r}_1, \mathbf{r}_2) &\approx C_{\rho\rho}(\mathbf{r}_1, \mathbf{r}_2) \nabla_1 \nabla_2 g_0(\mathbf{r}_1, \mathbf{r}_2) .
 \end{aligned} \tag{4.19}$$

The bilocal approximation is represented in diagram notation as



Applying this approximation to (4.8), the mean field is

$$\begin{aligned}
 \bar{g}(\mathbf{r}, \mathbf{r}_0) &= g_0(\mathbf{r}, \mathbf{r}_0) + \bar{k}^4 \iint C_{\kappa\kappa}(\mathbf{r}_1, \mathbf{r}_2) g_0(\mathbf{r}, \mathbf{r}_1) g_0(\mathbf{r}_1, \mathbf{r}_2) \bar{g}(\mathbf{r}_2, \mathbf{r}_0) d\mathbf{r}_1 d\mathbf{r}_2 \\
 &+ \bar{k}^2 \iint C_{\kappa\rho}(\mathbf{r}_1, \mathbf{r}_2) g_0(\mathbf{r}, \mathbf{r}_1) \nabla_2 g_0(\mathbf{r}_1, \mathbf{r}_2) \cdot \nabla_2 \bar{g}(\mathbf{r}_2, \mathbf{r}_0) d\mathbf{r}_1 d\mathbf{r}_2 \\
 &+ \bar{k}^2 \iint C_{\rho\kappa}(\mathbf{r}_1, \mathbf{r}_2) \nabla_1 g_0(\mathbf{r}, \mathbf{r}_1) \cdot \nabla_1 g_0(\mathbf{r}_1, \mathbf{r}_2) \bar{g}(\mathbf{r}_2, \mathbf{r}_0) d\mathbf{r}_1 d\mathbf{r}_2 \\
 &+ \iint C_{\rho\rho}(\mathbf{r}_1, \mathbf{r}_2) \nabla_1 g_0(\mathbf{r}, \mathbf{r}_1) \cdot \nabla_1 \nabla_2 g_0(\mathbf{r}_1, \mathbf{r}_2) \cdot \nabla_2 \bar{g}(\mathbf{r}_2, \mathbf{r}_0) d\mathbf{r}_1 d\mathbf{r}_2 .
 \end{aligned} \tag{4.20}$$

Again, consider a statistically homogeneous medium where the density and compressibility fluctuations are proportional using (2.13) and (2.14). Using the bilocal approximation, the individual mass operators that comprise (4.18) can be written as

$$\begin{aligned}
 M_{\kappa\kappa}(\mathbf{k}) &\approx \mu^2 \int C_{\rho\rho}(\mathbf{r}) g_0(\mathbf{r}) e^{-i\mathbf{k}\cdot\mathbf{r}} d\mathbf{r} , \\
 M_{\kappa\rho}(\mathbf{k}) &\approx \mu \int C_{\rho\rho}(\mathbf{r}) \nabla g_0(\mathbf{r}) e^{-i\mathbf{k}\cdot\mathbf{r}} d\mathbf{r} , \\
 M_{\rho\rho}(\mathbf{k}) &\approx \int C_{\rho\rho}(\mathbf{r}) \nabla \nabla g_0(\mathbf{r}) e^{-i\mathbf{k}\cdot\mathbf{r}} d\mathbf{r} .
 \end{aligned} \tag{4.21}$$

Using the free space Green's function in three dimensions with an isotropic and exponential correlation function,

$$C_{\rho\rho}(\mathbf{r}) = \sigma_\rho^2 e^{-|\mathbf{r}|/l_c}, \quad (4.22)$$

each term in the mass operator can be derived analytically as

$$M_{\kappa\kappa}(\mathbf{k}) = \mu^2 \frac{\sigma_\rho^2 l_c^2}{a^2 - b^2}, \quad (4.23)$$

$$\mathbf{k} \cdot \mathbf{M}_{\kappa\rho}(\mathbf{k}) = \mu \frac{\sigma_\rho^2 k l_c}{2b^2} \left[i\bar{k}l_c \left(c - \frac{2ab}{a^2 - b^2} \right) - (2b - ac) \right], \quad (4.24)$$

and

$$\begin{aligned} \mathbf{k} \cdot \mathbf{M}_{\rho\rho}(\mathbf{k}) \cdot \mathbf{k} = \frac{\sigma_\rho^2 k^2}{2b^3} & \left[i\bar{k}l_c \left[(2b - ac) - (a - b^2) \left(c - \frac{2ab}{a^2 - b^2} \right) \right] \right. \\ & \left. + (2b - ac)(a - b^2) \right], \end{aligned} \quad (4.25)$$

where

$$\begin{aligned} a &= 1 - i\bar{k}l_c, \\ b &= ikl_c, \\ c &= \ln[(a + b)/(a - b)]. \end{aligned} \quad (4.26)$$

Since equations (4.23), (4.24), and (4.25) are not found in previous literature, the details of performing the integrations are outlined in Appendix F.

For an isotropic medium, (4.17) can be rewritten in spherical coordinates with vector \mathbf{k} pointing in the z -direction. Performing the integration over the angle variables, a single integral results:

$$\bar{g}(R) = \frac{1}{4\pi^2 i R} \int_{-\infty}^{\infty} \frac{e^{ikR}}{k^2 - \bar{k}^2 - M(k)} k dk, \quad (4.27)$$

with $R = |r - r_0|$. Taking residues of the integrand with respect to k at the dominant pole, the mean Green's function for the medium can be found approximately as

$$\bar{g}(R) \approx \frac{e^{ik_e R}}{4\pi R}. \quad (4.28)$$

It is expected that a single pole ($k_e \approx \bar{k}$) in the upper half of the complex k plane will dominate the total solution of (4.27). The other wave solutions - corresponding to the other poles - are expected to decay rapidly and can be ignored. This has been shown for the case of index of refraction fluctuation only [68], and is assumed to be true for the current case if the medium fluctuations are not too strong and $|M(k)| \ll \bar{k}$.

The wavenumber k_e is the *effective wavenumber* of the renormalized medium. The real component of k_e yields the effective phase speed of the medium. As the mean path of the wave through the medium is increased by multiple scattering, the real part of k_e increases, thus causing an effective decrease in the phase speed. The imaginary part of k_e corresponds to the total coherent field attenuation in the effective medium. Multiple scatter will act to increase the total attenuation due to scattering loss out of the incident direction.

The onset of multiple scattering can be examined by studying the behavior of the dominant pole k_e as the parameters of the medium are varied. The poles of (4.27) are the roots of the denominator of the integrand:

$$k^2 - \bar{k}^2 - M(k) = 0. \quad (4.29)$$

In the weak scattering limit, the position of k_e should approach that of \bar{k} in the complex plane. Therefore, rather than solving for the root exactly, using (4.23), (4.24) and (4.25), the position of the dominant pole k_e can be found approximately by taking σ_p^2 to be small and using perturbation analysis. In the zeroth-order solution for the pole, where there is no multiple scattering, $M(k) = 0$ and $k_e = \bar{k}$. The first-order solution is then found by substituting the zeroth-order result into (4.29), such

that

$$k_e^2 - \bar{k}^2 - M(\bar{k}) \approx 0. \quad (4.30)$$

With $M(\bar{k})$ small, the effective wavenumber for the the bilocal approximation is

$$k_e \approx \bar{k} + \frac{M(\bar{k})}{2\bar{k}}. \quad (4.31)$$

Multiple scattering can be examined by plotting the changes in the real and imaginary components of k_e , defined respectively as

$$\gamma_e' = \frac{\text{Re}[k_e - \bar{k}]}{\text{Re}[\bar{k}]} \quad (4.32)$$

and

$$\gamma_e'' = \frac{\text{Im}[k_e - \bar{k}]}{\text{Im}[\bar{k}]} \quad (4.33)$$

Figures 4.1 and 4.2 show contours of γ_e' and γ_e'' as functions of l_c and μ for several values of the attenuation coefficient α_λ . All plots are made with $\sigma_\rho^2 = 0.01$. The dashed contours in Figure 4.2 are values of γ_e'' found by solving for the roots of (4.29) numerically using a complex simplex method. The solid contours are values of γ_e'' found using k_e estimated with (4.31). The perturbation method for finding the effective wavenumber shows reasonable correspondence with the numerical method for small l_c/λ and μ near -1 . When using the perturbation method, γ_e' and γ_e'' are (to first order) proportional to the variance of the medium. Therefore, it is only necessary to plot contours for a single value of σ_ρ^2 . Contours for other values of σ_ρ^2 will scale proportionally.

The range of parameters shown in Figures 4.1 and 4.2 reflects typical values observed in marine sediment over a variety of environments and sediment types. The plot for $\alpha_\lambda = 0.1$ (which corresponds to typical mud and silt sediment) shows higher scattering attenuation of the mean field. As the intrinsic attenuation in the

medium ($\text{Im}[\bar{k}]$) increases, multiple scattering decreases and the scattering attenuation ($\text{Im}[k_e - \bar{k}]$) decreases. A value of $\alpha_\lambda = 1.0$ corresponds to a typical sand sediment.

Relative to the homogeneous wavenumber, changes in the real part of the effective wavenumber are small as expected ($\gamma'_e \ll \gamma''_e$). Changes in the imaginary part of the effective wavenumber are a minimum for values of $\mu \approx -1$. This can be attributed to the minimum in the sound speed fluctuations when density and compressibility fluctuations are negatively correlated.

4.1.3 First-order Multiple Scattering

For weak scattering - but not necessarily single scattering - the imaginary component of k_e that is due to scattering attenuation should approach the total scattering cross-section derived from the first-order perturbation approximation. The effective wavenumber found using (4.31) can then be compared to the first-order perturbation result of Section 2.2. In other words, the power attenuation of the mean field should obey the relation

$$2\text{Im}[k_e - \bar{k}] = \sigma_{iv} = \int_{4\pi} \sigma_v d\omega, \quad (4.34)$$

where σ_v is the differential volume scattering cross-section and $d\omega = \sin\theta d\theta d\phi$. This approach is often referred to as first-order multiple scattering [30].

From Section 2.3, using (2.90) and neglecting half-space effects, the first-order differential cross-section is

$$\sigma_v = \frac{\pi}{2} |\bar{k}|^4 (\mu + \cos\theta)^2 S_{\rho\rho}(k_d), \quad (4.35)$$

where θ is the angle between the incidence and scattering directions, and $k_d = 2\text{Re}[\bar{k}] \sin(\theta/2)$ is the Bragg wavenumber. Using the correlation function (4.22), the

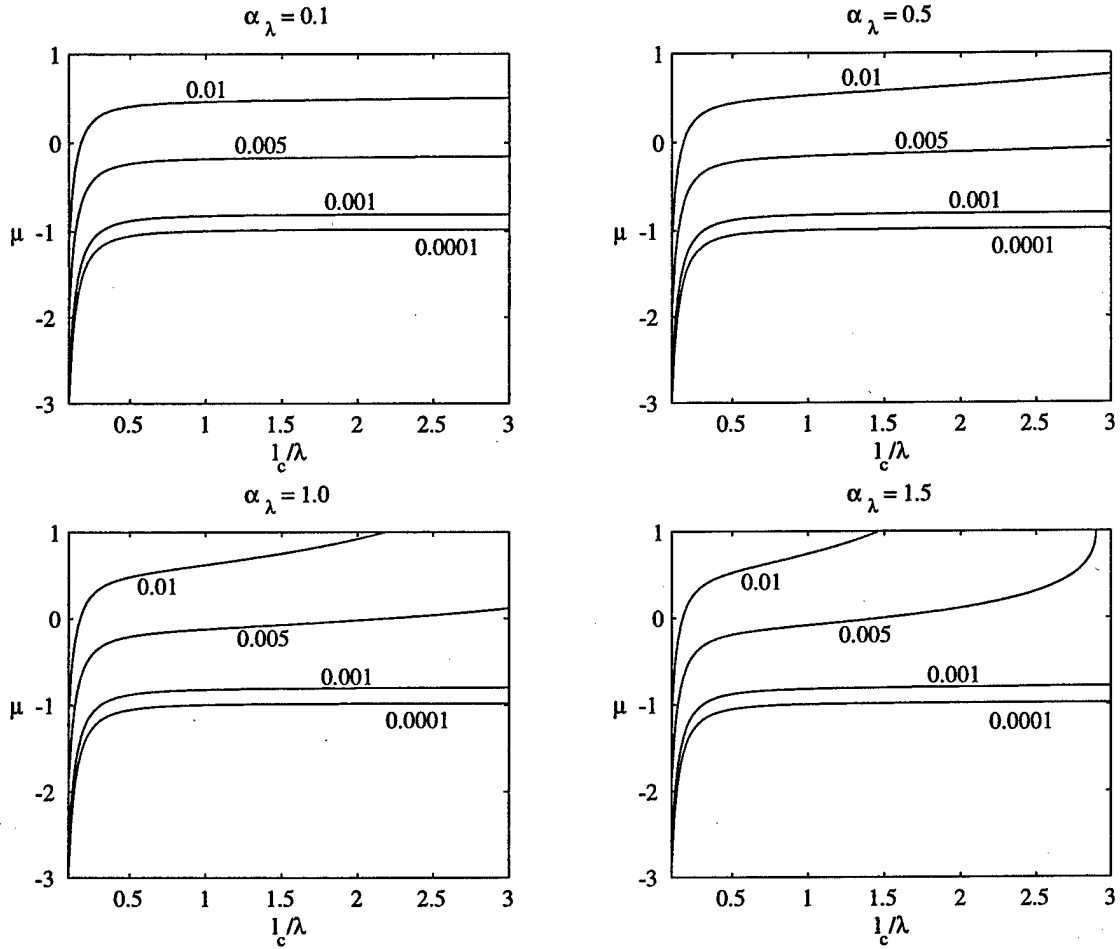


Figure 4.1: Contours of γ'_e as a function of l_c/λ , μ , and α_λ . All contours are calculated with $\sigma_\rho^2 = 0.01$ using (4.31).

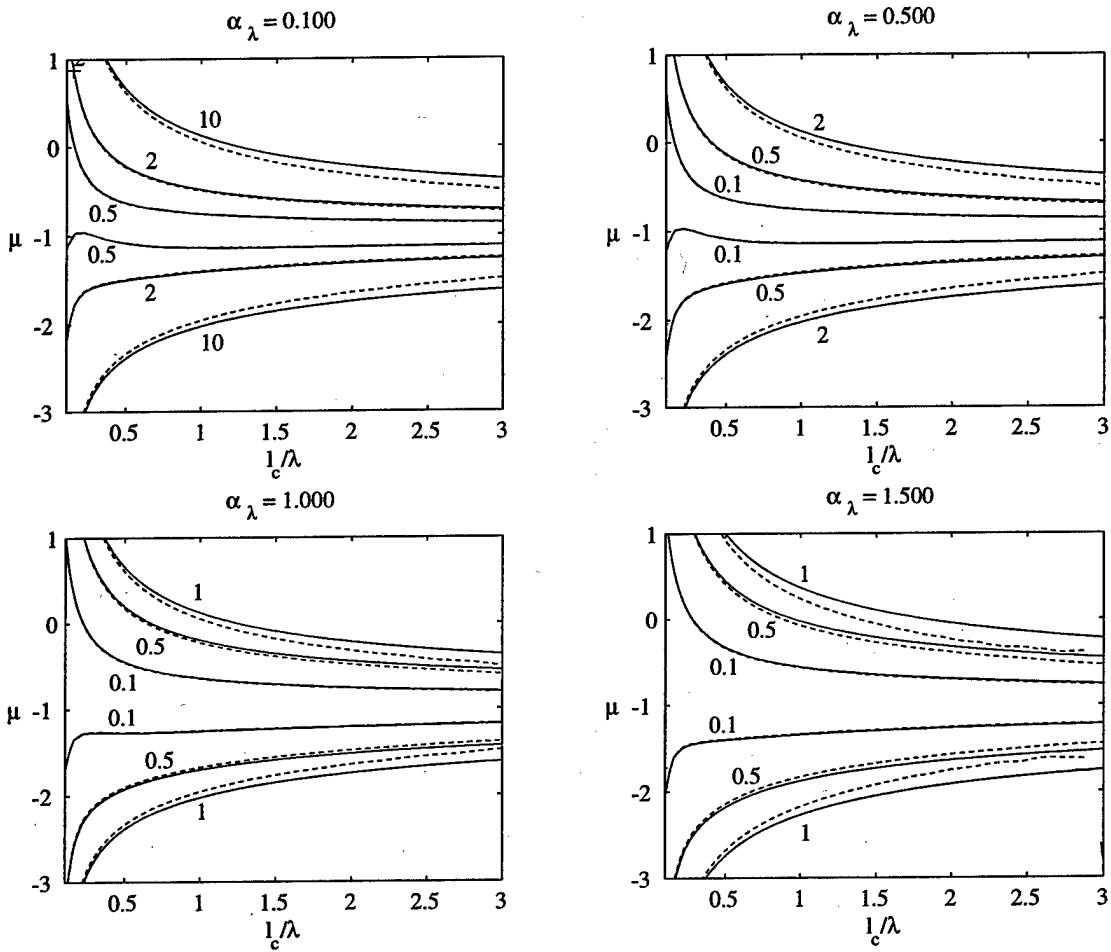


Figure 4.2: Contours of γ_e'' as a function of l_c/λ , μ , and α_λ . Solid contours are found using a perturbation method, and the dashed contours are found numerically. All contours are calculated with $\sigma_\rho^2 = 0.01$.

total volume scattering cross-section is

$$\sigma_{tv} = \sigma_{\rho}^2 l_c^3 |\bar{k}|^4 \left[\frac{2\mu^2}{a^2 - b^2} + \frac{2\mu}{b^2} \left(c - \frac{2ab}{a^2 - b^2} \right) + \frac{1}{b^3} \left(2b - 2ac + \frac{2a^2b}{a^2 - b^2} \right) \right], \quad (4.36)$$

where now a , b , and c are redefined as

$$\begin{aligned} a &= 1 + 2(\text{Re}[\bar{k}]l_c)^2, \\ b &= -2(\text{Re}[\bar{k}]l_c)^2, \\ c &= \ln \left(\frac{a+b}{a-b} \right). \end{aligned} \quad (4.37)$$

Figure 4.3 shows contour plots of the ratio γ_e'' using k_e found from (4.36) and (4.34) for various sediment types (solid contours). Also plotted in Figures 4.3 (as the nearly hidden dashed contours) is γ_e'' found using (4.31). A small difference in the two methods of calculating k_e can be seen at $l_c/\lambda \ll 1$ near $\mu = -1$.

4.2 A Comparison with Numerical Methods

Multiple scattering theory provides an analytic method of studying higher-order scattering in an unbounded medium. For a random half-space, however, analytic results are not easily obtained. The half-space geometry prohibits a solution by Fourier transforms because the medium and the Green's function are no longer translationally invariant in the z -direction. The integration over the medium is no longer an integration over an infinite continuum, but rather over the half-space. Analytical results cannot be found unless further approximations are made.

Numerical methods will be employed to analyze half-space effects and their effect on multiple scattering. Two potential effects will be investigated: 1) the existence of a transition layer near the interface as predicted by [43, 63] and its effect on the definition of an effective wavenumber in the sediment; and 2) the effect of the half-space and multiple scattering on the volume scattering cross-section.

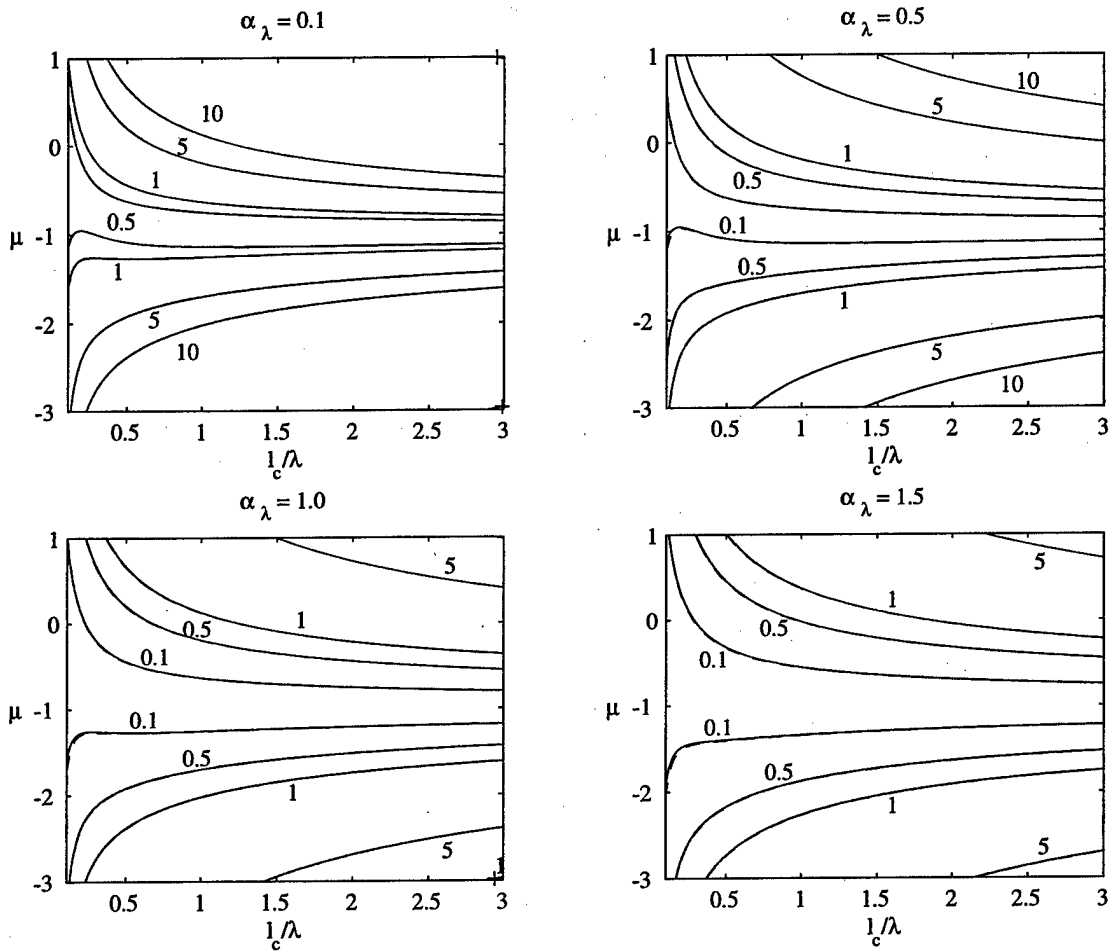


Figure 4.3: First-order multiple scattering compared to the bilocal approximation: Contours of γ_e'' as a function of l_c/λ , μ , and α_λ . The solid contour lines are found using first-order multiple scattering, the dashed contours (nearly hidden below the solid contours) are found using the bilocal approximation with a small variance. All contours are calculated with $\sigma_\rho^2 = 0.01$.

Simulations are performed in two dimensions, and the multiple scattering theory is for three dimensions. Therefore, the comparison of the results of numerical simulations with the results of multiple scattering theory is limited to relative magnitudes. The exact magnitudes of the effective wavenumbers found using both methods can not be compared directly. Multiple scattering theory could be derived for two-dimensional scattering. However, the derivation of the mass operator is much more difficult with the two-dimensional Green's function (a Hankel function), and it is not done in this thesis.

4.2.1 *Half-Space Effects on the Mean Field*

Consider first the scattered field within the sediment. As in the previous section where Dyson's equation was used, multiple scattering can be observed by examining the mean field. The mean field is generated by performing Monte-Carlo simulations and averaging the total field over a sufficient number of realizations to remove the incoherent field. A periodic medium is used to allow for plane wave propagation, and the incident field is normal to the interface. Six cases are examined using parameters of the medium that correspond to typical sand sediments. The cases are defined in Figure 4.4 over a range of μ and correlation scales, l_c/λ . Multiple scattering theory predicts that in these cases the effective wavenumber will be influenced by at least first-order multiple scattering. Figure 4.5 illustrates the geometry, the incident field, and mean fields within the scattering volume of the numerical simulations. The incident field (Figure 4.5a) is normal to the interface at $z = 0$. The mean field (Figure 4.5b) is an average over 50 realizations.

The bilocal approximation for an unbounded medium predicts an effective wavenumber at which the mean field propagates in the scattering medium. However, near the interface the definition of an effective medium is obscured. Figure 4.6 shows numerically estimated values of γ_e'' as a function of depth into the half-space, found using the estimated effective wave number of the mean field. The estimates of the

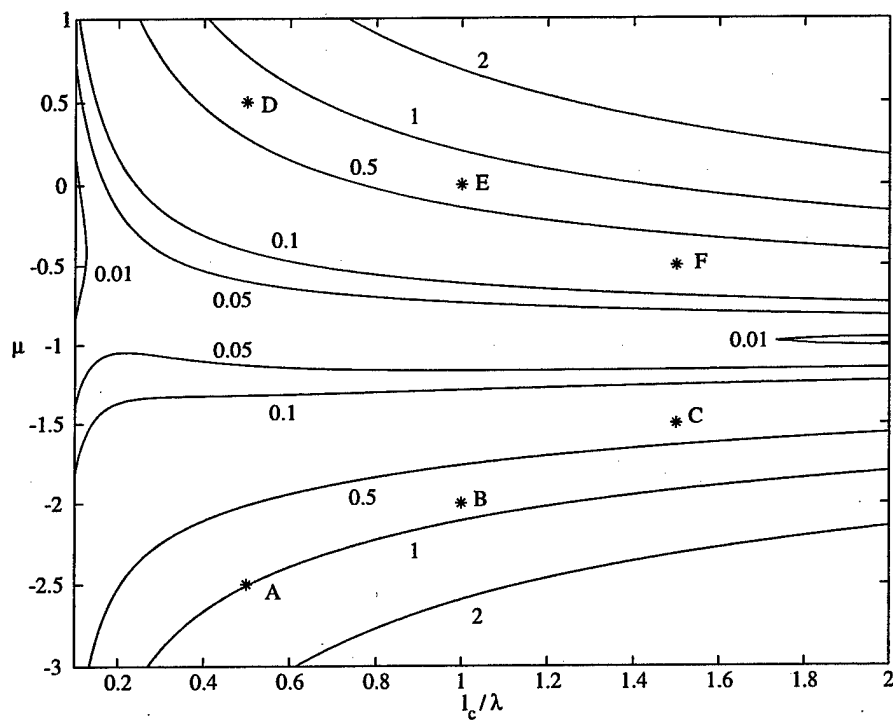


Figure 4.4: Cases for which effective wavenumber are estimated. $\rho/\rho_0 = 2.0$, $c/c_0 = 1.2$, $\alpha_\lambda = 1.0$, $\sigma_\rho^2 = 0.01$.

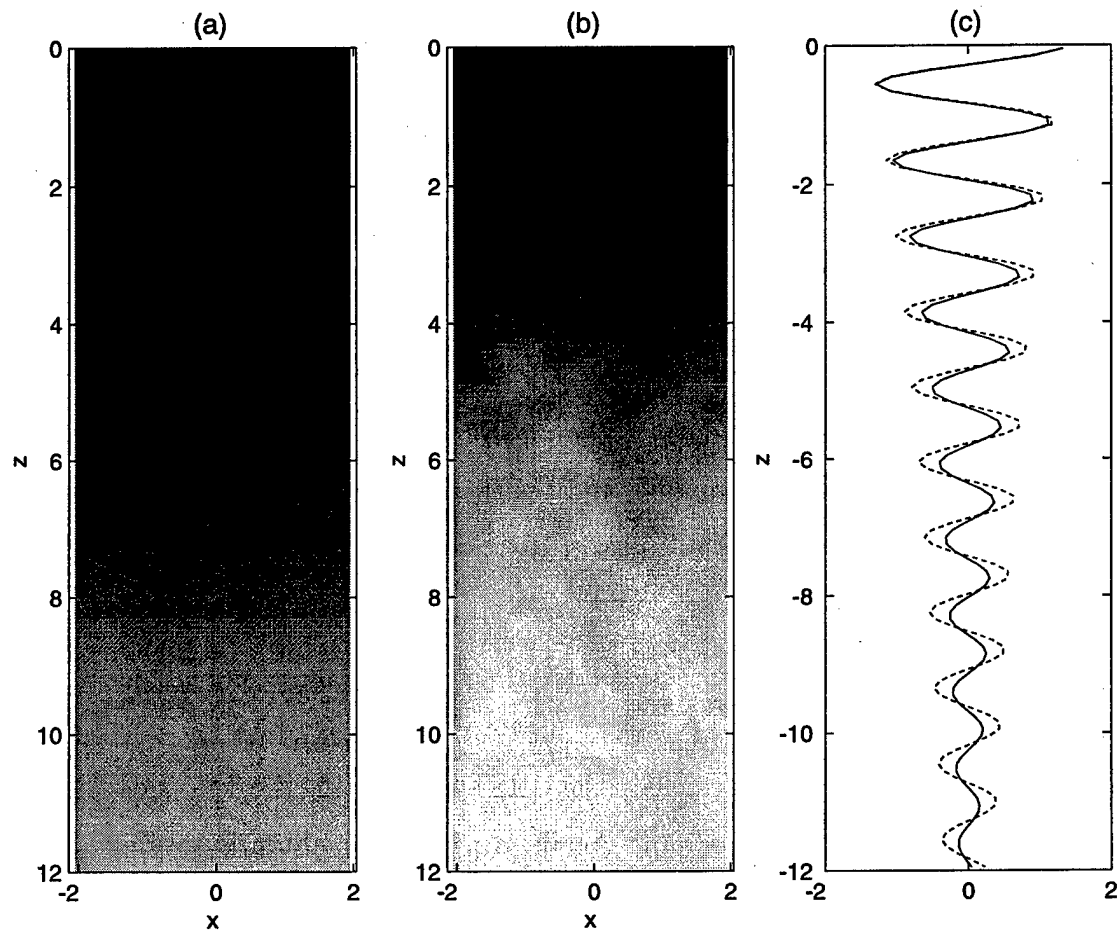


Figure 4.5: The magnitude of: (a) the incident field; (b) the mean field; and (c) the horizontally averaged real components of the incident field (dashed line) and mean field (solid line) within the scattering volume of a periodic medium. Sediment parameters correspond to case *B* in Figure 4.4. The incident field is normal to the interface at $z = 0$. All coordinates are normalized by the wavelength.

effective wavenumber are found by solving for the z -component of the exponent of the wave field at each point in the depth direction:

$$[\mathbf{k}_e - \bar{\mathbf{k}}] \cdot \hat{z} = \frac{\ln(\langle p \rangle / p_0)}{-iz}. \quad (4.38)$$

The estimate of the mean field $\langle p \rangle$ is found by averaging Monte-Carlo simulations, and p_0 is the incident field. Within a transition layer near the interface, the scattering attenuation increases from approximately zero at the interface to a constant value. The depth at which the effective wavenumber becomes constant is the depth of the transition layer. In all cases, the depth of the transition layer is larger than the correlation length of the medium, with larger correlation lengths showing larger transition layers.

As mentioned previously, no direct comparison can be made between the numerically estimated effective wavenumber and the three-dimensional bilocal approximation. However, the relative magnitudes of the test cases agree with the theoretical predictions.

4.2.2 Bistatic Scattering Strength

Next, consider the scattered far-field in the UHS by estimating the equivalent surface scattering strength for the medium. Again, a periodic medium is assumed. The scattering strength is found by estimating the variance of the scattered far-field for a large number of realizations. Because a periodic medium is used, the scattering angles are limited by the Floquet modes, and the scattering cross-section is defined using (2.133). Figure 4.7 shows the bistatic scattering strength for different incident angles for case B of Figure 4.4. A critical angle exists at 24.6°

The bistatic scattering strengths for various incident angles above and below the critical angle show good agreement with first-order perturbation results. The solid and dashed lines are the formally averaged perturbation theory with and without half-space effects. The dots are the numerically calculated scattering strength. Half-

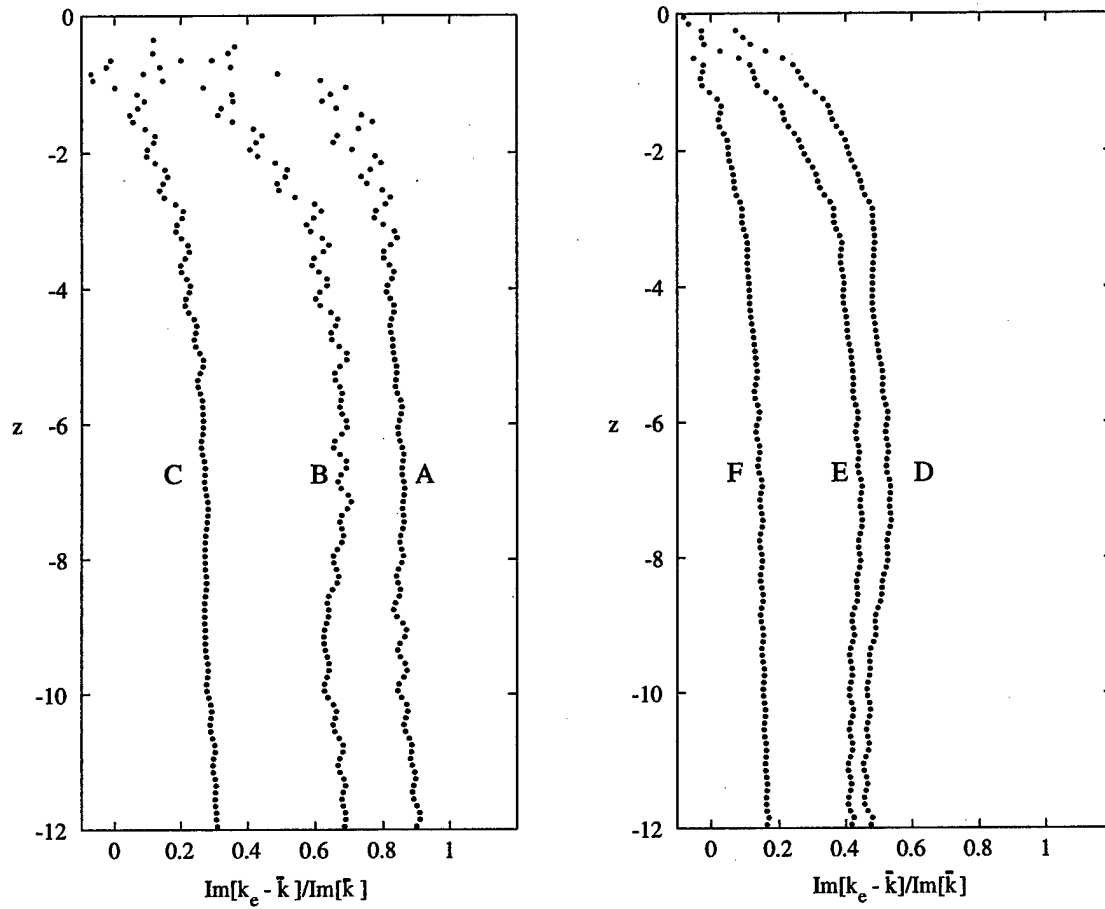


Figure 4.6: Estimate of γ_e'' as a function of depth for different values of μ and l_c/λ defined in Figure 4.4.

space effects are significant in the specular direction. Although multiple scattering is observed in the scattering medium (as shown by the mean field), the scattering strength is modeled well by first-order perturbation methods.

4.2.3 Assessment of Multiple Scattering in Marine Sediments

Figure 4.8 shows four different contour plots of γ_e'' for four different marine sites. The sediment physical properties at each site were estimated from cores samples [34, 14]. The measured sediment parameters μ and l_c/λ are plotted as points (*) on the contour plots. For the estimated sediment parameters and the frequencies used, multiple scattering theory predicts that no significant multiple scattering of the field within the sediment will occur at three of the sites ($\gamma_e'' < 5\%$). The Panama City site shows fairly strong scattering within the sediment ($\gamma_e'' \approx 10\%$). The sediments at the Eckernfoerde and Orcas sites are primarily silt and mud. The Key West and Panama City sites are primarily sand.

A primary indicator of multiple scattering in marine sediments (at least at these four sites) is the amplitude of the cross-correlation between the compressibility and density. In general, compressibility and density are negatively correlated and of comparable magnitude. This leads to $\mu \approx -1$, and multiple scattering is minimal. For values of μ away from negative unity, compressibility and density act to enhance multiple scattering. The Panama City site in Figure 4.8 shows non-negligible multiple scattering due to the relatively high estimate of $\mu \approx -2.5$.

4.3 Summary and Conclusions

The bilocal approximation to Dyson's equation for the coherent field is extended to include density, as well as compressibility, fluctuations in volume scattering from a continuous Gaussian random medium. The Gaussian medium assumption is only used to develop a bilocal approximation for sediment volume scattering that can be

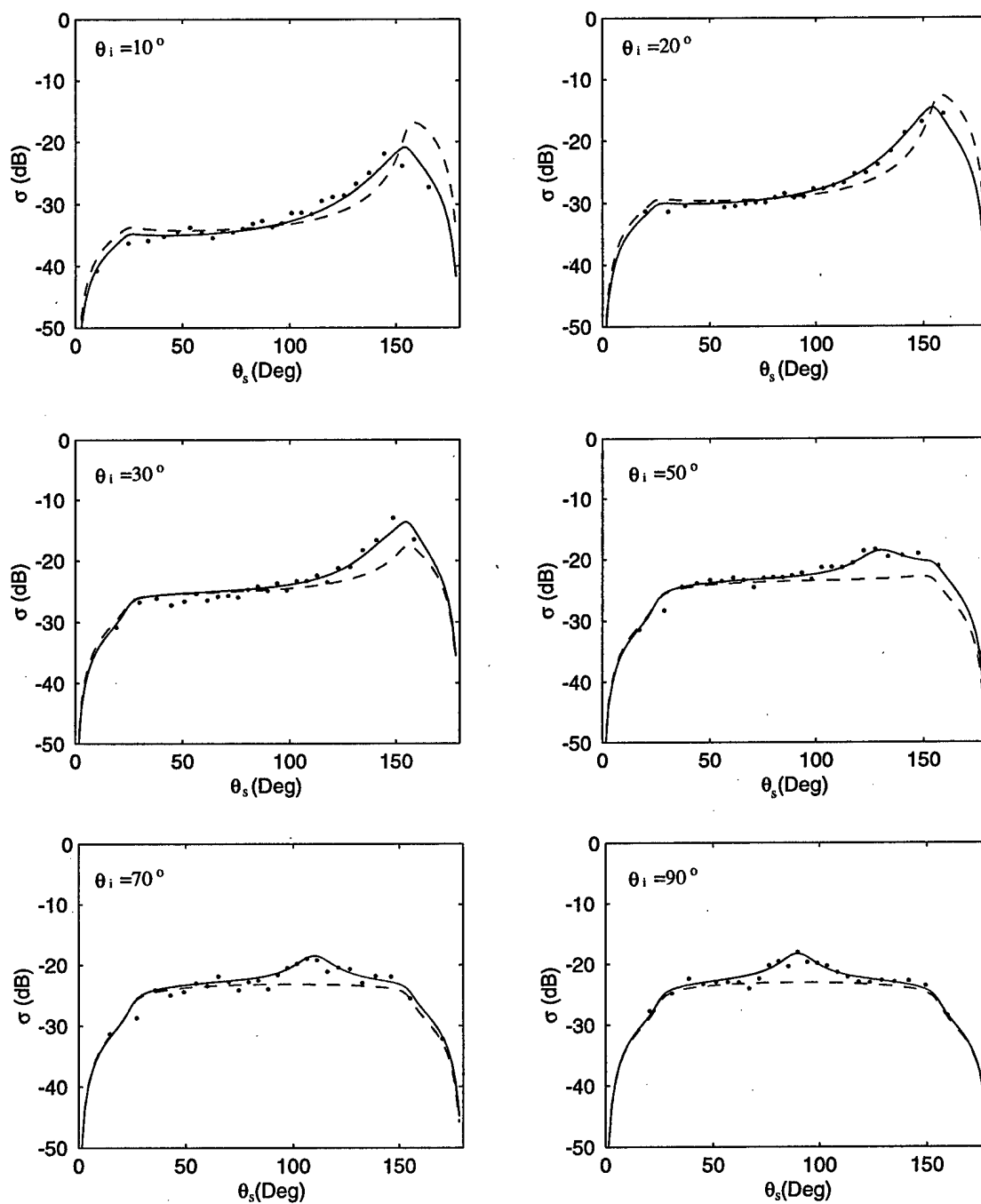


Figure 4.7: Bistatic scattering strength for various angles of incidence for case *B* of Figure 4.4. Critical angle of 24.6° .

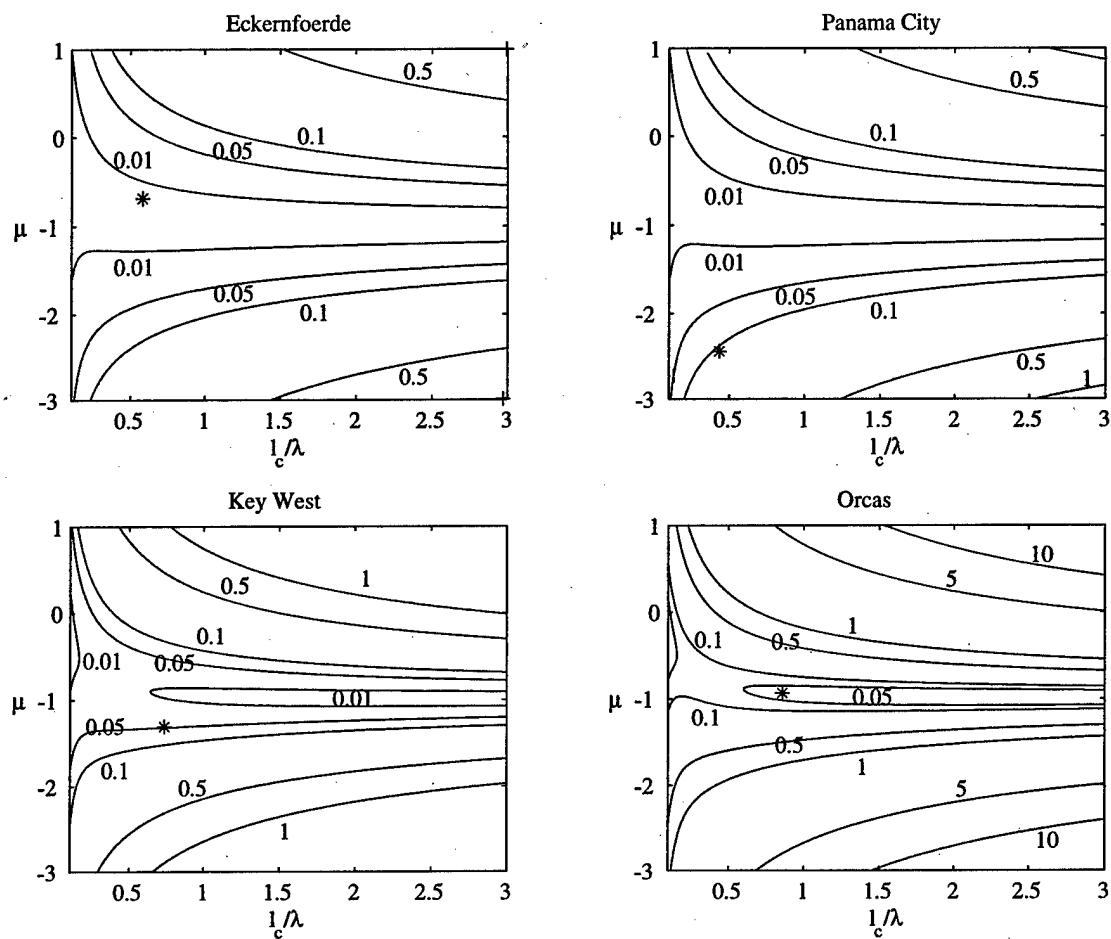


Figure 4.8: Contours of γ_e'' for several sites. The * indicates the values of l_c/λ and μ estimated from core data at each site. Eckernfoerde: $\alpha_\lambda = 0.1, \sigma_\rho = 0.01$, Panama City: $\alpha_\lambda = 0.9, \sigma_\rho = 0.03$, Key West: $\alpha_\lambda = 0.5, \sigma_\rho = 0.045$, Orcas: $\alpha_\lambda = 0.1, \sigma_\rho = 0.045$.

used to study the applicability of the small perturbation method. It is not intended as a realistic model of sediment fluctuations.

The effective wavenumber in the scattering medium is found using the bilocal approximation. Alternatively, the effective wavenumber is found using a first-order multiple scattering method. The two expressions for the effective wavenumber agree well for typical values of sediment physical properties. However, they differ slightly at $l_c/\lambda \ll 1$ near $\mu = -1$ (as shown numerically).

The effective wavenumber within the sediment half-space is found by numerical Monte-Carlo simulations using the method of moments (for several test cases). The numerical simulations show the existence of a transition layer near the sediment-water interface, as predicted by one-dimensional theory [63, 43]. The UHS scattering strength for a typical marine sediment is also calculated using numerical simulations. The bilocal approximation for the effective wavenumber in the sediment predicts that multiple scattering is present in some cases. However, numerical simulations of the scattering strength in the UHS still show good agreement with the first-order perturbation model (2.88) when half-space effects are included.

One conclusion that can be drawn from this analysis is that good estimates of the physical properties of sediment are critical for making predictions of scattering. Good estimates of μ are especially important. The current measurements of μ indicate that first-order multiple scattering within the sediment is significant for the Panama City site, for example. However, the core analysis used in this case may not have provided adequately accurate estimates of μ to make reliable predictions.

A final judgment as to the applicability of the weak scattering assumption in marine sediments cannot be made. Further research is needed to address the proportionality of sediment density and compressibility fluctuations. If the assumption of proportionality can be verified, the range of values of μ for typical sediments must be established. If a constitutive relation between density and compressibility cannot be established, the effects of uncorrelated scattering between density and

compressibility fluctuations must be addressed.

For far-field scattering from the sediment into the UHS, an important conclusion can be made. In general, it is observed from numerical simulations that even when multiple scattering is present in the medium, first-order estimates for the scattering strength are good approximations to the true scattering strength. This is assumed to be the case in typical marine sediments, and it is assumed to be true for the cases shown in Figure 4.8.

An explanation for this is most likely found in the transition layer near the sediment-water interface. As observed through numerical simulations, multiple scattering diminishes near the interface. This is shown in the estimates of the depth-dependent effective wavenumber in the scattering medium (Figure 4.6). The scattered field in the UHS, however, is more strongly influenced by scattering from the sediment near the interface - because attenuation limits the depth to which the incident field will penetrate. Therefore, if multiple scattering is diminished in the volume of the sediment near the interface (which most influences the scattered far-field), it is expected that weak scattering methods will model the scattered far-field adequately. In other words, half-space effects that create a transition layer in the upper sediment diminish the effects of multiple scattering on the far-field scattering strength.

Chapter 5

BIOLOGICAL SOURCES OF HETEROGENEITY IN SEDIMENTS

Identifying the specific mechanisms by which benthic organisms mix sediment is critical in the development of a mathematical model of bioturbation. However, generalization to an arbitrary level of description seems exceedingly difficult due to the variety, complexity and irregularity of bioturbational processes. Exceptions to the general behavior of organisms will always require unique treatment in a model. For example, communities of organisms may affect actions of individuals in ways that may be unique to a particular environment [4]. It seems realistic, however, to model the cumulative effects of bioturbation and the subsequent effects on sediment properties in a statistical sense - that is, to develop models that describe the stochastic properties of the mixing process without attempting to model the behavior of individual organisms.

This chapter will begin with a brief review of the activities of benthic organisms that cause sediment mixing and heterogeneity (at least the activities that affect the physical properties of sediments). Then, a review of current mathematical models of bioturbation is presented, keeping in mind that these models were developed for other purposes (and other parameterizations) than for acoustic remote sensing. Finally, a new model is presented that closely follows the existing models, but which is extended to include higher-order statistical measures of fluctuations in the sediment bulk properties. The fluctuation statistics can then be used to relate the parameters of the mixing model to the statistics of the scattered sound field.

5.1 *Mixing of Sediments by Benthic Organisms*

The activities of organisms (meiofauna and macrofauna) that live and feed in marine sediments rework the sediment and cause mixing. These activities are characterized as *deposit feeding*, *locomotion*, and *home building* [83] which in turn are characterized as either causing *local* or *nonlocal* displacement of sediment particles and pore water [1, 9]. Local displacement is a continuum of small random movements that transport sediment short distances. Nonlocal displacements are large (relative to animal body size) and discrete movements of sediment. In either case, displacements can take place in the horizontal and vertical directions with time and distance scales that may vary with direction and depth into the sediment. The precise meaning and scale of local and nonlocal will be defined later.

Deposit feeding is the bulk ingestion and subsequent egestion of particles within or upon the sediment. It is the dominant type of feeding activity that displaces sediment particles. In general, most deposit feeders must ingest large amounts of sediment material - several times their body weight per day. They often move the sediment distances comparable to, or greater than, the length of the animal. Depending on the body size of the animal in question and the mixing length scales of interest, deposit feeding may produce either local or nonlocal mixing. Some deposit feeders restrict their activities to either horizontal or vertical mixing, potentially creating anisotropic mixing. Conveyor belt or tunnel feeders, which make up the majority of deposit feeders, tend to move sediment from some depth in the sediment to the surface. Other animals transport sediment in nearly equal distances in both directions.

Locomotion is the movement of an animal from one location to another within the volume or on the surface of the sediment which results in the sediment being displaced in some manner. Movements may be due to feeding or predator-prey interactions, for example. Since a large amount of energy must be expended during

movements within the volume of the sediment, infaunal mixing of this nature will have relatively small particle displacements (local mixing) and be less intensive than mixing by deposit feeding. Epifaunal locomotion, on the other hand, is less difficult, and mobile epifauna are generally more abundant. This potentially creates higher localized horizontal mixing rates at the sediment interface. It may also influence vertical mixing by the "piping" of surface sediments into open tubes and burrows that extend vertically into the sediment.

Home building is the creation of tubes and burrows for dwellings in the sediment. The size and structure of tubes and burrows reflect the size of the animals inhabiting them and the environment in which they are built. Large volumes of sediment can be displaced and moved nonlocally by home building - comparable to mixing caused by deposit feeding. Mixing is further intensified as uninhabited homes collapse or become filled as sediment falls into them.

Other factors that affect mixing (that cannot be simply classified as one of the above) are lumped into a general category of mixing termed *incidental movements*. These include mixing that cannot be directly associated with an animal activity but which occurs as an indirect result of the above activities. For example, through a siphoning action a surface deposit-feeder will frequently dislodge sediment particles which it does not ingest [83].

5.2 Classical Diagenetic Models

Diagenesis refers to the processes that bring about changes in time and space of a sediment or sedimentary rock after deposition. Bioturbation is an important aspect of this process in marine sediments and has received a significant amount of attention and modeling. The current models typically describe the net effects of bioturbation as localized diffusion or *biodiffusion*. This section is a brief overview of the most widely published model [4, 9, 83] and provides a starting point for the development

of a more general mixing model.

Quantitative analysis of diagenesis requires the use of mathematical models that describe the mixing process. Classical diagenetic models describe the steady-state vertical mixing of the mean concentration of a sediment tracer (usually a chemical or radioisotope tracer) as an idealized mass balance between adjacent layers of sediment. Using the sediment-water interface as the origin, the rate of change of a solid or liquid tracer at a fixed depth is expressed as

$$\frac{\partial C}{\partial t} = -\frac{\partial F}{\partial z} + R, \quad (5.1)$$

where C is the bulk concentration of a biodiffusing tracer (to be identified). The units of C are mass per unit volume of sediment. The function F is the flux of C in the vertical direction, with dimensions of mass per unit area per unit time. The R term is the rate of diagenetic reaction affecting the concentration or the rate of removal or addition of tracer from outside the control volume.

For loose marine sediments, this type of rate equation is used to describe the conservation of fluid and/or solid trace species. The tracer may refer to the concentration of a dissolved solute in the sediment pore water, such that

$$C = \phi C_f, \quad (5.2)$$

where C_f is mass of solute per unit volume of pore water, and ϕ is the sediment porosity. The concentration may also describe a solid species, in which case

$$C = (1 - \phi)C_s, \quad (5.3)$$

where C_s is the mass of tracer per unit volume of solid. Solids are typically discrete sediment grains immersed in the pore water. The trace quantity may also refer to the total fluid mass, in which case $C_f = \phi\rho_f$, or total solid mass such that $C_s = (1 - \phi)\rho_s$, where ρ_f and ρ_s are the fluid and solid mass densities, respectively. The trace quantity may also be the total combined sediment mass, such that

$$C = \phi\rho_f + (1 - \phi)\rho_s. \quad (5.4)$$

The flux F is the result of diffusion and/or advection. The advection of a tracer relative to the sediment-water interface is primarily due to depositional burying, compaction, and, depending on the environment, externally impressed hydrological flow. Deposition results in a net flux downward into the sediment relative to the sediment-water interface. Compaction of sediment due to gravity results in a vertical flow of pore water. On the time scales of interest in this thesis, deposition and compaction will be neglected. In principle, nonlocal mixing can also cause advection. For example, deposit feeding may result in a net upward or downward advection of sediment due to "conveyer-belt" feeding.

Local diffusional flux is in general due to bioturbation and molecular diffusion. Considering only bioturbational diffusion, and ignoring molecular diffusion, the total localized flux within the sediment is proportional to the gradient of the tracer concentration. The net effect of bioturbation is lumped into a single parameter, the *biodiffusion* coefficient D_b , such that

$$F = -D_b \frac{\partial C}{\partial z} . \quad (5.5)$$

The diffusive nature of bioturbation is not the result of the activities of a single type of organism, but it is rather the net effect of a collection of infauna having a wide range of mixing lengths that are small compared to the length scales of the volume of sediment being considered.

The resulting vertical biodiffusion equation is

$$\frac{\partial C}{\partial t} - D_b \frac{\partial^2 C}{\partial z^2} = R . \quad (5.6)$$

A typical model assumes a zone of biodiffusional mixing near the sediment-water interface ($0 > z > -L$) over which D_b is constant and below which animal activities are negligible with $D_b = 0$. The depth at which bioturbational mixing stops is referred to as the rework depth L . Below the rework depth, other flux mechanisms are dominant, such as molecular diffusion. To model anisotropic and inhomogeneous

biodiffusion, the diffusion equation can be generalized into three dimensions,

$$\frac{\partial}{\partial t}C(\mathbf{r}, t) - \nabla \cdot [D_b(\mathbf{r}, t)\nabla C(\mathbf{r}, t)] = R(\mathbf{r}, t), \quad (5.7)$$

where the biodiffusion coefficient is now a dyad.

5.2.1 Nonlocal Mixing

Nonlocal mixing is defined as any mixing that cannot be described as diffusive. To complete this definition it is necessary to define what is meant by diffusive in the context of sediment mixing. To start, consider conservation of a trace quantity c_i at layer i in a one-dimensional sediment comprised of thin layers [9, 8]. The rate of change of c_i due to the instantaneous exchange of sediment from all other layers is

$$\frac{dc_i}{dt} = \sum_{j=1}^N K_{ij}c_j\Delta z - \sum_{j=1}^N K_{ji}c_i\Delta z. \quad (5.8)$$

The constant K_{ij} specifies the rate at which sediment is exchanged from layer j to layer i (with units of inverse time and distance). Figure 5.1 illustrates exchange between a finite number of layers. Deposition at the sediment-water interface creates advection downward relative to the interface-centered coordinate system. Local exchange is illustrated as exchange between adjacent layers, and nonlocal exchange is between non-adjacent layers. Generalizing to a continuum in three dimensions, (5.8) is rewritten as an integro-differential equation in terms of a general exchange function K that describes all scales of mixing:

$$\begin{aligned} \frac{\partial}{\partial t}c(\mathbf{r}, t) = & \int_V K(\mathbf{r}, \mathbf{r}'; t)c(\mathbf{r}', t)d\mathbf{r}' \\ & - c(\mathbf{r}, t) \int_V K(\mathbf{r}', \mathbf{r}; t)d\mathbf{r}'. \end{aligned} \quad (5.9)$$

Conservation of the trace quantity follows from (5.9) by integrating over the control volume:

$$\frac{d}{dt} \int_V c(\mathbf{r}, t)d\mathbf{r} = 0. \quad (5.10)$$

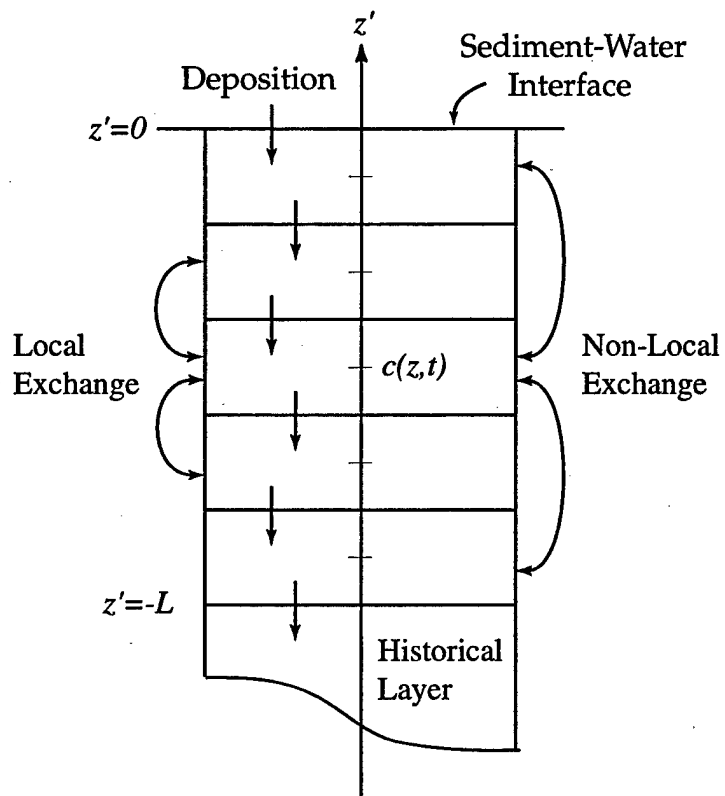


Figure 5.1: Local and non-local mixing between layers of sediment.

In general, sediment is composed of a collection of complex and heterogeneous sediment grains. In describing a continuous trace quantity (concentration, density, etc.) it is necessary to consider a sample volume over which the point function (e.g. mass of particular substance) is spatially averaged. This is accomplished by defining the sample filtering function $s(\mathbf{r})$, such that

$$C(\mathbf{r}, t) = \int_V c(\mathbf{r}', t) s(\mathbf{r} - \mathbf{r}') d\mathbf{r}' , \quad (5.11)$$

where

$$\int_V s(\mathbf{r}) d\mathbf{r} = 1 . \quad (5.12)$$

The sampling filter must have a characteristic dimension (width) large enough to define the specific quantity of interest but small enough to provide adequate spatial resolution. Usually, the scale of the required spatial resolution dictates the sample filtering scale. For example, acoustic waves interact with fluctuations in the sediment bulk properties at length scales comparable to the acoustic wavelength. Therefore, an appropriate sample filter for measuring sediment acoustic properties (density, sound speed) should have a length scale much greater than the grain size but smaller than the acoustic wavelength.

To gain insight into the effects of sample filtering on the mixing equation, the operator (5.11) is applied to the mixing equation (5.9) to yield

$$\begin{aligned} \frac{\partial}{\partial t} C(\mathbf{r}, t) = & \iint_V K(\mathbf{r}'', \mathbf{r}'; t) c(\mathbf{r}', t) s(\mathbf{r} - \mathbf{r}'') d\mathbf{r}' d\mathbf{r}'' \\ & - \iint_V K(\mathbf{r}', \mathbf{r}''; t) c(\mathbf{r}'', t) s(\mathbf{r} - \mathbf{r}'') d\mathbf{r}' d\mathbf{r}'' . \end{aligned} \quad (5.13)$$

A comparison of the spatial scales of the exchange function and the filtering function will give definition to the terms local and nonlocal mixing [Jackson-personal communication].

Local mixing is defined as exchange on scales smaller than the scale of the filtering function - that is, when $K(\mathbf{r}'', \mathbf{r}'; t)$ restricts mixing to length scales that are much

smaller than the width of $s(\mathbf{r} - \mathbf{r}'')$. If this is assumed, the filtering function can be expanded in a Taylor series in $(\mathbf{r}'' - \mathbf{r}')$:

$$\begin{aligned} s(\mathbf{r} - \mathbf{r}'') &= s(\mathbf{r} - \mathbf{r}') + (\mathbf{r}' - \mathbf{r}'') \cdot \nabla s(\mathbf{r} - \mathbf{r}') \\ &+ \frac{1}{2} [(\mathbf{r}' - \mathbf{r}'') \cdot \nabla]^2 s(\mathbf{r} - \mathbf{r}') + \dots \end{aligned} \quad (5.14)$$

Using the first three terms in the Taylor series, and assuming $K(\mathbf{r}'', \mathbf{r}')$ restricts $|\mathbf{r}' - \mathbf{r}''|$ to scales much smaller than the width of s , then $s(\mathbf{r} - \mathbf{r}') \simeq s(\mathbf{r} - \mathbf{r}'')$ within the mixing integrals. The mixing equation (5.13) can now be rewritten as

$$\begin{aligned} \frac{\partial}{\partial t} C(\mathbf{r}, t) &= \int_V \mathbf{u}(\mathbf{r}', t) \cdot \nabla [c(\mathbf{r}', t) s(\mathbf{r} - \mathbf{r}')] d\mathbf{r}' + \\ &\nabla \cdot \int_V \mathbf{D}(\mathbf{r}', t) \cdot \nabla [c(\mathbf{r}', t) s(\mathbf{r} - \mathbf{r}')] d\mathbf{r}' , \end{aligned} \quad (5.15)$$

where the new mixing parameters are defined as

$$\mathbf{u}(\mathbf{r}', t) = \int_V K(\mathbf{r}'', \mathbf{r}'; t) (\mathbf{r}'' - \mathbf{r}') d\mathbf{r}'' \quad (5.16)$$

and

$$\mathbf{D}(\mathbf{r}', t) = \frac{1}{2} \int_V K(\mathbf{r}'', \mathbf{r}'; t) (\mathbf{r}'' - \mathbf{r}')^2 d\mathbf{r}'' . \quad (5.17)$$

The function \mathbf{D} is the dyadic diffusion coefficient, and \mathbf{u} is a vector function that describes advection in the local mixing process due to asymmetry in the local exchange function about the point \mathbf{r} . If \mathbf{u} and \mathbf{D} are constants in space, or slowly varying functions compared to the filtering function, then (5.15) reduces to a diffusion equation in terms of the filtered quantity:

$$\frac{\partial}{\partial t} C(\mathbf{r}, t) = \mathbf{u}(\mathbf{r}, t) \cdot \nabla C(\mathbf{r}, t) + D(\mathbf{r}, t) \nabla^2 C(\mathbf{r}, t) . \quad (5.18)$$

If the exchange function is an even function of space, such that

$$K(\mathbf{r}) = K(-\mathbf{r}) , \quad (5.19)$$

then the coefficient u will vanish, and there will be no advection. Assuming isotropy in the exchange function, the familiar diffusion equation results:

$$\frac{\partial}{\partial t} C(\mathbf{r}, t) = D(\mathbf{r}, t) \nabla^2 C(\mathbf{r}, t). \quad (5.20)$$

Therefore, local mixing is defined as sediment exchange on scales smaller than the sample filter length scale. Local exchange is characterized by diffusive mixing.

Nonlocal mixing is defined as exchange of sediment on scales much larger than the sample filter length scale. Nonlocal mixing is non-diffusive. In this regime of mixing, the filter function $s(\mathbf{r})$ is a narrow function in space compared to the exchange function $K(\mathbf{r})$. The mixing equation (5.13) can then be rewritten in terms of the averaged quantity C , and the nonlocal mixing equation results:

$$\begin{aligned} \frac{\partial}{\partial t} C(\mathbf{r}, t) = & \int_V K(\mathbf{r}, \mathbf{r}'; t) C(\mathbf{r}', t) d\mathbf{r}' \\ & - C(\mathbf{r}, t) \int_V K(\mathbf{r}', \mathbf{r}; t) d\mathbf{r}'. \end{aligned} \quad (5.21)$$

5.3 *Inhomogeneous Biodiffusion of Sediment Bulk Properties*

The mixing of a sediment tracer (for example, a radioisotope with a relatively long half-life) is modeled remarkably well by the homogeneous and steady-state solution of the biodiffusion equation. This has been shown by comparison of theoretical results with measured vertical profiles of tracer concentration taken from sediment cores. Typically, many cores are taken in a particular area to develop a statistical ensemble. Each core profile represents a single realization of the random mixing process. Any particular core may include disturbances associated with sediment microenvironments such as strong gradients in porosity around burrows or corpses of larger organisms [4, 9]. The ensemble of core profiles is then averaged to find the mean concentration of the tracer of interest as a function of depth. The average profile is then compared with the theoretical profile for a biodiffusive process and a biodiffusion coefficient is inferred.

In the context of acoustic scattering, however, the fluctuations in the cores from realization to realization are of primary interest. Acoustic scattering provides a measure of the correlation structure of the sediment density fluctuations. Therefore, to use acoustic scattering as a means of measuring bioturbational mixing, it is necessary to investigate the transient and heterogeneous nature of the mixing process and develop a model that can be used to describe higher-order statistics - at least the correlation of the medium fluctuations.

A starting point to develop such a model is the mixing equation (5.21). Since this model is intended for acoustic remote sensing, the trace species of interest will be the sediment bulk density. Therefore, using (5.4), with

$$C = \rho \equiv \phi\rho_f + (1 - \phi)\rho_s, \quad (5.22)$$

and using the mixing equation (5.21), the rate of change of total mass (fluid and solid) is described as

$$\frac{\partial}{\partial t}\rho(\mathbf{r}, t) = \int_V K(\mathbf{r}', \mathbf{r}; t)\rho(\mathbf{r}', t)d\mathbf{r}' - \rho(\mathbf{r}, t) \int_V K(\mathbf{r}, \mathbf{r}'; t)d\mathbf{r}'. \quad (5.23)$$

By using the bulk density as the trace quantity, it is assumed that the solid and fluid mass of the sediment grains and pore water are mixed as a single quantity. Alternatively, the porosity could be considered constant, and only the sediment grains (without pore water) would be subject to biodiffusional mixing [4]. This macroscopic view of mixing ignores the particular mechanism by which an organism transports sediment. The proper trace quantity to use for a particular sediment type and environment has yet to be established. Only bulk density will be used in this thesis; however, the modeling methodology is general.

To start, several assumptions about the mixing process are made. First, owing to the modal characteristic of the size spectrum of organisms, it is assumed that mixing takes place on two scales: 1) local biodiffusional mixing that represents the continuous diffusive activity of smaller organisms (meiofauna) or the collapsing

and filling of borrows created by larger organisms; and 2) nonlocal mixing that represents the activities of larger organisms (macrofauna). On the time scales of interest, the movement of sediment is not necessarily restricted to localized mixing between adjacent horizontal layers. Rather, larger organisms may transfer sediment between non-adjacent layers creating nonlocal (non-diffusive) mixing that gives rise to spatial heterogeneity. Furthermore, over short time periods, it cannot be assumed that a large collection of organisms with a broad spectrum of sizes has reworked the sediment. Nonlocal mixing may be dominated by a single or several types of organisms with characteristic length scales. Therefore, the second assumption is that the activities of the larger macrofaunal organisms are discrete in both space and time, and the activity of meiofauna is assumed to be continuous in space and time.

The exchange function K describes the spatial and temporal characteristics of mixing. In the simplest form (as a continuous function or a constant), it describes total mixing within the sediment volume. In this case, every point in the volume exchanges sediment with every other point in the volume; mixing occurs on all scales. To describe a two-scale mixing process (as motivated above) K is divided in two components - local and nonlocal exchange - that have a finite (but not overlapping) spatial extent. The components are assumed to be independent of each other; therefore, they can be superimposed to describe the total exchange as

$$K(\mathbf{r}', \mathbf{r}; t) = K_l(\mathbf{r}', \mathbf{r}; t) + K_{nl}(\mathbf{r}', \mathbf{r}; t) . \quad (5.24)$$

The function K_l represents the continuous and random *local* exchange of sediment by meiofauna (diffusive mixing). The function K_{nl} represents the discrete (in time and space) *nonlocal* mixing due to larger animals.

The random and discrete nature of the nonlocal mixing is described by modeling K_{nl} as a series of source and sink functions that are distributed randomly in space and time. To start, consider only two such events - a source and sink event related

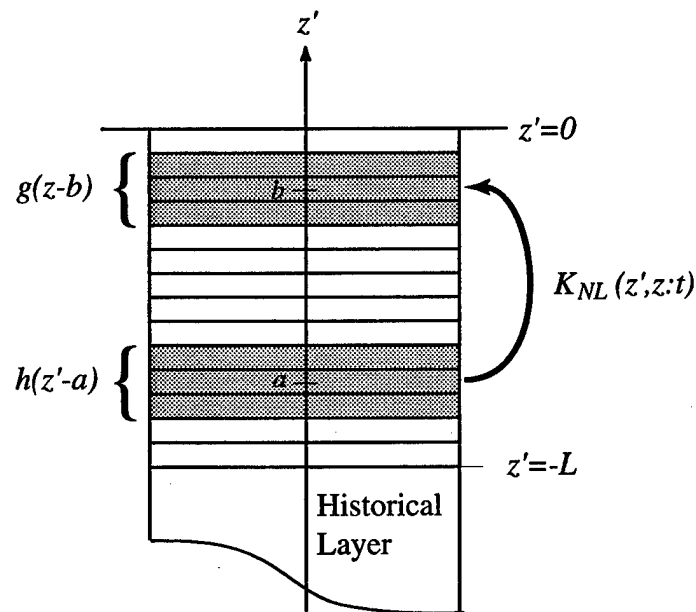


Figure 5.2: Discrete nonlocal mixing between two layered regions of sediment. Sediment is removed from a volume defined by the sink function h and deposited in a volume defined by the source function g .

to the removal and deposition of sediment by a single animal due to a single action (a single feeding motion, for example). Suppose that a random mass of sediment q is removed (nonlocally) at time ζ from a location described by the function $h(\mathbf{r} - \mathbf{a})$. The position vector \mathbf{a} is at the center of the volume, and h describes the shape of the volume of sediment where the mass was removed. The sediment is then deposited at some later time, ξ , in a location defined by the function $g(\mathbf{r} - \mathbf{b})$, where \mathbf{b} is the central location and g describes the shape of the volume of sediment where the mass is deposited. While the sediment is being transferred, assume that it is temporarily removed from the system and no mass is lost during transport. The mass removed and deposited is described by the random variable q . Figure (5.2) illustrates nonlocal mixing in an idealized one-dimensional system of layers.

It is further assumed that a nonlocal mixing event causes the removal and deposition of a fixed amount of mass - as opposed to a fixed mass per unit volume.

With this assumption, the amount of mass transferred (for nonlocal mixing only) is *not* a function of the density at the location of removal. The exchange function for nonlocal mixing will be factorized as

$$\rho(\mathbf{r}')K_{nl}(\mathbf{r}', \mathbf{r}; t) = qh(\mathbf{r}' - \mathbf{a})g(\mathbf{r} - \mathbf{b})\eta(t - \xi) \quad (5.25)$$

and

$$\rho(\mathbf{r})K_{nl}(\mathbf{r}, \mathbf{r}'; t) = qg(\mathbf{r}' - \mathbf{b})h(\mathbf{r} - \mathbf{a})\eta(t - \zeta) . \quad (5.26)$$

The shape functions are defined such that

$$\begin{aligned} \int_V h(\mathbf{r}' - \mathbf{a})d\mathbf{r}' &= 1 , \\ \int_V g(\mathbf{r}' - \mathbf{b})d\mathbf{r}' &= 1 ; \end{aligned} \quad (5.27)$$

therefore, they have units of inverse volume.

The function η defines the time dependence of the source and sink events. If the duration of each event is small and there are many events occurring within the time period of interest, the time dependence can be modeled as impulsive:

$$\eta(t - \zeta) = \delta(t - \zeta) . \quad (5.28)$$

In general, ξ and ζ are not independent. For example, the time of the sink event must come before the time of the source event, and the spacing between events is likely small compared to the time intervals of interest in here (days to weeks).

Using (5.25), (5.26) in (5.23), and grouping all the nonlocal terms into a single forcing term on the right hand side of the equation, the rate of change of mass at position \mathbf{r} in the sediment is

$$\frac{\partial}{\partial t}\rho(\mathbf{r}, t) - \int_V [\rho(\mathbf{r}', t)K_l(\mathbf{r}', \mathbf{r}; t) + \rho(\mathbf{r}, t)K_l(\mathbf{r}, \mathbf{r}'; t)]d\mathbf{r}' = f(\mathbf{r}, t) , \quad (5.29)$$

where

$$f(\mathbf{r}, t) = q \int_V [h(\mathbf{r}' - \mathbf{a})g(\mathbf{r} - \mathbf{b})\delta(t - \xi) - h(\mathbf{r} - \mathbf{a})g(\mathbf{r}' - \mathbf{b})\delta(t - \zeta)]d\mathbf{r}' . \quad (5.30)$$

The left hand side of (5.29) has been shown in Section 5.2.1 to reduce to the biodiffusion equation if K_l is symmetric and local. Two-scale mixing can then be modeled as a biodiffusional process where nonlocal mixing acts as a forcing function:

$$\frac{\partial}{\partial t}\rho(\mathbf{r}, t) - \nabla \cdot [D_b(\mathbf{r}, t)\nabla\rho(\mathbf{r}, t)] = f(\mathbf{r}, t). \quad (5.31)$$

Using (5.27), the nonlocal forcing function (5.30) is rewritten as

$$f(\mathbf{r}, t) = q[g(\mathbf{r} - \mathbf{b})\delta(t - \xi) - h(\mathbf{r} - \mathbf{a})\delta(t - \zeta)]. \quad (5.32)$$

This form of the diffusive mixing equation is inhomogeneous in ρ ; that is, the forcing function is not dependent on the value of ρ .

Generalizing (5.25) and (5.26) as a series of source/sink pair functions occurring randomly in space and time, the exchange function becomes

$$\rho(\mathbf{r}'; t)K_{nl}(\mathbf{r}', \mathbf{r}; t) = \sum_n q_n h_n(\mathbf{r}' - \mathbf{a}_n)g_n(\mathbf{r} - \mathbf{b}_n)\delta(t - \xi_n) \quad (5.33)$$

and

$$\rho(\mathbf{r}; t)K_{nl}(\mathbf{r}, \mathbf{r}'; t) = \sum_n q_n h_n(\mathbf{r} - \mathbf{a}_n)g_n(\mathbf{r}' - \mathbf{b}_n)\delta(t - \zeta_n). \quad (5.34)$$

The nonlocal forcing function is then described as

$$f(\mathbf{r}, t) = \sum_n q_n [g_n(\mathbf{r} - \mathbf{b}_n)\delta(t - \xi_n) - h_n(\mathbf{r} - \mathbf{a}_n)\delta(t - \zeta_n)]. \quad (5.35)$$

The source and sink functions g_n and h_n are random functions associated with the n th event. They describe a random shape of the sediment volume moved nonlocally by each event.

In general, the excitation may be anisotropic and a function of position in the sediment volume. For example, the shape of an event may be asymmetric in the horizontal and vertical directions, and biological activity may decrease with depth into the sediment. Figure 5.3 shows examples of shape function that represent: (a) head-down deposit feeding; (b) burrow hole infilling; and (c) arbitrary movements of

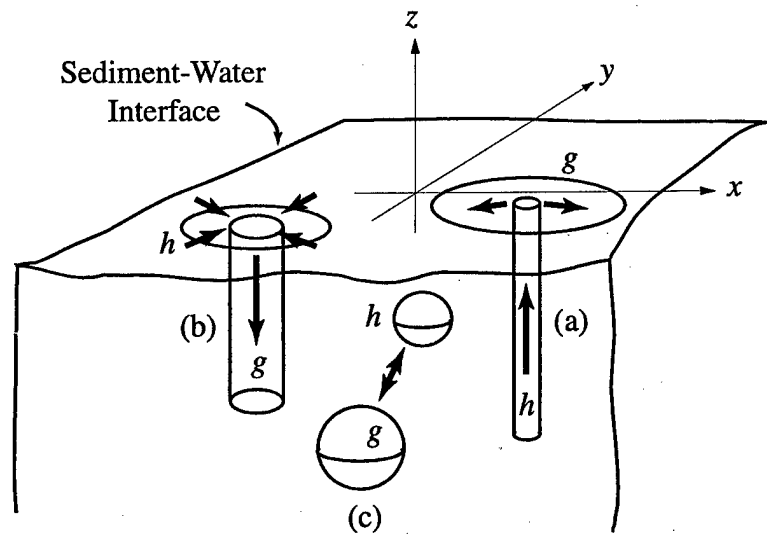


Figure 5.3: Examples of cylindrical and spheroidal source/sink shape functions that represent idealized nonlocal mixing of macrofauna: (a) head-down deposit feeding; (b) burrow hole infilling; and (c) arbitrary movements of sediment.

sediment. Figure 5.4 shows a hypothetical depth-dependent distribution of spherical shape functions. Activity is concentrated near the sediment-water interface and decreases with depth into the sediment, but it is uniform in the horizontal plane. The source and sink functions may also be location dependent. Head-down deposit feeders will deposit sediment only on the surface of the sediment, for example.

The solution to the inhomogeneous biodiffusion equation can be expressed as a convolution integral using the appropriate Green's function for the diffusive system:

$$\rho(\mathbf{r}, t) = \int_0^t \int_V g_d(\mathbf{r}, \mathbf{r}', t - \tau) f(\mathbf{r}', \tau) d\tau d\mathbf{r}' . \quad (5.36)$$

The Green's function (g_d) is the solution to the diffusion equation with an impulse

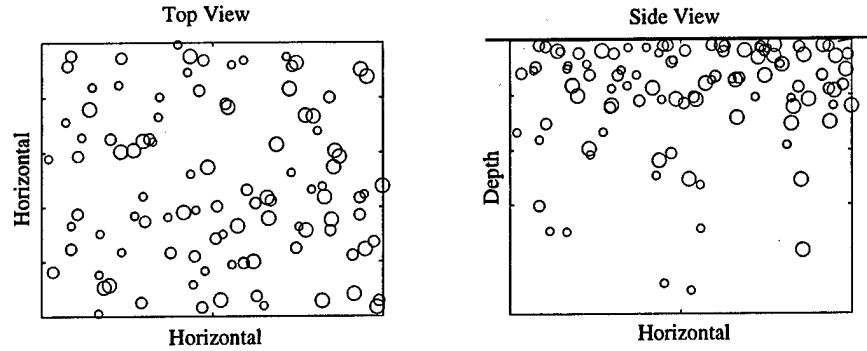


Figure 5.4: Spherical shape functions that are homogeneously distributed in the horizontal (a) and nonhomogeneously distributed in depth (b). The Poisson point density in space and time decreases with depth, concentrating activity near the sediment-water interface.

excitation:

$$\frac{\partial}{\partial t} g_d(\mathbf{r}, t; \mathbf{r}_0, t_0) - \nabla \cdot [D(\mathbf{r}, t) \nabla g_d(\mathbf{r}, t; \mathbf{r}_0, t_0)] = \delta(\mathbf{r} - \mathbf{r}_0) \delta(t - t_0). \quad (5.37)$$

The prescribed initial and boundary conditions are

$$\begin{aligned} \rho(x, y, z, t = t_0) &= \rho_0(x, y, z), \\ \frac{\partial}{\partial z} \rho(x, y, z = 0^-, t) &= 0. \end{aligned} \quad (5.38)$$

Assuming D is independent of \mathbf{r} and t , the half-space Green's function for diffusion is found, by introducing an image source across the z axis [42], to be

$$g_d(\mathbf{r}, t; \mathbf{r}_0, t_0) = \frac{e^{-R^2/[4(t-t_0)D]} + e^{-R_i^2/[4(t-t_0)D]}}{[4\pi(t-t_0)D]^{3/2}}, \quad (5.39)$$

where

$$\begin{aligned} R^2 &= (x - x_0)^2 + (y - y_0)^2 + (z - z_0)^2 \\ R_i^2 &= (x - x_0)^2 + (y - y_0)^2 + (z + z_0)^2. \end{aligned} \quad (5.40)$$

If half-space effects are neglected (as will be done in later sections), the image source is removed from the solution, and

$$g_d(\mathbf{r}, t; \mathbf{r}_0, t_0) = \frac{e^{-R^2/[4(t-t_0)D]}}{[4\pi(t-t_0)D]^{3/2}}. \quad (5.41)$$

5.3.1 Perturbation Method

Equations (5.31) and (5.35) describe nonlocal mixing in terms of an excitation function that is independent of the sediment density. This formulation follows directly from the assumption that an organism moves a fixed amount of mass during nonlocal transport, independent of the density at the location of the event. The same result can be derived using time-dependent perturbation theory.

Start by redefining the nonlocal exchange functions as

$$K_{nl}(\mathbf{r}', \mathbf{r}; t) = \sum_n v_n h_n(\mathbf{r}' - \mathbf{a}_n) g_n(\mathbf{r} - \mathbf{b}_n) s(t - \xi_n) \quad (5.42)$$

and

$$K_{nl}(\mathbf{r}, \mathbf{r}'; t) = \sum_n v_n g_n(\mathbf{r}' - \mathbf{b}_n) h_n(\mathbf{r} - \mathbf{a}_n) s(t - \zeta_n), \quad (5.43)$$

where v_n are the exchange function magnitudes that specify the fraction of the total mass present in a location that is removed or deposited. Mass rate of change is still described by (5.23), but the excitation has the form

$$f(\mathbf{r}, t) = \sum_n [u_n(t) g_n(\mathbf{r} - \mathbf{b}_n) \delta(t - \xi_n) - w_n(\mathbf{r}, t) h_n(\mathbf{r} - \mathbf{a}_n) \delta(t - \zeta_n)], \quad (5.44)$$

where the shape function magnitudes are now defined as

$$\begin{aligned} u_n(t) &= \int_V v_n \rho(\mathbf{r}', t) h_n(\mathbf{r}' - \mathbf{a}) d\mathbf{r}', \\ w_n(\mathbf{r}, t) &= v_n \rho(\mathbf{r}, t) \int_V g_n(\mathbf{r}' - \mathbf{b}) d\mathbf{r}'. \end{aligned} \quad (5.45)$$

The forced mixing equation is no longer inhomogeneous in ρ ; the forcing function is dependent on the value of ρ .

Now, assume that the fraction of sediment mass per unit volume moved by each source/sink event is small compared to initial density at that location such that

$$|h_n v_d| \ll 1 \quad \text{and} \quad |g_n v_d| \ll 1. \quad (5.46)$$

The density can then be represented in a perturbation series as

$$\rho = \rho_0 + \rho_1 + \dots, \quad (5.47)$$

where ρ_0 is the solution of the biodiffusion equation without nonlocal mixing. An equation for each order of density correction can be found by substituting (5.47) into (5.31) with the new definition of the pulse amplitudes and grouping the terms by orders of magnitude. The first-order biodiffusion equation is then found to be an inhomogeneous diffusion process:

$$\frac{\partial}{\partial t} \rho_1(\mathbf{r}, t) - \nabla \cdot [D(\mathbf{r}, t) \nabla \rho_1(\mathbf{r}, t)] = f(\mathbf{r}, t). \quad (5.48)$$

The excitation function is a series of random pulse functions with random amplitudes, as in (5.44). However, the event amplitude functions are now defined as

$$\begin{aligned} u_n(t) &= \int_V v_n \rho_0(\mathbf{r}', t) h_n(\mathbf{r}' - \mathbf{a}_n) d\mathbf{r}', \\ w_n(\mathbf{r}, t) &= v_n \rho_0(\mathbf{r}, t) \int_V g_n(\mathbf{r}' - \mathbf{b}_n) d\mathbf{r}', \end{aligned} \quad (5.49)$$

which are independent of the first-order fluctuation in density. Using (5.49) and comparing (5.44) with (5.35), the fixed mass assumption can be interpreted in terms of the perturbation result. In doing so, the mass moved by each event is defined as

$$q_n = v_n \rho_0. \quad (5.50)$$

Either approach can be used to derive the inhomogeneous biodiffusion equation.

5.3.2 Poisson Pulse Process

Consider the excitation of the inhomogeneous biodiffusion process. If the correlation of the excitation function can be found, the correlation and corresponding spectrum of the sediment density fluctuations can be found. By assuming the sequence of excitation pulse functions is a Poisson process in time, the problem is greatly simplified.

To cast the problem as a Poisson process, two assumptions are made about the stochastic properties of the random time variables: 1) the random variables ξ_n and ζ_n are statistically independent and identically distributed; and 2) the series consists of N pulses that are homogeneously distributed over a time interval of length T with $N \rightarrow \infty$ and $T \rightarrow \infty$. The probability density functions (pdfs) of all the random time variables ($\xi_1, \dots, \xi_N, \zeta_1, \dots, \zeta_N$) are then described as the product of the individual pdfs:

$$p(\xi_1, \zeta_1, \dots, \xi_N, \zeta_N) = \prod_n p_\xi(\xi_n) p_\zeta(\zeta_n). \quad (5.51)$$

The independence assumption essentially amounts to randomizing the source/sink pair functions in time. The sink that is related to a particular source can occur at any time before or after the source event. This violates causality in the mixing process. However, if a large number of events occur between observation times and initial condition effects are ignored, the cumulative effects of the events will be the same as if their order was preserved.

Similar assumptions are also made about the random position variables. Up to this point, the statistical properties of the random variables \mathbf{a}_n and \mathbf{b}_n have been general. Now, it is assumed that each event is independent and identically distributed, such that

$$p(\mathbf{a}_1, \mathbf{b}_1, \dots, \mathbf{a}_N, \mathbf{b}_N) = \prod_n p_{ab}(\mathbf{a}_n, \mathbf{b}_n). \quad (5.52)$$

The random positions \mathbf{a}_n and \mathbf{b}_n for a single event n , however, are not independent. In general, the position \mathbf{a}_n may be conditional on the position \mathbf{b}_n for the same n . This may be the case for specific types of nonlocal deposit feeding, such as head down feeding where the position of the deposition is most likely above the position of the removal of sediment, for example. It is further assumed that the random position variables are independent of any other random variables that may be defined to describe the shape functions g and h .

The correlation of the random process f in space and time is defined as

$$R_{ff}(\mathbf{r}_1, \mathbf{r}_2, t_1, t_2) = \langle f(\mathbf{r}_1, t_1)f(\mathbf{r}_2, t_2) \rangle. \quad (5.53)$$

Using (5.35) and assuming stationarity in time only (with $\tau = t_1 - t_2$), the correlation of the excitation can be expressed as a double summation with N^2 terms:

$$\begin{aligned} R_{ff}(\mathbf{r}_1, \mathbf{r}_2, \tau) = & \sum_m^N \sum_n^N [\langle q_n g_n q_m g_m \delta(t - \xi_n) \delta(t - \tau - \xi_m) \rangle \\ & - 2 \langle q_n g_n q_m h_m \delta(t - \xi_n) \delta(t - \tau - \zeta_m) \rangle \\ & + \langle q_n h_n q_m h_m \delta(t - \zeta_n) \delta(t - \tau - \zeta_m) \rangle]. \end{aligned} \quad (5.54)$$

The angle brackets are the ensemble averages over the random variables \mathbf{a}_n , \mathbf{b}_n , ξ_n , ζ_n , and any other random parameters that define the shape functions (yet to be defined). The arguments to the shape functions g_n and h_n have been dropped to save space.

Using the Poisson pulse assumption, the random time variables with $m \neq n$ are assumed to be independent. The double summation can then be divided into two parts:

$$\begin{aligned} R_{ff}(\mathbf{r}_1, \mathbf{r}_2, \tau) = & \sum_n^N [\langle q_n g_n q_n g_n \rangle \langle \delta(t - \xi_n) \delta(t - \tau - \xi_n) \rangle \\ & - 2 \langle q_n g_n q_n h_n \rangle \langle \delta(t - \xi_n) \delta(t - \tau - \zeta_n) \rangle \\ & + \langle q_n h_n q_n h_n \rangle \langle \delta(t - \zeta_n) \delta(t - \tau - \zeta_n) \rangle] \\ & + \sum_{m \neq n}^N [\langle q_n g_n \rangle \langle q_m g_m \rangle \langle \delta(t - \xi_n) \rangle \langle \delta(t - \tau - \xi_m) \rangle \\ & - 2 \langle q_n g_n \rangle \langle q_m h_m \rangle \langle \delta(t - \xi_n) \rangle \langle \delta(t - \tau - \zeta_m) \rangle \\ & + \langle q_n h_n \rangle \langle q_m h_m \rangle \langle \delta(t - \zeta_n) \rangle \langle \delta(t - \tau - \zeta_m) \rangle]. \end{aligned} \quad (5.55)$$

The function $\langle q_n g_n \rangle$ is the first moment of the source function (to be discussed later), defined as

$$\langle q_n g_n \rangle = \langle q_n g_n(\mathbf{r} - \mathbf{b}_n) \rangle. \quad (5.56)$$

The function $\langle q_n h_n \rangle$ is the first moment of the sink. The function $\langle q_n g_n q_n g_n \rangle$ is the second moment of the source function, defined as

$$\langle q_n g_n q_n g_n \rangle = \langle q_n^2 g_n(\mathbf{r}_1 - \mathbf{b}_n) g_n(\mathbf{r}_2 - \mathbf{b}_n) \rangle. \quad (5.57)$$

Similarly for $\langle q_n g_n q_n h_n \rangle$ and $\langle q_n h_n q_n h_n \rangle$.

Since the random time functions are impulsive and homogeneously distributed over time T , the ensemble averaging over time can be performed, resulting in

$$\begin{aligned} \langle \delta(t - \zeta_n) \rangle &= \frac{1}{T}, \\ \langle \delta(t - \zeta_n) \delta(t - \tau - \zeta_n) \rangle &= \frac{1}{T} \delta(\tau). \end{aligned} \quad (5.58)$$

In addition, since the random variables are independent and identically distributed, the summations can be eliminated. The first summation contains N identical terms, and the second summation contains $N(N - 1)$ identical terms. Equation (5.55) is then rewritten as

$$\begin{aligned} R_{ff}(\mathbf{r}_1, \mathbf{r}_2, \tau) &= \frac{N}{T} [\langle q^2 g g \rangle + \langle q^2 h h \rangle] \delta(\tau) - \frac{2N}{T^2} \langle q^2 g h \rangle \\ &\quad + \frac{N(N - 1)}{T^2} [\langle q g \rangle - \langle q h \rangle]^2. \end{aligned} \quad (5.59)$$

The angle brackets now represent the ensemble average over the random variables \mathbf{a} , \mathbf{b} and the other random parameters that define g and h . As N and T become large, the Poisson point density in time is defined as

$$\lambda_t = \frac{N}{T}. \quad (5.60)$$

The second term in (5.59) will then vanish in the limit, and the excitation correlation can be rewritten as

$$R_{ff}(\mathbf{r}_1, \mathbf{r}_2, \tau) = \lambda_t [\langle q^2 g g \rangle + \langle q^2 h h \rangle] \delta(\tau) + \lambda_t^2 [\langle q g \rangle - \langle q h \rangle]^2 \quad (5.61)$$

In general, λ_t can be a function of time. This is known as an inhomogeneous Poisson point process in time.

To solve for the correlation of the excitation function, the correlations of the shape functions must be found. Before any assumptions are made, it is useful to describe the random shape functions as deterministic three-dimensional pulse functions that are functions of a finite number of random parameters:

$$\begin{aligned} h(\mathbf{r} - \mathbf{a}) &= \hat{h}(\mathbf{c}, \mathbf{r} - \mathbf{a}) , \\ g(\mathbf{r} - \mathbf{b}) &= \hat{g}(\mathbf{d}, \mathbf{r} - \mathbf{a}) . \end{aligned} \quad (5.62)$$

The randomness in the source and sink functions (g and h) is now represented by the random variables \mathbf{c} and \mathbf{d} . In general, \mathbf{c} and \mathbf{d} can be random vectors of a finite number of random variables each. The deterministic functions \hat{g} and \hat{h} now represent the nonrandom characteristic shape of the source and sink events.

In general, the magnitudes of the shape functions are not independent of the parameters that define the randomness in the shape function. For example, the variable \mathbf{c} may represent the random radius of the sink function \hat{h} . The magnitude of the sink event (q) could also be a function of the random radius - a larger volume of sediment affected will result in a larger amount of mass that is transported. If this is the case, the joint probability density function for q and \mathbf{c} must be specified to find the correlation of the sink event.

However, if the magnitudes of the source/sink events are assumed to be independent of the shape functions, the correlations can be simplified as

$$\begin{aligned} \langle qg \rangle &= \langle q \rangle \langle \hat{g}(\mathbf{d}, \mathbf{r} - \mathbf{b}) \rangle , \\ \langle q^2 gg \rangle &= \langle q^2 \rangle \langle \hat{g}(\mathbf{d}, \mathbf{r}_1 - \mathbf{b}) \hat{g}(\mathbf{d}, \mathbf{r}_2 - \mathbf{b}) \rangle . \end{aligned} \quad (5.63)$$

The correlation function can then be described in terms of the correlations of the shape functions only:

$$R_{ff}(\mathbf{r}_1, \mathbf{r}_2, \tau) = \lambda_t \sigma_q^2 [R_{gg}(\mathbf{r}_1, \mathbf{r}_2) + R_{hh}(\mathbf{r}_1, \mathbf{r}_2)] \delta(\tau) + \lambda_t^2 \eta_q^2 [\langle g \rangle - \langle h \rangle]^2 , \quad (5.64)$$

where σ_q^2 is the variance of the event magnitudes and η_q is the mean. The shape

function correlations are defined as

$$\begin{aligned} R_{gg}(\mathbf{r}_1, \mathbf{r}_2) &= \langle \hat{g}(\mathbf{d}, \mathbf{r}_1 - \mathbf{b}) \hat{g}(\mathbf{d}, \mathbf{r}_2 - \mathbf{b}) \rangle, \\ R_{hh}(\mathbf{r}_1, \mathbf{r}_2) &= \langle \hat{h}(\mathbf{c}, \mathbf{r}_1 - \mathbf{a}) \hat{h}(\mathbf{c}, \mathbf{r}_2 - \mathbf{a}) \rangle. \end{aligned} \quad (5.65)$$

The covariance of the excitation function is defined as

$$C_{ff}(\mathbf{r}_1, \mathbf{r}_2) = R_{ff}(\mathbf{r}_1, \mathbf{r}_2) - \langle f(\mathbf{r}, t) \rangle^2. \quad (5.66)$$

It can be easily shown that the second term in (5.64) is equal to the second term in (5.66). Therefore, the covariance of the excitation is

$$C_{ff}(\mathbf{r}_1, \mathbf{r}_2, \tau) = \lambda_t \sigma_q^2 [R_{gg}(\mathbf{r}_1, \mathbf{r}_2) + R_{hh}(\mathbf{r}_1, \mathbf{r}_2)] \delta(\tau). \quad (5.67)$$

5.3.3 Stationarity in Space

Up to this point, the only assumptions made about the statistics of the shape functions in space are that the source/sink events are independent and identically distributed. The pdfs of the random variables that define the shape functions are still general. The correlations of the shape functions could have arbitrary structure that models the nonstationary behavior of complicated systems of organisms. Variability in the horizontal dimension due to the clustering of organisms could be modeled as a random process with stationary increments, for example. The depth dependence of bioturbation could be modeled by distributing the depth of the source/sink events nonuniformly, concentrating activity near the sediment-water interface. The pdf of the random position variables \mathbf{a} and \mathbf{b} may also be joint and/or conditional upon each other. In general, some form of non-stationarity in the depth direction is expected, unless the distribution of source/sink events is uniform in depth. Uniformity in depth is unlikely and is a very restrictive assumption.

This inherent non-stationarity presents an apparent paradox in relating a model for bioturbation to the acoustic model of Chapter 2. Somehow, the spectrum of the bioturbational process must be found, and a spectrum is only defined in terms

of a stationary process. Alternatively, the acoustic correlation could be found by integrating the sediment correlation directly. However, this complicates the inverse process of inferring biological parameters and forfeits the physical insight that can be gained by working with spectra.

This apparent paradox in modeling can be resolved by introducing a locally stationary process. This leads to the concept of a local spectrum that can vary in space. The simplest form of a local spectrum is found by assuming the positions of the source/sink events are independent and uniformly distributed with a Poisson density that is a function of position in space. The shape function correlations can then be defined in terms of the difference coordinate $\mathbf{r}_d = \mathbf{r}_1 - \mathbf{r}_2$, such that

$$\begin{aligned} R_{hh}(\mathbf{r}_d) &= \iint \lambda_a(\mathbf{a}) \hat{h}(\mathbf{c}, \mathbf{r} - \mathbf{a}) \hat{h}(\mathbf{c}, \mathbf{r} - \mathbf{r}_d - \mathbf{a}) p_c(\mathbf{c}) d\mathbf{c} d\mathbf{a} \\ &= \iint \lambda_a(\mathbf{r} - \boldsymbol{\alpha}) \hat{h}(\mathbf{c}, \boldsymbol{\alpha}) \hat{h}(\mathbf{c}, \boldsymbol{\alpha} - \mathbf{r}_d) p_c(\mathbf{c}) d\mathbf{c} d\boldsymbol{\alpha}, \end{aligned} \quad (5.68)$$

where $p_c(\mathbf{c})$ is the pdf of the random variable \mathbf{c} , $\mathbf{r} = \mathbf{r}_1$, and the change of variable $\boldsymbol{\alpha} = \mathbf{r} - \mathbf{a}$ is made. The parameter λ_a is the nonhomogeneous Poisson density in space. If λ_a varies slowly over the integral on $\boldsymbol{\alpha}$, compared to the shape function h , the Poisson parameter can be moved outside of the integral:

$$R_{hh}(\mathbf{r}_d) = \lambda_a(\mathbf{r}) \iint \hat{h}(\mathbf{c}, \boldsymbol{\alpha}) \hat{h}(\mathbf{c}, \boldsymbol{\alpha} - \mathbf{r}_d) p_c(\mathbf{c}) d\mathbf{c} d\boldsymbol{\alpha}. \quad (5.69)$$

Similarly for the correlation function R_{gg} :

$$R_{gg}(\mathbf{r}_d) = \lambda_b(\mathbf{r}) \iint \hat{g}(\mathbf{d}, \boldsymbol{\alpha}) \hat{g}(\mathbf{d}, \boldsymbol{\alpha} - \mathbf{r}_d) p_d(\mathbf{d}) d\mathbf{d} d\boldsymbol{\alpha}. \quad (5.70)$$

The excitation correlation is now simplified as a position-dependent, locally stationary process,

$$C_{ff}(\mathbf{r}_d, \mathbf{r}, \tau) = \sigma_q^2 [\lambda_b(\mathbf{r}) \hat{R}_{gg}(\mathbf{r}_d) + \lambda_a(\mathbf{r}) \hat{R}_{hh}(\mathbf{r}_d)] \delta(\tau), \quad (5.71)$$

where

$$\hat{R}_{gg}(\mathbf{r}_d) = \iint \hat{g}(\mathbf{d}, \boldsymbol{\alpha}) \hat{g}(\mathbf{d}, \boldsymbol{\alpha} - \mathbf{r}_d) p_d(\mathbf{d}) d\mathbf{d} d\boldsymbol{\alpha} \quad (5.72)$$

and

$$\hat{R}_{hh}(\mathbf{r}_d) = \iint \hat{h}(\mathbf{c}, \alpha) \hat{h}(\mathbf{c}, \alpha - \mathbf{r}_d) p_c(\mathbf{c}) d\mathbf{c} d\alpha . \quad (5.73)$$

The Poisson parameter in time has been absorbed into λ_a and λ_b , which are redefined as the number of source events (N_b) or the number of sink events (N_a) per unit time and unit volume:

$$\lambda_a = \frac{N_a}{TV} \quad \text{and} \quad \lambda_b = \frac{N_b}{TV} . \quad (5.74)$$

5.4 Spectrum of a Biodiffusional Process

Equation (5.31) is a deterministic differential equation with a random excitation f due to the nonlocal exchange of sediment. The solution ρ can be interpreted as the output of a linear system with a stochastic input:

$$\rho(\mathbf{r}, t) = L_d [f(\mathbf{r}, t)] . \quad (5.75)$$

The operator L_d is the integral equation (5.36) containing the diffusion Green's function. If the half-space effects are neglected, and the diffusion process is linear and space- and time-invariant, ρ can be expressed as a space-time convolution with the system impulse response,

$$\rho(\mathbf{r}, t) = g_d(\mathbf{r}, t) \otimes f(\mathbf{r}, t) , \quad (5.76)$$

where

$$g_d(\mathbf{r}, t) = L_d [\delta(\mathbf{r})\delta(t)] . \quad (5.77)$$

It follows from the linearity of the expected value that the correlation of the output is found in terms of the correlation of the input process:

$$R_{\rho\rho}(\mathbf{r}_d, \tau) = R_{ff}(\mathbf{r}_d, \tau) \otimes g_d(\mathbf{r}_d, \tau) \otimes g_d(-\mathbf{r}_d, -\tau) . \quad (5.78)$$

Thus, the mixing process can be characterized as a linear filtering process where the spectrum of the output process ($S_{\rho\rho}$) is defined completely in terms of the spectrum of the input (S_{ff}) and the frequency response of the diffusive system (G_d):

$$S_{\rho\rho}(\mathbf{k}, \omega) = |G_d(\mathbf{k}, \omega)|^2 S_{ff}(\mathbf{k}, \omega) . \quad (5.79)$$

The function G_d is the space-time Fourier transform of g_d . The spectrum of the input is found by taking the Fourier transform of the locally stationary covariance function (5.71) with respect to \mathbf{r}_d and τ ,

$$S_{ff}(\mathbf{k}, \mathbf{r}) = \frac{\sigma_q^2}{2\pi} [\lambda_b(\mathbf{r})S_{gg}(\mathbf{k}) + \lambda_a(\mathbf{r})S_{hh}(\mathbf{k})] , \quad (5.80)$$

where

$$S_{hh}(\mathbf{k}) = (2\pi)^3 \langle |H(\mathbf{k})|^2 \rangle \quad (5.81)$$

and

$$S_{gg}(\mathbf{k}) = (2\pi)^3 \langle |G(\mathbf{k})|^2 \rangle \quad (5.82)$$

are the spectra of the shape functions, and G and H are the Fourier transforms of the shape functions, \hat{g} and \hat{h} . The angle brackets in (5.81) and (5.82) are now the expected value operators with respect to the random variables \mathbf{c} and \mathbf{d} only. Note that the spectrum is independent of temporal frequency, ω , because of the assumed impulsive nature of the source and sink events.

For the case of a depth-independent and isotropic diffusion coefficient and neglecting the half-space, the diffusion Green's function is

$$G_d(k, \omega) = \frac{1}{Dk^2 - i\omega} , \quad (5.83)$$

where $k^2 = k_x^2 + k_y^2 + k_z^2$. The spectrum $S_{\rho\rho}$ is then expressed as

$$S_{\rho\rho}(\mathbf{k}, \mathbf{r}, \omega) = \frac{S_{ff}(\mathbf{k}, \mathbf{r})}{D^2 k^4 + \omega^2} . \quad (5.84)$$

Performing an inverse Fourier transform in time, the temporal and spatial spectrum of density fluctuations in the sediment can be modeled as

$$S_{\rho\rho}(\mathbf{k}, \mathbf{r}, \tau) = \frac{S_{ff}(\mathbf{k}, \mathbf{r})}{2Dk^2} e^{-Dk^2|\tau|}. \quad (5.85)$$

5.5 *Inhomogeneous Biodiffusion of Sediment Microtopography*

Epifaunal and infaunal activity create time varying roughness at the sediment-water interface on spatial and temporal scales that are of interest in acoustic scattering. Mega- and macrofaunal locomotion along the interface create surficial traces. Topographical trace concentration has been considered as an indicator of abundance of epifauna [84]. Infauna, such as deposit feeders, also create and destroy microtopography as sediment is transported to and from the sediment interface, creating mounds and depressions on the surface.

While larger organisms create roughness, other processes act to erase their effects. Physical processes, such as gravity and fluid flow due to wave action or currents, will transport surface sediment particles and erase traces of larger animals. Meiofaunal activity (analogous to the activity on similar scales within the sediment) creates random and continuous local exchange at the surface acting to erase or smooth larger-scale roughness features.

Analogous to the two-scale mixing of sediment volume inhomogeneities, as detailed in Section 5.3, the temporal and spatial properties of surface roughness, due to reworking by benthic organisms, can also be modeled as a forced diffusion process. The methods used to describe the correlation and spectral properties in terms of animal activity and spatial characteristics are applied directly to the surface roughness. The diffusive quantity is now the rough surface height (z_s), and local mixing by meiofauna (and other physical mechanisms) is described with a horizontal diffusion coefficient for roughness (D_s).

Equation (5.31) for two-scale mixing of sediment density inhomogeneities is then

rewritten to describe the temporal and spatial evolution of surface relief:

$$\frac{\partial}{\partial t} z_s(\mathbf{r}, t) - \nabla \cdot [D_s(\mathbf{r}, t) \nabla z_s(\mathbf{r}, t)] = f_s(\mathbf{r}, t). \quad (5.86)$$

The position vectors and derivatives are now in two dimensions $\mathbf{r} = (x, y)$. The nonlocal forcing function is described as

$$f_s(\mathbf{r}, t) = \sum_n q_n h_n(\mathbf{r} - \mathbf{a}_n) \delta(t - \xi_n). \quad (5.87)$$

The magnitude of each event is defined by the zero-mean quantity q_n in units of height. The shape function h_n is a dimensionless random function associated with the n th event that describes a random shape of a trace left behind by an animal or other surface relief event. The diffusion coefficient D_s describes the localized mixing in the horizontal direction at the surface of the sediment. In some cases, it may be the same as the horizontal component of the biodiffusion coefficient D_b used in Section 5.3. However, it may also include processes that only exist on the sediment-water interface, such as mixing due to bottom currents.

The correlation of the excitation function is found in the same manner as it was found in Section 5.3.2. However, now it is the covariance of f_s that is defined in terms of the correlation of the shape functions, the variance of the magnitudes of the events, and the Poisson density:

$$C_{ff}(\mathbf{r}_1, \mathbf{r}_2, \tau) = \lambda_s \sigma_s^2 R_{hh}(\mathbf{r}_1, \mathbf{r}_2) \delta(\tau). \quad (5.88)$$

The variance of the event magnitudes q_n is σ_s^2 . The Poisson density λ_s is the number of surficial traces per unit time.

The problems associated with stationarity in the depth direction, as in the volume problem, do not exist in the two-dimensional surface roughness problem. Stationarity in the horizontal directions is more easily justified (on spatial scales comparable with the sizes of the traces left by mega- and macrofauna, at least). Therefore, with λ_s defined as a slowly varying function of space compared with the trace shape

functions, the covariance of the excitation function can be modeled using Section 5.3.3, and the spectrum of the excitation modeled using Section 5.4, such that

$$S_{ff}(\mathbf{k}, \mathbf{r}) = \frac{\sigma_s^2}{2\pi} \lambda_s(\mathbf{r}) S_{hh}(\mathbf{k}). \quad (5.89)$$

The Poisson density λ_s is now the number of animal trace events per unit time per unit surface area, and S_{hh} is the spectrum of the trace shape functions defined analogously to (5.81). The surface roughness spectrum of a biodiffusive process at the sediment-water interface is then

$$S_{zz}(\mathbf{k}, \mathbf{r}, \omega) = \frac{S_{ff}(\mathbf{k}, \mathbf{r})}{D_s^2 k^4 + \omega^2}. \quad (5.90)$$

The temporal and spatial spectrum of surface roughness due to biological mixing is

$$S_{zz}(\mathbf{k}, \mathbf{r}, \tau) = \frac{S_{ff}(\mathbf{k}, \mathbf{r})}{2D_s k^2} e^{-D_s k^2 |\tau|}. \quad (5.91)$$

5.6 Summary and Conclusions

The above expressions are general in the sense that they attempt to model bioturbation in nonspecific terms (e.g., diffusion and point density) while still accounting for the two-scale nature of the mixing process (meiofauna and macrofauna) and non-stationarity. The shape functions and their expected values should reflect the size and shape of the macrofauna that move sediment nonlocally. Anisotropy can be modeled, for example, by using a shape function that represents directional feeding, such as vertical burrows made by conveyer-belt feeders [40, 7]. Spatial dependence of the source/sink events is modeled as a nonhomogeneous Poisson process in space and time. The preference of a deposit feeder to remove sediment from a specific depth, for example, could be modeled by specifying a non-uniform Poisson density function that increases the probability of an event occurring at the favored depth.

The Poisson point density in time should reflect the amount and rate of macrofaunal activity, which in general can be time dependent. The diffusion coefficient

should reflect the length and time scales of the meiofaunal activity, which can also be modeled as depth dependent. Of course, in some circumstances the Poisson assumption (homogeneous or nonhomogeneous) cannot be justified. This may occur if the gradient in the Poisson parameter cannot be assumed constant over the geometric extent of the shape function. For example, deposit feeders with long body lengths can extend deep into the sediment. In this case, equation (5.67) must be solved directly, as opposed to using (5.71). The possibility of describing mixing as a stationarity process may be abandoned altogether. This would bring in question the use of spectral analysis for describing sediment physical properties. Correlation descriptions would still be valid, however, using (5.67).

Chapter 6

REMOTE SENSING OF BENTHIC ACTIVITY

Remote sensing of benthic biology by acoustic wave scattering is potentially an important tool for studying biological processes on spatial and temporal scales larger than can be achieved by current point sampling methods. Inferences about the effect of benthic biota on sediment structure are typically made by examining sparsely sampled sediment cores and optical imagery. Coring can provide detailed information on the vertical structure of the sediment at an instant in time and for a single horizontal location. However, large gaps are generally left in horizontal and temporal sampling. High resolution X-radiographs [28], X-ray tomography [52], microelectric conductivity methods [74], and box coring provide better horizontal resolution, but they are usually limited to very small spatial scales (less than a meter). They are also destructive, providing only a single measurement in time. Nondestructive in situ methods, such as acoustic tomography in the sediment [74, 87] and very high-frequency acoustic (ultra-sound) imaging [51], can provide increased temporal resolution with minimal impact on the sediment. However, they are also limited to small spatial scales due to high acoustic attenuation in the medium. Optical methods, such as stereo photography [64, 70], only provide information about the sediment interface, and are again limited in their larger-scale spatial resolution.

This chapter will discuss a stochastic model-based technique for monitoring biological activity on large spatial and temporal scales using high-frequency acoustic backscatter. The method is stochastic because it relies on the random nature of biological mixing to create the scattering medium. In this sense it is similar to previous statistical methods of monitoring benthic activity using backscatter [41]. The

method differs in its reliance on physical models of scattering and sediment mixing.

The chapter will begin with the development of a forward model of scattering due to bioturbation using the results of chapters 2 and 5. Then the inverse problem will be investigated where an estimate of the temporal correlation of backscatter is used to infer parameters of biological mixing in the sediment. Finally, the models will be applied to experimental data as a preliminary test of the modeling methodology. The experiment was performed in the West Sound of Orcas Island in Puget Sound. Backscatter data was recorded in an area with observed biological activity. Ground truth estimates of biological activity are compared with the acoustically inferred activity.

6.1 Forward Model of Scattering

A model for the effects of bioturbation on volume scattering is developed by relating the decorrelation in time of the backscattered field with changes in the sediment physical properties due to biological mixing. The perturbation method of Section 2.4 is used to describe scattering as a function of the statistical properties of the sediment. The sediment bioturbation model of Chapter 5 is used as the spectral model of sediment mixing. They are combined to form a forward stochastic model of scattering due to benthic biological activity.

Consider backscatter of an acoustic field due to volume scattering in sediment. For backscatter at grazing angle θ , equations (2.74) and (2.56) are rewritten as

$$C_{pp}(\theta, \tau) = 8\pi^3 |\Gamma(\theta)|^2 |\bar{k}|^4 (\mu + 1)^2 \tilde{S}_{\rho\rho}(k_d, \tau), \quad (6.1)$$

where

$$\Gamma(\theta) = \frac{\rho_0 T^2(\theta)}{\rho (4\pi r)^2} e^{i2k_0 r}, \quad (6.2)$$

and $k_d = (\text{Re}[\bar{k}]/2) \sin \theta$ is the Bragg wavenumber. Recall that $\tilde{S}_{\rho\rho}(k_d, \tau)$ is the time-dependent, half-space spectrum of density fluctuation in the sediment defined

using (2.75) as

$$\tilde{S}_{\rho\rho}(\mathbf{k}_d, \tau) = \int_{hs} d\mathbf{r}_c \int_{-\infty}^{\infty} dk'_{dz} S_{\rho\rho}(k_{dx}, k_{dy}, k'_{dz}, \mathbf{r}_c, \tau) W(k'_{dz} - k_{dz}, z_c) e^{-2\alpha z_c}, \quad (6.3)$$

where

$$W(k_z, z_c) = \frac{\sin(2k_z z_c)}{\pi k_z}. \quad (6.4)$$

The function $S_{\rho\rho}(\mathbf{k}_d, \mathbf{r}_c, \tau)$ is the time and space dependent spectrum of density fluctuations in the sediment evaluated at the Bragg wavenumber. The normalized correlation coefficient for scattering is defined as

$$c_{pp}(\tau) = \frac{C_{pp}(\theta, \tau)}{C_{pp}(\theta, 0)} = \frac{\tilde{S}_{\rho\rho}(k_d, \tau)}{\tilde{S}_{\rho\rho}(k_d, 0)}. \quad (6.5)$$

In Section 5.4 a model for the spectrum of density fluctuations due to biological mixing was presented, see equations (5.85) and (5.80). Mixing is modeled as a locally stationary and time-dependent diffusion process having the spectrum

$$S_{\rho\rho}(\mathbf{k}, \mathbf{r}, \tau) = \frac{S_{ff}(\mathbf{k}, \mathbf{r})}{2Dk^2} e^{-Dk^2|\tau|}, \quad (6.6)$$

where the spectrum of the random biological forcing is

$$S_{ff}(\mathbf{k}, \mathbf{r}) = 4\pi^2 \sigma_q^2 [\lambda_b(\mathbf{r}) \langle |G(\mathbf{k})|^2 \rangle + \lambda_a(\mathbf{r}) \langle |H(\mathbf{k})|^2 \rangle]. \quad (6.7)$$

Equations (6.1-6.7) form the basis of the forward and inverse models of scattering due to biological activity. The model parameters include: the biodiffusion coefficient D ; the spectra of the macrofaunal shape functions h and g ; and the nonhomogeneous Poisson point density functions λ_a and λ_b . The observable is the estimate of the correlation function (6.1).

Using (6.1), the correlation of the scattered field is a function of lag time and grazing angle. As the lag time increases, the correlation is expected to decrease exponentially with a time constant that is predicted by the time-dependent biodiffusive spectrum of density fluctuations using (6.6). Therefore, the time dependence of the field correlation is due to the time dependence of the diffusion process.

The grazing angle dependence of the backscatter correlation is due to the scattering geometry. At low grazing angles, the incident field will penetrate a short distance into the sediment. Therefore, the scattered field at low grazing angles will be influenced primarily by the sediment near the sediment-water interface. At higher grazing angles, the incident field will penetrate deeper into the sediment, and the scattered field will be affected by deeper sediment, as well as the interface sediment. If the sediment mixing processes are depth dependent, the grazing angle dependence of the scattered field correlation should reveal this structure. A concentration of biological activity near the sediment-water interface (decreasing with depth) will cause the scattered field at lower grazing angles to decorrelate faster than at higher grazing angles.

6.2 Inverse Model of Scattering

Using the forward model of (6.1) through (6.7), predictions of backscatter correlation can be made using information about the parameters that define biological mixing. If the stochastic geometry, behavior, and rate of activity of an organism are well understood, its effect on the scattered field over time can be modeled. In contrast, the remote sensing problem is the estimation of these stochastic biological parameters from the observation of the decorrelation of acoustic backscatter.

6.2.1 Estimation of Backscatter Correlation

To use the backscattered field as a tool for observing changes in the sediment, the inverse problem must begin by estimating the temporal correlation function (6.1) using acoustic data. One means of doing this is to use the time-domain scattered field to form an estimate of the ensemble average. To start, a finite duration pulse is transmitted at time t_0 , and the time-domain scattered field is digitized and time-gated to correspond to scattering from an isolated and finite region of the seafloor.

An estimate of the backscatter correlation can be found by correlating the time-domain scattered field from a volume of sediment the size of the ensonified volume. If the ensonified volume is large compared to the correlation length of the medium, the time-domain correlation will be an estimate of the correlation function (2.74) (see Section 2.6).

A pulse is transmitted, and the received signal $p_s(t)$ is digitized as

$$p_s(t_n) = \text{Re} [u_s(t_n)e^{-i\omega_0 t_n}] , \quad (6.8)$$

with

$$u_s(t_n) = A_s(t_n)e^{i\phi_s(t_n)} . \quad (6.9)$$

The discretized variable t_n is the time after transmission of the pulse for a single scan. The backscattered signal from each range bin is then cross-correlated with the signal from the same range bin, but from a scan at some later time τ :

$$\hat{C}_{pp}(\tau) = \sum_{n=M}^{M+N-1} u_s(t_n)u_s^*(t_n + \tau) . \quad (6.10)$$

The signal $u_s(t_n)$ is from the scan chosen as a reference, and $u_s(t_n + \tau)$ is from a scan at time τ later. The limits of the summation (M and N) are the start and end sample numbers for the range bin of interest.

The correlation estimate is a measure of the total change in the scattered field between scans, including changes in the propagation path between the transducer and the seafloor. To be assured that any decorrelation observed in the scattered field is due to changes in the seafloor only, propagation effects must be removed. The most likely source of decorrelation introduced by the propagation path is sound speed changes in the water. Uncorrelated ambient noise and volume reverberation from the water due to suspended matter and organisms [41], for example, are other sources of signal decorrelation.

The speed of sound in the ocean water will fluctuate with changes in the water temperature. Neglecting the scattering from temperature microstructure in the water, changes in the average water temperature between scans of the seafloor will introduce a phase and amplitude shift into the scattered field, as compared with the reference field [20]. Before cross-correlating the scattered fields from different scans, the sound speed fluctuations due to water temperature changes (δc) must be removed. The temperature compensated cross-correlation between scans, derived previously in [20], can be written as

$$\hat{C}_{pp}(\tau) = \sum_{n=M}^{M+N-1} u_s(t_n) u_s^*(t_n + \tau) e^{i\omega_0 \frac{\delta c}{c} t_n} . \quad (6.11)$$

This approximation compensates for the shift in the carrier (at frequency ω_0), but neglects the changes in the complex envelope of the scattered field.

6.2.2 Models of Biological Activity

The mixing model of (6.6) is very general. With no *a priori* information about the statistical description of the organisms in a sediment to constrain the spatial and temporal parameters of the bioturbation model, the remote sensing problem may be ill-posed. It is likely that the spectrum of the shape functions will provide the most ambiguity in the model inversion, as the types of shape functions (that reflect the types of organisms) and their spatial distributions provide the most unconstrained degrees of freedom in the model. It is unrealistic to expect a unique inversion without some prior knowledge of their form. In general, some knowledge of the biology must be applied to the inverse problem.

A formal analysis of the stability of the inversion will not be performed. However, several assumptions about the sediment source/sink functions are made to simplify the sediment mixing model, and to improve the uniqueness of the inversion. First, the biodiffusion coefficient is assumed to be uniform in the horizontal directions and

exponentially decaying in depth:

$$D(z) = D_0 e^{-|z|/L} . \quad (6.12)$$

This form assumes that diffusive activity decreases with depth at a rate defined by the meiofauna rework depth L , with meiofaunal activity concentrated near the surface. It also seems reasonable to assume the same form for the spatial point density (the Poisson parameters λ_a and λ_b):

$$\lambda_a(\mathbf{r}) = \lambda_0 e^{-|z|/L_\lambda} . \quad (6.13)$$

The activity is assumed to decrease with depth at a rate defined by the macrofauna rework depth L_λ . For simplicity, it is assumed that the macrofaunal and meiofaunal rework depths are equal ($L_\lambda = L$), and the rate parameters for the positions of the source/sink functions are assumed to be identical ($\lambda_a = \lambda_b$).

The diffusion coefficient and the distribution of source/sink events are assumed to be uniform in the horizontal directions. In general, this assumption does not seem realistic. However, it may be reasonable if enough horizontal averaging is performed in the measurements.

The shape functions to be used will be random spherical source and sink functions, having the Fourier transform

$$H(\mathbf{k}) = G(\mathbf{k}) = \frac{1}{2\pi^2 k^3} (\sin ak - ak \cos ak) . \quad (6.14)$$

The radius a is assumed to be a Gaussian random variable with normal distribution $N(\eta_a; \sigma_a)$. Using equations (6.12-6.14) and the above assumptions, the spectrum of the locally stationary and time-dependent biodiffusion process (6.6) is rewritten as

$$S_{\rho\rho}(\mathbf{k}, \mathbf{r}, \tau) = 4\pi^2 \frac{\sigma_a^2 \lambda_0}{D_0} \frac{\langle |H(\mathbf{k})|^2 \rangle}{k^2} e^{-D(z)k^2|\tau|} . \quad (6.15)$$

The expected value integral in (6.15) must be performed numerically. Figure 6.1 illustrates an exponentially decreasing distribution of spherical source/sink functions with random radii.

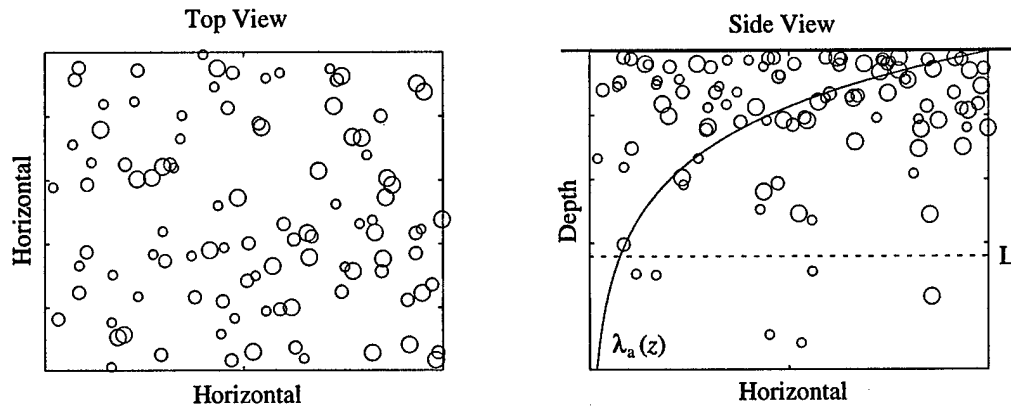


Figure 6.1: Spherical shape functions that are: (a) homogeneously distributed in the horizontal; and (b) nonhomogeneously distributed in depth. The Poisson point density in space and time decreases exponentially with depth with a scale defined by the rework depth L , concentrating activity near the sediment-water interface.

The model now consists of the normalized correlation coefficient (6.5) as the observable and the biodiffusive spectrum (6.15) as the forward model. The object is to minimize the difference between the model predicted backscatter correlation and the data as a function of grazing angle and lag time. By using the normalized correlation, the magnitude of (6.15) is removed from the model as an unknown. The inverse problem is reduced to the solution of four unknowns: 1) the mean radius η_a of the spherical source/sink shape functions; 2) the variance σ_a^2 of the radius; 3) the biodiffusion coefficient D_0 ; and 4) the rework depth L .

6.3 Orcas Island Experiment

Model predictions are compared with data collected during an acoustic experiment performed in a shallow water bay of Orcas Island in Puget Sound in Washington state. Acoustic backscatter was recorded over an area of seafloor by a bottom mounted transducer configured as illustrated in Figure 6.2. The acoustic system has been described in detail elsewhere [20, 41], and only a brief description is given here.

A calibrated 40 kHz monostatic transducer with a fan-shaped beam pattern was used to scan a circular site approximately 50 meters in radius at azimuthal increments of 5° . A single pulse of duration $T_0 = 2$ ms was transmitted for each azimuthal direction, and backscatter was recorded to produce a single radial scan. The pulse has a rectangular envelope, and it was frequency modulated to cover a bandwidth of 2 kHz. The transducer was then rotated to the next azimuthal increment and another pulse transmitted. The transmission and recording of backscatter is repeated to complete a circular scan in approximately 7 minutes. A complete scan was recorded at 2.4 hour intervals through the duration of the experiment. The instrument remained at a fixed location for approximately 60 days.

A total of 585 circular scans was recorded to provide a series of backscatter images that reveal temporal and spatial variability in scattering from the sediment. Figure 6.3 illustrates the spatial variability of backscatter. The circular images show the mean and variance of backscatter estimated from 50 complete scans (over 5 days). The mean shows large spatial variation in backscatter strength (> 3 dB). The small patches of high backscatter in the fourth quadrant of the circle are due to targets and manipulations made during the experiment. The second and third quadrants were undisturbed. The small scale spatial variations in backscatter (~ 1 -2 meter scale) are likely due to the expected statistical variations in the signal (of ~ 5 dB). The low variance of the backscatter strength (~ -80 dB) suggests that the variability in the mean backscatter strength is due to the sediment properties, rather than caused by transients such as reverberation from organisms in the water or uncorrelated noise. For both plots in Figure 6.3, the Lambert law angular dependence of backscattering ($\sin^2 \theta$) is removed. Both the mean and the variance of the scattering strength were calculated by forming the ensemble average of the scattering cross-section and then converting to dB using $10 \log_{10}$.

The sediment in the area is a silty-clay with moderate biological activity. No bubbles were observed in the sediment, and an extensive set of sediment physi-

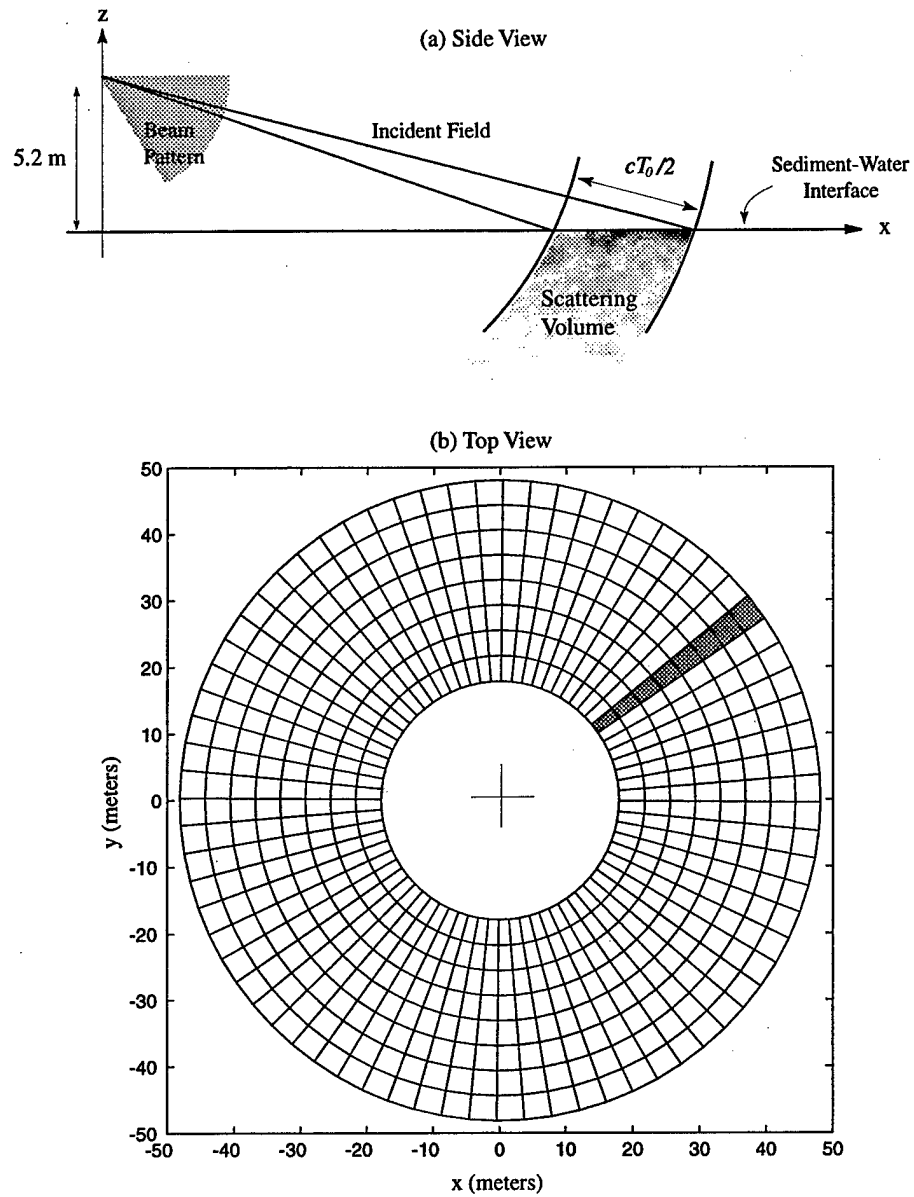


Figure 6.2: Scattering geometry of Orcas experiment. The shaded area is a radial scan for a single pulse transmission.

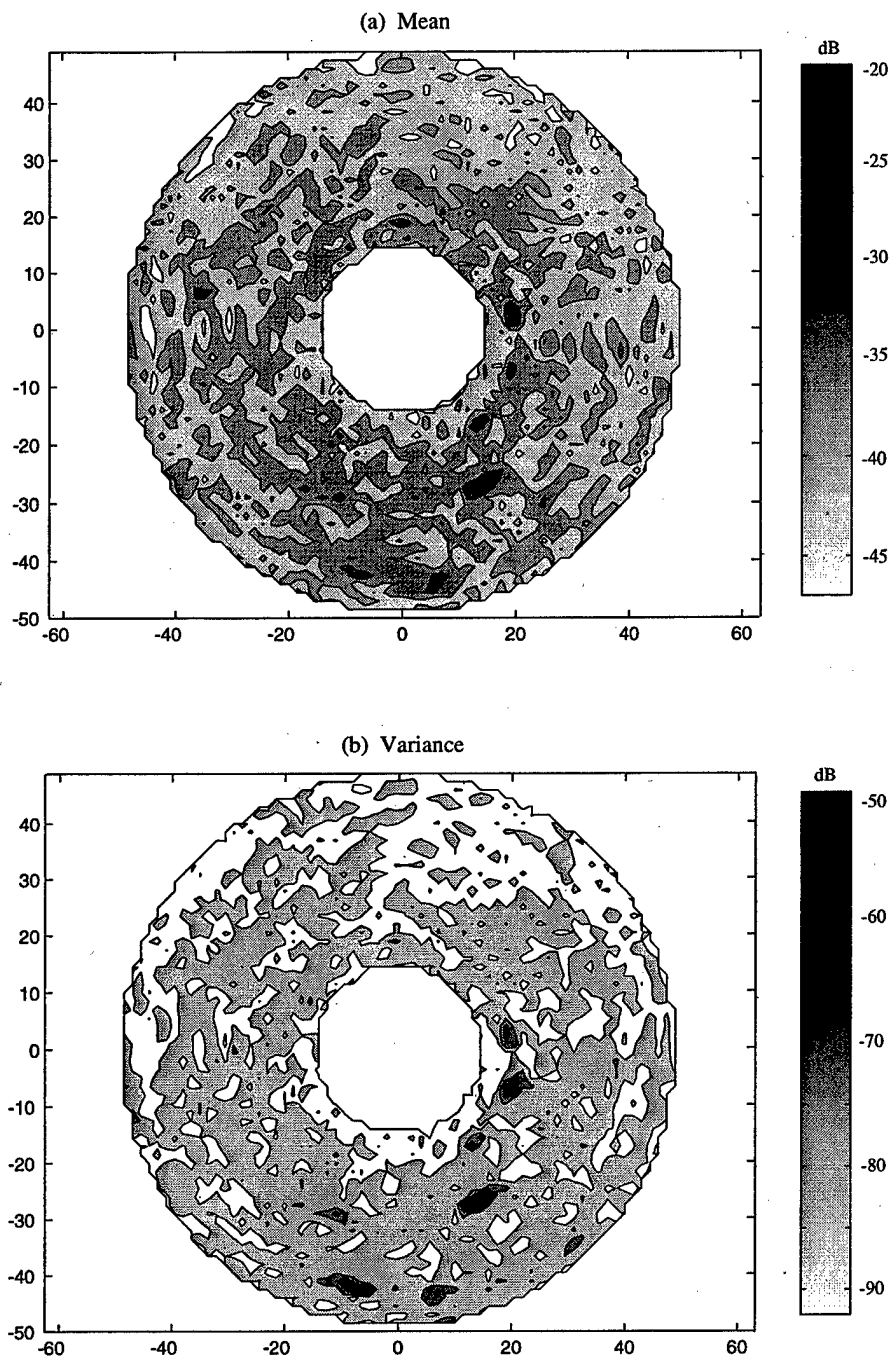


Figure 6.3: Spatial variability in (a) the mean backscatter strength, and (b) the variance of the backscatter strength at the Orcas site. Data estimated from 50 consecutive scans using 40 kHz backscatter, and plotted on a uniform grid with 1.5 meter spacing.

cal properties was measured at the site by investigators of the US Naval Research Laboratory (NRL). This work included core and in-situ measurement of geoacoustic parameters, X-radiography of sediment inhomogeneity, and stereo-photographic measurement of sea floor roughness. The biodiffusion of natural radio-isotope tracers was also analyzed, and an estimate of the vertical biodiffusion coefficient was obtained in the same location as the acoustic data [82].

6.3.1 *Sediment Physical Properties*

The spectra of core density fluctuations were estimated using a first-order autoregressive (AR) model (see Appendix C). This model assumes that the autocorrelation of the normalized fluctuations can be expressed as

$$\hat{C}_{\rho\rho}(\mathbf{r}) = \sigma_{\rho}^2 e^{-\ln \hat{a} |z| / \delta z}, \quad (6.16)$$

where \hat{a} is the first-order AR coefficient estimated from the core data using the Levinson-Durbin algorithm [59]. Since γ_{ρ} is a zero-mean process, the zero-lag autocorrelation is its variance, σ_{ρ}^2 . The isotropic power law PSD function for density fluctuations is found from (6.16) where the correlation length is defined as $l_c = -\delta z / \ln \hat{a}$, and δz is the core sampling interval. The spectral parameters for the Orcas cores are listed in Table 6.1 along with other geoacoustic parameters supplied by NRL. A core sampling interval of 2 cm was used providing marginal resolution compared to the acoustic wavelength. The core data are also one-dimensional, which necessitated an assumption of isotropy in the spectral estimates.

6.3.2 *Sediment Volume Scattering*

Backscatter strength per unit area of sea floor was measured as a function of grazing angle for the Orcas site. Owing to the similarity of the magnitude and angular dependence of the measured values compared to those of other sites having a range of different sediment types [33, 34, 48], the dominant scattering mechanism cannot

Density Ratio	ρ/ρ_0	1.406
Sound Velocity Ratio	\bar{c}/c_0	0.977
Proportionality Constant	μ	-0.934
Compressional Loss	δ	0.0019
Density Variance	σ_ρ^2	0.002
Correlation Length	l_c	3.198 (cm)

Table 6.1: Sediment parameters estimated from cores and model-data comparison for the Orcas site [14].

be inferred from the backscatter alone. However, by using the sediment core measurements as inputs to scattering models, the model results can be compared with observed backscatter data, and the dominant scattering mechanism inferred.

Two scattering models are considered: scattering from volume heterogeneity and scattering from a rough sediment-water interface. Surface roughness scattering is treated using a first-order perturbation approximation [34] with roughness characterized by the two-dimensional, isotropic, power-law spectrum estimated from sites with similar sediments [33, 34]. As Figure 6.4 shows, the predicted interface scattering was sufficiently below the measured values that interface scattering effects can be neglected.

Figure 6.4 shows the predicted backscatter strengths found using the first-order volume model with and without half-space effects. In this case, a first-order approximation models the data reasonably well, and half-space effects are negligible over the angular range of the data. The difference between model predictions and data is most likely due to errors in the estimated heterogeneity spectra.

No significant oceanographic processes or sediment transport events were observed during the experiment. For the Orcas site, sound speed fluctuations were recorded for the duration of the experiment by conductivity, temperature, and depth

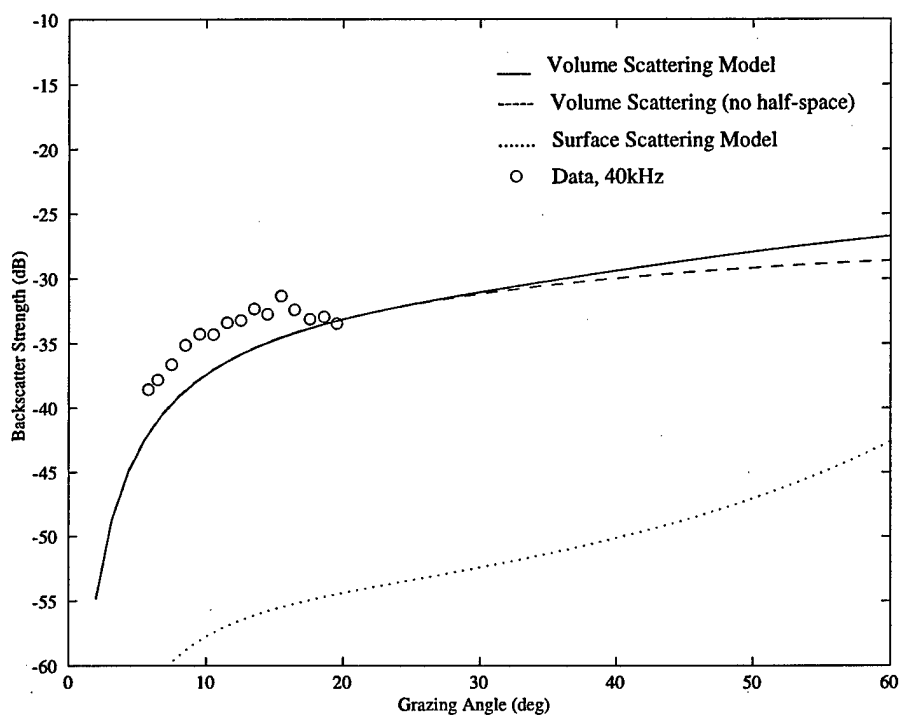


Figure 6.4: Comparison of measured backscatter with model predictions for the Orcas site.

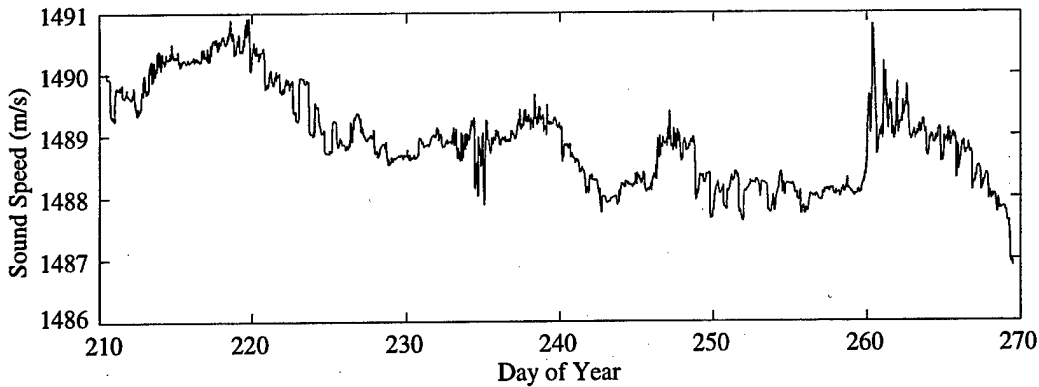


Figure 6.5: Sound speed fluctuations in the water during the Orcas experiment.

(CTD) measurements (see Figure 6.5). Given the nature of the sediment and the expected low level of roughness scattering, it is expected that acoustic penetration into the sediment and the effects of biological mixing are the dominant mechanisms for decorrelation.

6.3.3 Model-Data Comparison

The model for the temporal correlation of seafloor backscattering due to biodiffusive sediment mixing was compared with backscatter correlation estimated from the Orcas experiment. Figure 6.6 shows a comparison of the observed and predicted correlations as functions of lag time. The model was fitted to the data (plotted as points) by trial and error while constraining the parameters of the sediment model to realistic values. The offset of the observed correlation profile from the predicted profile is due to uncorrelated noise in the data. Reverberation in the water column that is uncorrelated from scan to scan is a likely source of noise.

Table 6.2 outlines the parameters estimated from the model-data comparison. The estimated biological parameters are typical for the type of sediment and environment encountered at the Orcas site. An estimate of the biodiffusion coefficient for naturally occurring radioisotopes (D_b) was measured from cores in the same

Diffusion Coefficient	D_0	2.4 ($cm^2/year$)
Macrofauna Rework Depth	L_λ	3.8 (cm)
Meiofauna Rework Depth	L	3.8 (cm)
Mean Radius	η_a	0.4 (cm)
Radius Standard Deviation	σ_a	0.14 (cm)

Table 6.2: Sediment parameters estimated from cores and model-data comparison for the Orcas site.

area as the acoustic experiment. The core analysis produced an estimate of $D_b \approx 8$ $cm^2/year$ [82]. This value is higher than the acoustically inferred value of $D_0 \approx 2.4$ $cm^2/year$. One explanation is that the value estimated from the cores is a different type of diffusion coefficient than the coefficient estimated using (6.12). The D found using the bioturbation model developed in this thesis is the meiofaunal diffusion coefficient. The D_b estimated from cores uses the classical diagenesis model of diffusive mixing, and therefore it includes both meiofaunal and macrofaunal mixing. In general, it would be expected that the meiofaunal diffusion coefficient is smaller than the total diffusion coefficient.

6.4 Summary and Conclusions

A biodiffusion model using random excitation to describe the time evolution of sediment inhomogeneities is combined with the first-order perturbation treatment of sediment volume backscatter. The first-order perturbation model for volume backscatter is validated for use at the Orcas site by data-model comparison. Half-space effects are shown to be unimportant at the low grazing angles used in the Orcas experiment. Sediment physical properties and inhomogeneity spectra were estimated using measured core data. Higher resolution two- or three-dimensional core analyses (e.g., X-radiographs, CT) are recommended for future work to improve the sediment

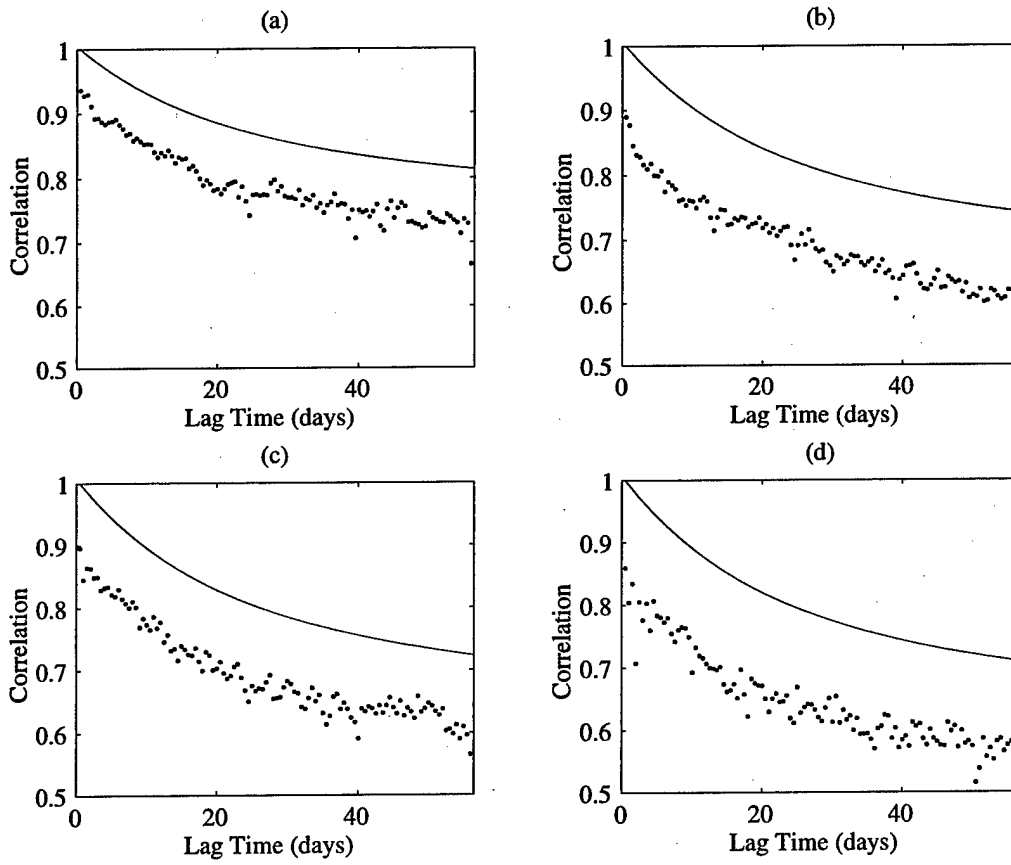


Figure 6.6: Comparison of measured backscatter correlation and model predictions, (a) $\theta = 14.7^\circ$, (b) $\theta = 9.4^\circ$, (c) $\theta = 7.6^\circ$, (d) $\theta = 6^\circ$

ground truth estimates.

Backscatter measured at the Orcas site was used to estimate the temporal correlation of the scattered field. The correlation estimate was then used to estimate benthic biological activity by comparison with the biodiffusive mixing model. Using the correlation data for the Orcas site, the proposed model of sediment mixing predicts sediment biodiffusion parameters that are realistic. Verifying the acoustically inferred biodiffusive parameters is problematic because there is no analogous sampling method that provides similar spatial and temporal resolution. This is the main reason acoustic remote sensing methods are interesting. Further model-data comparisons and better ground truth estimates of sediment physical and biological properties are needed to verify the methodology. However, this initial and simple application of the model to data provides encouraging results.

BIBLIOGRAPHY

- [1] R. C. Aller. *The Effects of Macrobenthos on Chemical Properties of Marine Sediment and Overlaying Water*, pages 53–103. Plenum Press, New York, 1982.
- [2] Uscinski B, L. *The Elements of Wave Propagation in Random Media*. McGraw-Hill, New York, NY, 1977.
- [3] D. H. Berman. Simulations of rough interface scattering. *J. Acoust. Soc. Am.*, 89(2):623–636, February 1991.
- [4] R. A. Berner. *Early Diagenesis - A Theoretical Approach*. Princeton University Press, Princeton, NJ, 1980.
- [5] P. Blondel and B. J. Murton. *Handbook of Seafloor Sonar Imagery*. Wiley-PRAXIS Series in Remote Sensing, Chichester, 1997.
- [6] B. P. Boudreau. Mathematics of tracer mixing in sediments: I. Spatially-dependent, diffusive mixing. *Am. J. Sci.*, 286:161–198, 1986.
- [7] B. P. Boudreau. Mathematics of tracer mixing in sediments: II. Nonlocal mixing and biological conveyor-belt phenomena. *Am. J. Sci.*, 286:199–238, 1986.
- [8] B. P. Boudreau. Mathematics of tracer mixing in sediments: III. The theory of nonlocal mixing within the sediment. *Am. J. Sci.*, 287:693–719, 1987.
- [9] B. P. Boudreau. *Diagenetic Models and Their Implementation*. Springer-Verlag, Berlin, 1997.

- [10] R. C. Bourret. Propagation in randomly perturbed fields. *Can. J. Phys.*, 40:782-790, 1962.
- [11] L. M. Brekhovskikh. *Waves in Layered Media*. Academic, San Diego, 1980.
- [12] L. M. Brekhovskikh and Yu. P. Lysanov. *Fundamentals of Ocean Acoustics*. Springer-Verlag, Berlin, 1991.
- [13] K. B. Briggs. High-frequency acoustic scattering from sediment interface and volume inhomogeneities. Technical Report NRL/FR/ 7431-94-9617, Naval Research Laboratory, December 1994.
- [14] K. B. Briggs. Personal correspondence. 1997.
- [15] S. L. Broschat and E. I. Thorsos. An investigation of the small slope approximation for scattering from rough surfaces: Part II. Numerical studies. *J. Acoust. Soc. Am.*, 101(5):2615-625, May 1987.
- [16] M. J. Buckingham. Theory of acoustic attenuation, dispersion, and pulse propagation in unconsolidated granular materials including marine sediments. *J. Acoust. Soc. Am.*, 102(5):2570-2596, November 1997.
- [17] S. Chandrasekhar. *Radiative Transfer*. Dover, New York, 1960.
- [18] W. C. Chew, C. C. Lu, and Y. M. Wang. Efficient computation of three-dimensional scattering of vector electromagnetic waves. *J. Opt. Soc. Am.*, 11(4):1528-1537, April 1994.
- [19] N. P. Chotiros. Biot model of sound propagation in water-saturated sand. *J. Acoust. Soc. Am.*, 97:199-214, January 1995.

- [20] J.G. Dworski and D. R. Jackson. Spatial and temporal variation of acoustic backscatter in the STRESS experiment. *J. Continental Shelf Res.*, 14:1221–1237, August 1994.
- [21] D. Farmer and S. Vagle. Waveguide propagation of ambient sound in the ocean surface bubble layer. *J. Acoust. Soc. Am.*, 86:1897–1908, 1989.
- [22] H. Gan and W. C. Chew. A discrete BCG-FFT algorithm for solving 3D inhomogeneous scattering problems. *J. Electromagnetic Waves and Appl.*, 9(10):1339–1357, 1995.
- [23] E. L. Hamilton. Geoacoustic models of the sea floor. *J. Acoust. Soc. Am.*, 68:1313–1336, 1980.
- [24] R. F. Harrington. *Field Computation by Moment Methods*. Macmillan Publishing Company, New York, 1968.
- [25] F. D. Hastings, J. B. Schneider; and S. L. Broschat. A finite-difference time-domain solution to scattering from a rough pressure-release surface. *J. Acoust. Soc. Am.*, 106(2):3394–3340, December 1997.
- [26] P. C. Hines. Theoretical model of in-plane scatter from a smooth sediment seabed. *J. Acoust. Soc. Am.*, 88(2):325–334, July 1990.
- [27] D. V. Holliday, R. E. Pieper, and G. S. Klepple. Bioacoustical oceanography at high frequencies. *ICES J. Mar. Sci.*, 52:279–298, 1995.
- [28] R. J. Holyer, D. K. Young, and J. C. Sandidge. Sediment density structure derived from textural analysis of cross-sectional X-radiographs. *Geo-Marine Letters*, 16:204–211, 1996.

- [29] A. Ishimaru. *Electromagnetic Wave Propagation, Radiation, and Scattering*. Prentice-Hall, New Jersey, 1991.
- [30] A. Ishimaru. *Wave Propagation and Scattering in Random Media*. IEEE Press and Oxford University Press, New York, 1997.
- [31] A. N. Ivakin. A unified approach to volume and roughness scattering. *J. Acoust. Soc. Am.*, 103(2):827-873, 1998.
- [32] A. N. Ivakin and Yu. P. Lysanov. Underwater sound scattering by volume inhomogeneities of a bottom medium bounded by a rough surface. *Sov. Phys. Acoust.*, 27, May 1981.
- [33] D. R. Jackson and K. B. Briggs. High-frequency bottom backscattering: Roughness versus sediment volume scattering. *J. Acoust. Soc. Am.*, 92:962-977, 1992.
- [34] D. R. Jackson, K. B. Briggs, K. Williams, and M. Richardson. Tests of models of high-frequency seafloor backscatter. *IEEE J. of Ocean. Engin.*, 21(4):458-470, 1996.
- [35] D. R. Jackson and A. N. Ivakin. Scattering from elastic sea beds: First-order theory. *J. Acoust. Soc. Am.*, 103:336-345, January 1998.
- [36] D. R. Jackson, K. L. Williams, and K. B. Briggs. High-frequency acoustic observations of benthic spatial and temporal variability. *Geo-Marine Letters*, 16:212-218, 1996.
- [37] D. R. Jackson, D. P. Winebrenner, and A. Ishimaru. Application of the composite roughness model to high-frequency bottom backscatter. *J. Acoust. Soc. Am.*, 95:2441-2451, May 1994.

- [38] F. B. Jenson, W. A. Kuperman, M. B. Porter, and H. Schmidt. *Computational Ocean Acoustics*. AIP Press, New York, 1993.
- [39] C. D. Jones and D. R. Jackson. Temporal fluctuation of backscattered field due to bioturbation in marine sediments. In *High Frequency Acoustics in Shallow Water*, pages 275–283, Lerici, Italy, 1997. NATO SACLENT Undersea Research Center.
- [40] P. A. Jumars. *Concepts in Biological Oceanography*. Oxford University Press, New York, 1993.
- [41] P. A. Jumars, D. R. Jackson, T. F. Gross, and C. Sherwood. Acoustic remote sensing of benthic activity: A statistical approach. *Limnol. Oceanogr.*, 41(6):1220–1241, 1996.
- [42] J. Kevorkian. *Partial Differential Equations, Analytical Solution Techniques*. Wadsworth and Brooks/Cole Mathematics Series, Pacific Grove, CA, 1990.
- [43] I. Kupiec, B. Felson, S. Rosenbaum, J. B. Keller, and P. Ckw. Reflection and transmission by a random medium. *Radio Science*, 4(11):1067–1077, November 1969.
- [44] R. J. LeVeque. Wave propagation algorithms for multi-dimensional hyperbolic systems. *J. Comput. Phys.*, 131:327–353, 1997.
- [45] A. P. Lyons, A. L. Anderson, and F. S. Dwan. Acoustic scattering from the seafloor: Modeling and data comparison. *J. Acoust. Soc. Am.*, 99:866–879, February 1996.
- [46] P. L. MaCall and M. J. S. Tevesz. *Animal-Sediment Relations - The Biogenic Alteration of Sediment*. Plenum Press, New York, 1982.

- [47] J. E. Moe. Near and Far-Field Acoustic Scattering through and from Two Dimensional Fluid-Fluid Rough Interfaces. Technical Report APL-UW TR 9606, Applied Physics Laboratory, University of Washington, Seattle, WA, October 1996.
- [48] P. D. Mourad and D. R. Jackson. High frequency sonar equation models for bottom backscatter and forward loss. In *Proceedings of OCEAN '89*, pages 1168-1175, New York, September 1989. IEEE.
- [49] P. D. Mourad and D. R. Jackson. A model/data comparison for low-frequency bottom backscatter. *J. Acoust. Soc. Am.*, 94:344-358, July 1993.
- [50] W. Munk and C. Wunsch. Ocean acoustic tomography: a scheme for large scale monitoring. *Deep-Sea Res.*, 26:123-161, 1979.
- [51] M. H. Orr and D. C. Rhoads. Acoustic imaging of structure in the upper 10 cm of sediment using a megahertz backscattering system: preliminary results. *Mar. Geol.*, 46:117-129, 1982.
- [52] T. H. Orsi, M. E. Duncan, A. P. Lyons, K. B. Briggs, M. D. Richardson, and A. L. Anderson. High-resolution characterization of seafloor sediments for modeling acoustic backscatter. In *High Frequency Acoustics in Shallow Water*, pages 409-415, Lerici, Italy, 1997. NATO SACLENT Undersea Research Center.
- [53] T. H. Orsi, C. M. Edwards, and A. L. Anderson. X-rays computed tomography: a nondestructive method for quantitative analysis of sediment cores. *Jour. Sed. Res.*, A64:690-693, 1994.
- [54] P. M. Morse and K. U. Ingard. *Theoretical Acoustics*. Princeton University Press, New Jersey, 1968.

- [55] A. Papoulis. *Probability, Random Variables, and Stochastic Processes*. McGraw-Hill, New York, 1991.
- [56] V. R. Paul, R. Snelgrove, and C. A. Butman. Animal-sediment relationships revisited: cause versus effect. In *Oceanography and Marine Biology: An Annual Review*, volume 32, pages 111–177. UCL Press, 1994.
- [57] A. F. Peterson, S. L. Ray, and R. Mittra. *Computational Methods for Electromagnetics*. IEEE Press and Oxford University Press, New York, 1998.
- [58] W. H. Press, B. P. Flannery, S. A Teukolsky, and W. T. Vetterling. *Numerical recipes in C, Second Edition*. Cambridge University Press, 1992.
- [59] J. Proakis and D. Manolakis. *Digital Signal Processing*. Macmillan Publishing Company, New York, 1992.
- [60] M. D. Richardson and K. B. Briggs. *In situ* and laboratory geoacoustic measurements in soft mud and hard-packed sand sediments: Implications for high-frequency acoustic propagation and scattering. *Geo-Marine Lett.*, 16:196–203, 1996.
- [61] P. A. Rona, D. R. Jackson, T. Wen, C. D. Jones, K. Mitsuzawa, and K. G. Bemis. Acoustic mapping of diffuse flow at a seafloor hydrothermal site: Monolith Vent, Juan de Fuca Ridge. *Geophys. Res. Lett.*, 24(19):2351–2354, 1997.
- [62] P. A. Rona, D. R. Palmer, C. D. Jones, D. A. Chayes, M. Czarnecki, E. W. Carey, and J. C. Guerrero. Acoustic imaging of hydrothermal plumes: East Pacific Rise 21N, 109W. *Geophys. Res. Lett.*, 18(12):2233–2236, 1991.
- [63] S. Rosenbaum. On the coherent wave motion in bounded, randomly fluctuating regions. *Radio Science*, 4(8):709–719, August 1969.

- [64] G. T. Rowe, G. Keller, H. Eggerton, N. Staresinic, and J. MacIlvaine. Time-lapse photography of the biological reworking of sediment in the hudson submarine canyon. *J. Sediment. Petrol.*, 44:549–552, 1974.
- [65] S. M. Rytov, Yu. A. Kravtsov, and V. I. Tartarskii. *Principles of Statistical Radiophysics 1, Elements of Random Process Theory*. Springer-Verlag, Berlin, 1989.
- [66] S. M. Rytov, Yu. A. Kravtsov, and V. I. Tartarskii. *Principles of Statistical Radiophysics 2*. Springer-Verlag, Berlin, 1989.
- [67] S. M. Rytov, Yu. A. Kravtsov, and V. I. Tartarskii. *Principles of Statistical Radiophysics 3, Elements of Random Fields*. Springer-Verlag, Berlin, 1989.
- [68] S. M. Rytov, Yu. A. Kravtsov, and V. I. Tartarskii. *Principles of Statistical Radiophysics 4, Wave Propagation Through Random Media*. Springer-Verlag, Berlin, 1989.
- [69] H. Sato and M. C. Fehler. *Seismic Wave Propagation and Scattering in the Heterogeneous Earth*. Springer-Verlag, New York, 1998.
- [70] C. R. Smith, P. A. Jumars, and J. DeMaster. In situ studies of megafaunal mounds indicate rapid sediment turnover and community response at the deep-sea floor. *Nature*, 323:251–253, 1986.
- [71] D. Sternlicht. *High Frequency Acoustic Remote Sensing of Seafloor Characteristics*. Doctoral Thesis, Scripps Institute of Oceanography, UCSD, La Jolla, CA, 1999.
- [72] R. Stoll. *Sediment Acoustics*. Springer, 1989.

- [73] D. Tang. A note on scattering by a stack of rough interfaces. *J. Acoust. Soc. Am.*, 99(3):1414-1418, March 1996.
- [74] D. Tang. Small scale volumetric inhomogeneities of shallow water sediments: measurements and discussion. In *High Frequency Acoustics in Shallow Water*, pages 539-546, Lerici, Italy, 1997. NATO SACLENT Undersea Research Center.
- [75] V. I. Tatarski and M. E. Gertsenshtein. Propagation of waves in a medium with strong fluctuation of the refractive index. *Soviet Physics, JETP*, 17(2), August 1963.
- [76] E. I. Thorsos. The validity of the Kichhoff approximation for rough surface scattering using a Gaussian roughness spectrum. *J. Acoust. Soc. Am.*, 83(1):79-92, January 1988.
- [77] E. I. Thorsos and D. R. Jackson. The validity of the perturbation approximation for rough surface scattering using a Gaussian roughness spectrum. *J. Acoust. Soc. Am.*, 86(1):261-277, July 1989.
- [78] L. Tsang, C. H. Chan, K. Pak, and H. Sangani. Monte-Carlo simulations of large-scale problems of random rough surface scattering and applications to grazing incidence with the BMIA/canonical grid methods. *IEEE Trans. Antennas Propagat.*, 43(8):851-859, August 1995.
- [79] L. Tsang and J. A. Kong. Wave theory for microwave remote sensing of a half-space random medium with three-dimensional variations. *Radio Science*, 14(3):359-369, May 1979.
- [80] L. Tsang, J. A. Kong, and R. T. Shin. *Theory of Microwave Remote Sensing*. Wiley Interscience, New York, 1985.

- [81] J. L. Volakis, A. Chatterjee, and L. C. Kempel. Review of the finite-element method for three-dimensional electromagnetic scattering. *J. Opt. Soc. Am.*, 11(4):1422–1433, April 1994.
- [82] R. A. Wheatcroft and P. A. Jumars. Personal correspondence. 1997.
- [83] R. A. Wheatcroft, P. A. Jumars, C. A. Smith, and A. R. Nowell. A Mechanistic view of particulate biodiffusion coefficient: Step lengths, rest periods and transport directions. *J. Mar. Res.*, 48:177–207, 1990.
- [84] R. A. Wheatcroft, C. A. Smith, and P. A. Jumars. Dynamics of surficial trace assemblages in the deep sea. *Deep-Sea Res.*, 36(1):71–91, 1989.
- [85] R. A. Wheatcroft, C. A. Smith, and P. A. Jumars. Temporal variation in bed configuration and one-dimensional bottom roughness at the mid-shelf STRESS site. *Cont. Shelf Res.*, 14:1167–1190, 1994.
- [86] K. L. Williams. Temporal fluctuations in the acoustic scattering from bottom deployed objects and localized biological treatments. *Submitted to J. Acoust. Soc. Am.*, 1999.
- [87] T. Yamamoto. Velocity variabilities and other physical properties of marine sediments measured by crosswell tomography. *J. Acoust. Soc. Am.*, 98:2235–2248, October 1995.
- [88] T. Yamamoto. Acoustic scattering in the ocean from velocity and density fluctuations in the sediment. *J. Acoust. Soc. Am.*, 99(2):866–879, February 1996.
- [89] N. P. Zhuck. Effective parameters of a statistically homogeneous fluid with strong density and compressibility fluctuations. *Phys. Rev. B*, 52(2):919–926, 1995.

- [90] N. P. Zhuck. Strong fluctuation theory for a mean acoustic field in a random fluid medium with statistically anisotropic perturbations. *J. Acoust. Soc. Am.*, 99(1):46-54, 1996.

Appendix A

HALF-SPACE GREEN'S FUNCTION

Consider a two-dimensional medium with a source at position $\mathbf{r}' = (x', z')$ and a receiver at position $\mathbf{r} = (x, z)$ both in the LHS of two homogeneous half-spaces. The Green's function is the solution of the wave equation,

$$[\nabla^2 + \bar{k}^2] g_0(\mathbf{r}, \mathbf{r}') = -\delta(\mathbf{r} - \mathbf{r}') , \quad (\text{A.1})$$

that satisfies reciprocity and the appropriate boundary conditions along the interface (at $z = 0$). The solution is found by first taking the Fourier transform in x to obtain the spectral representation of (A.1),

$$\left[\frac{\partial^2}{\partial z^2} + \beta^2 \right] \tilde{g}_0 = -\frac{1}{2\pi} e^{-ik_x x'} \delta(z - z') , \quad (\text{A.2})$$

where

$$\beta = \sqrt{\bar{k}^2 - k_x^2} . \quad (\text{A.3})$$

The solution for (A.2) in the region $z < 0$ and $z > z'$ is

$$\tilde{g}_0 = A [R(k_x) e^{-i\beta z} + e^{i\beta z}] ,$$

and in the region $z < 0$ and $z < z'$ is

$$\tilde{g}_0 = B e^{-i\beta z} .$$

The coefficient R is the reflection coefficient between the two regions:

$$R = \frac{\rho_0 \beta - \bar{\rho} \beta_0}{\rho_0 \beta + \bar{\rho} \beta_0} . \quad (\text{A.4})$$

The unknown coefficients A and B are found by matching the solutions and imposing the discontinuity in the normal derivative at $z = z'$ required by (A.2), such that

$$A \left[R(k_x) e^{-i\beta z'} + e^{i\beta z'} \right] = B e^{-i\beta z'}$$

and

$$i\beta A \left[-R(k_x) e^{-i\beta z'} + e^{i\beta z'} \right] + i\beta B e^{-i\beta z'} = -\frac{1}{2\pi} e^{-ik_x x'}$$

Solving for A and B ,

$$A = \frac{i}{4\pi\beta} e^{-ik_x x'} e^{-i\beta z'}$$

and

$$B = \frac{i}{4\pi\beta} e^{-ik_x x'} \left[R(k_x) e^{-i\beta z'} + e^{i\beta z'} \right],$$

the combined solution for the entire region $z < 0$ is

$$\tilde{g}_0 = -\frac{i}{4\pi\beta} e^{-ik_x x'} \left[R(k_x) e^{-i\beta(z+z')} + e^{i\beta|z-z'|} \right].$$

The final solution is found by taking an inverse Fourier transform in x :

$$g_0(\mathbf{r}; \mathbf{r}') = \frac{i}{4\pi} \int_{-\infty}^{\infty} \frac{dk_x}{\beta} e^{ik_x(x-x')} \left[R(k_x) e^{i\beta(z+z')} + e^{i\beta|z-z'|} \right].$$

The Green's function for a receiver in the UHS ($z > 0$) and a source in the LHS ($z' < 0$) is found in a similar manner. The solution for (A.2) in the region $z > 0$ is

$$\tilde{g}_0 = C e^{i\beta_0 z},$$

where

$$\beta_0 = \sqrt{k_0^2 - k_x^2}. \quad (\text{A.5})$$

Again, solve for the unknown coefficients C by matching the solutions and their derivatives at $z = 0$, such that

$$C = A(R + 1) = AT',$$

and

$$\frac{i\beta_0}{\rho_0}C = \frac{i\beta}{\bar{\rho}}A(1 - R).$$

The coefficient T' is the transmission coefficient from the LHS to the UHS:

$$T' = \frac{2\rho_0\beta}{\rho_0\beta + \bar{\rho}\beta_0}. \quad (\text{A.6})$$

Using the derivation of A from the reflection Green's function above, the solution for the spectral component of the transmission Green's function is

$$\tilde{g}_0 = \frac{i}{4\pi\beta}T'(k_x)e^{ik_x x'}e^{i\beta_0 z - i\beta z'}.$$

The final solution is found by performing an inverse Fourier transform is

$$g_0(\mathbf{r}; \mathbf{r}') = \frac{i}{4\pi} \int_{-\infty}^{\infty} \frac{dk_x}{k_z} T'(k_x) e^{ik_x(x-x')} e^{i\beta_0 z - i\beta z'}.$$

Appendix B

FAR-FIELD HALF-SPACE GREEN'S FUNCTION

The half-space Green's function is evaluated in the far-field of the interface using the method of stationary phase or saddle-point method [29]. Begin with the two-dimensional Green's function for transmission

$$g_0(\mathbf{r}, \mathbf{r}') = \frac{i}{4\pi} \int_{-\infty}^{\infty} \frac{T'(k_x)}{\beta} e^{i\beta_0 z - i\beta z'} e^{ik_x(x-x')} dk_x, \quad (\text{B.1})$$

where

$$\begin{aligned} \beta &= \sqrt{\bar{k}^2 - k_x^2}, \\ \beta_0 &= \sqrt{k_0^2 - k_x^2}, \end{aligned} \quad (\text{B.2})$$

and

$$T' = \frac{2\rho_0\beta}{\rho_0\beta + \bar{\rho}\beta_0}. \quad (\text{B.3})$$

Change integration variable in (B.1) to cylindrical coordinates with $k_x = k_0 \cos \theta$ and $\beta_0 = k_0 \sin \theta$, and define the the position $\mathbf{r} = (x, z)$ as $x = r \cos \theta_s$ and $z = r \sin \theta_s$. Then using the identity

$$\cos(\theta - \theta_s) = \cos(\theta) \cos(\theta_s) + \sin(\theta) \sin(\theta_s), \quad (\text{B.4})$$

the integral (B.1) can be rewritten as

$$g_0(\mathbf{r}, \mathbf{r}') = \frac{i}{4\pi} \int_C F(\theta) e^{f(\theta)r} d\theta. \quad (\text{B.5})$$

The complex contour C is defined in Figure B.1. The function $F(\theta)$ is defined as

$$F(\theta) = -\frac{T'(\theta)}{\beta} e^{-ik_0 x' \cos \theta - ik_0 z' \sin \theta} k_0 \sin \theta, \quad (\text{B.6})$$

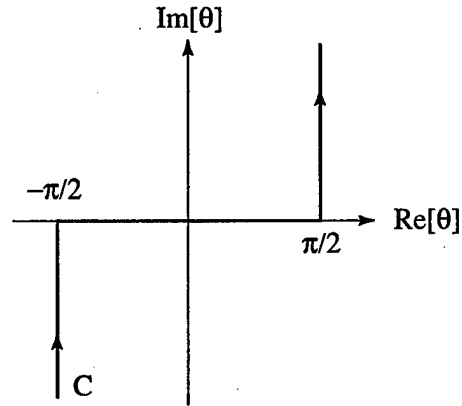


Figure B.1: Complex contour in the θ plane.

and the exponent function $f(\theta)$ is defined as

$$f(\theta) = ik_0 \cos(\theta - \theta_s) . \quad (\text{B.7})$$

It can be shown that the integrand vanishes at both ends of the contour [29].

The stationary phase point is given by

$$\frac{\partial f(\theta)}{\partial \theta} = -ik_0 \sin(\theta - \theta_s) = 0, \quad (\text{B.8})$$

or $\theta = \theta_s$. The function $f(\theta)$ is then expanded about θ_s as

$$f(\theta) = f(\theta_s) + \frac{(\theta - \theta_s)^2}{2} f''(\theta_s) , \quad (\text{B.9})$$

where the double primes denote the second derivative with respect to θ . The integrand can then be approximated as a Gaussian curve, which for large r can be evaluated. Evaluating the integral gives an approximate expression for the far-field,

$$g_0(\mathbf{r}, \mathbf{r}') = \frac{i}{4\pi} F(\theta_s) e^{rf(\theta_s) + i\gamma} \left[\frac{2\pi}{|f''(\theta_s)|r} \right]^{1/2} , \quad (\text{B.10})$$

where $\gamma = -\pi/4$ is chosen to properly orient the path of integration in the complex plane.

The far-field Green's function is then written as

$$g_0(\mathbf{r}, \mathbf{r}') = -\frac{i\bar{k} \sin \theta_s}{\beta} \frac{T'(\theta_s)}{\sqrt{8\pi k_0 r}} e^{ik_0 r} e^{-i\mathbf{k}_s \cdot \mathbf{r}'} e^{-i\pi/4}, \quad (\text{B.11})$$

or equivalently as

$$g_0(\mathbf{r}, \mathbf{r}') = -i \frac{\rho_0}{\rho} \frac{T(\theta_s)}{\sqrt{8\pi k_0 r}} e^{ik_0 r} e^{-i\mathbf{k}_s \cdot \mathbf{r}'} e^{-i\pi/4}, \quad (\text{B.12})$$

where

$$T = \frac{2\bar{\rho}\beta_0}{\rho_0\beta + \bar{\rho}\beta_0}. \quad (\text{B.13})$$

The same procedure is performed to find the three-dimensional far-field Green's function:

$$g_0(\mathbf{r}, \mathbf{r}') = \frac{\rho_0}{\rho} \frac{T(\theta_s)}{4\pi r} e^{ik_0 r} e^{-i\mathbf{k}_s \cdot \mathbf{r}'} . \quad (\text{B.14})$$

Appendix C

AUTO-REGRESSIVE SPECTRAL ESTIMATION

Auto-regressive spectral estimation is based on modeling the digital data sequence, $y(n)$, as the output of a linear system,

$$y(n) = h(n) * x(n) , \quad (\text{C.1})$$

characterized by the rational system function

$$H(z) = \frac{1}{A(z)} = \left[1 + \sum_{k=1}^p \hat{a}_k z^{-k} \right]^{-1} . \quad (\text{C.2})$$

If the input and output of the system are stationary random processes, the auto-correlation of the data sequence is defined in terms of the input auto-correlation and the discrete step response of the system:

$$R_{yy}(m) = R_{xx}(m) * h(m) * h^*(-m) . \quad (\text{C.3})$$

Using an estimate of $R_{yy}(m)$ taken from the data and assuming the input is a zero-mean white noise process with auto-correlation $R_{xx}(m) = q\delta(m)$, determining the spectrum of the output process becomes a problem of estimating the coefficients a_k . The constant q is the variance of the input process. Several well known techniques such as the Yule-Walker method and the Levinson-Durbin algorithm can be used to estimate these parameters [59] [55]. With an estimate of the system function (or system filter coefficients), the spectrum of the output process is found by evaluating equation (C.2) on the unit circle,

$$S_{yy}(k) = q |H(z)|^2 , \quad (\text{C.4})$$

where $z = e^{ik}$ and k is the spatial frequency.

A first-order AR process is characterized by a system function with a single pole

$$H(z) = \frac{1}{1 - \hat{a}z^{-1}}. \quad (\text{C.5})$$

For $\hat{a} < 1$ the impulse response function of this system is

$$h(n) = \hat{a}^n u(n). \quad (\text{C.6})$$

The auto-correlation of this process is found using equations (C.3) and (C.6) to be

$$R_{yy}(m) = \frac{q}{1 - \hat{a}^2} \hat{a}^{|m|}. \quad (\text{C.7})$$

The normalized auto-correlation function is

$$r_{yy}(m) = \hat{a}^{|m|} = e^{-|m| \ln \hat{a}}. \quad (\text{C.8})$$

In general, we want to consider the correlation function of a continuous process in 3-D space. Thus, if we generalize equation (C.7) to represent an isotropic process in which $m = r = \sqrt{x^2 + y^2 + z^2}$ and apply the Wiener-Khinchin theorem [30], the spatial spectrum of a first-order AR process is found to be

$$S_{yy}(k) = \frac{\alpha\beta/\pi^2}{(\alpha^2 + k^2)^2}, \quad (\text{C.9})$$

where $\alpha = -\ln \hat{a}/\delta m$, $\beta = q/(1 - \hat{a}^2)$, and δm is the sampling interval.

How does this relate to power law spectrum of normalized sediment density fluctuations derived from an exponential correlation function (as in Section 2.1.1)? By the definition of (C.8), $\alpha = 1/l_c$. The variance of the normalized sediment density fluctuations is simply the variance of the input process, $\sigma_p^2 = q/(1 - \hat{a}^2)$. Thus, equation (C.9) can be written as

$$S_{yy}(k) = \frac{\sigma_p^2}{\pi^2 l_c (1/l_c + k^2)^2}. \quad (\text{C.10})$$

Appendix D

FFT EVALUATION OF THE HALF-SPACE GREEN'S FUNCTION

Since the unknown field points are discretized on a uniform grid, the wavenumber integration of the half-space Green's function (2.33) can be performed efficiently using an FFT [38]. First, use the discretization of the x -coordinate,

$$x_n = x_{min} + n\Delta x, \text{ for } n = 1, 2, \dots, N, \quad (\text{D.1})$$

to define the corresponding discretized wavenumber in the x -direction,

$$k_{xm} = k_{x,min} + m\Delta k_x, \text{ for } m = 1, 2, \dots, M, \quad (\text{D.2})$$

where

$$\Delta x \Delta k_x = \frac{2\pi}{M}. \quad (\text{D.3})$$

Substituting x_n and k_{xm} into the definition of the half-space Green's function for reflection and approximating the wavenumber integration as a summation,

$$\int dk_x \approx \sum \Delta k_x, \quad (\text{D.4})$$

the Green's function is rewritten as

$$g_0(x_n, z_n; x', z') = \frac{i}{4\pi} \sum_{m=0}^{\infty} \frac{\Delta k_x}{\beta_m} [R(k_{xm}) e^{i\beta_m |z_n + z'|} + e^{i\beta_m |z_n - z'|}] e^{im\Delta k_x (x_{min} - x')} e^{i2\pi \frac{mn}{M}}. \quad (\text{D.5})$$

With attenuation in the medium, the term in square brackets will vanish at high wavenumbers and the summation can be truncated. The summation now takes the

form of an inverse FFT,

$$g_0(x_n, z_n; x', z') = \frac{iM}{2L} \text{FFT}^{-1} \left[\frac{1}{\beta_m} [R(k_{xm}) e^{i\beta_m |z_n + z'|} + e^{i\beta_m |z_n - z'|}] e^{im\Delta k_x (x_{min} - x')} \right], \quad (\text{D.6})$$

where

$$\text{FFT}^{-1} [F(x_n, z_n)] = \frac{1}{M} \sum_{m=0}^{M-1} F(x_n, z_n) e^{i2\pi \frac{mn}{M}}. \quad (\text{D.7})$$

The computation of the Green's function is greatly improved. A single FFT computation is required to find a row of values. The discretization spacing in the x -direction must be chosen to provide adequate spacing in the spectral domain to fully represent the spatial frequency characteristics of the integrand. If Δx or M is too small, aliasing may corrupt the FFT. Owing to the assumed periodicity of the FFT, the range over which the function F is evaluated must be sufficiently large so that F approximately vanishes outside the interval.

Appendix E

GENERATING GAUSSIAN RANDOM MEDIA

Realizations of a two-dimensional Gaussian random medium are generated by discrete inverse Fourier transforms. Consider the random variable $f(x, z)$ and the discrete Fourier transform

$$f(x, z) = \frac{(2\pi)^2}{L_x L_z} \sum_m \sum_n b_{mn} e^{ik_{zm}z} e^{ik_{xn}x}, \quad (\text{E.1})$$

where $k_{zm} = 2\pi m/L_z$ and $k_{xn} = 2\pi n/L_x$. The correlation of $f(x, z)$ is defined as

$$R_{ff}(x_1 - x_2, z_1 - z_2) = \langle f(x_1, z_1) f^*(x_2, z_2) \rangle. \quad (\text{E.2})$$

If $f(x, z)$ is a Gaussian random variable, then the coefficients b_{mn} are independent and uncorrelated, and they can be defined as the Gaussian random variable

$$b_{mn} = \frac{A_{mn}}{\sqrt{2}} [N(0, 1) + iN(0, 1)], \quad (\text{E.3})$$

where A_{mn} is the amplitude. The function $N(0, 1)$ is a uncorrelated Gaussian random number with zero mean and unit variance, such as a numerical random number generator. Using (E.1) the correlation of $f(x, z)$ can be rewritten as

$$R_{ff}(x_1 - x_2, z_1 - z_2) = \frac{(2\pi)^4}{(L_x L_z)^2} \sum_m \sum_n B_{mn} e^{ik_{zm}(z_1 - z_2)} e^{ik_{xn}(x_1 - x_2)}, \quad (\text{E.4})$$

where

$$B_{mn} = \langle |b_{mn}|^2 \rangle. \quad (\text{E.5})$$

The correlation of $f(x, z)$ is alternatively expressed as the discrete Fourier transform of the spectrum of the process that generated $f(x, z)$:

$$R_{ff}(x_1 - x_2, z_1 - z_2) = \frac{4\pi^2}{L_x L_z} \sum_m \sum_n S_{ff}(k_{xn}, k_{zm}) e^{ik_{zm}(z_1 - z_2)} e^{ik_{xn}(x_1 - x_2)}. \quad (\text{E.6})$$

Equating (E.6) and (E.4), the random Fourier coefficients of the correlation function are related to the spectrum as

$$B_{mn} = \frac{L_x L_z}{(2\pi)^2} S_{ff}(k_{xn}, k_{zm}) . \quad (\text{E.7})$$

Now, using (E.3) and (E.5) in (E.7), the amplitudes of the random Fourier coefficients of $f(x, z)$ are found to be

$$A_{mn} = \frac{1}{(2\pi)} \sqrt{L_x L_z S_{ff}(k_{xn}, k_{zm})} . \quad (\text{E.8})$$

Using a desired spectrum for S_{ff} , such as the power-law spectrum (2.18), and generating the Fourier coefficients using (E.3) and (E.8), a random realization of $f(x, z)$ can be generated by performing the inverse Fourier transform. A discrete random realization, $f(x_i, z_j)$, is found by discretizing the finite region (L_x, L_z) as a uniform grid and performing the inverse transform at the grid locations:

$$f(x_i, z_j) = \frac{(2\pi)^2}{L_x L_z} \sum_m \sum_n b_{mn} e^{ik_{zm}z_j} e^{ik_{zn}x_i} . \quad (\text{E.9})$$

Appendix F

MASS OPERATOR FOR THE BILOCAL APPROXIMATION

The mass operator for Dyson's equation using the bilocal approximation (4.17) is defined in the wavenumber domain as

$$M(\mathbf{k}) = \bar{k}^4 M_{\kappa\kappa}(\mathbf{k}) - 2i\bar{k}^2 \mathbf{k} \cdot \mathbf{M}_{\kappa\rho}(\mathbf{k}) - \mathbf{k} \cdot \mathbf{M}_{\rho\rho}(\mathbf{k}) \cdot \mathbf{k}, \quad (\text{F.1})$$

where

$$M_{\kappa\kappa}(\mathbf{k}) = \mu^2 \int C_{\rho\rho}(\mathbf{r}) g_0(\mathbf{r}) e^{-i\mathbf{k}\cdot\mathbf{r}} d\mathbf{r}, \quad (\text{F.2})$$

$$\mathbf{M}_{\kappa\rho}(\mathbf{k}) = \mu \int C_{\rho\rho}(\mathbf{r}) \nabla g_0(\mathbf{r}) e^{-i\mathbf{k}\cdot\mathbf{r}} d\mathbf{r}, \quad (\text{F.3})$$

and

$$\mathbf{M}_{\rho\rho}(\mathbf{k}) = \int C_{\rho\rho}(\mathbf{r}) \nabla \nabla g_0(\mathbf{r}) e^{-i\mathbf{k}\cdot\mathbf{r}} d\mathbf{r}. \quad (\text{F.4})$$

Using the free space Green's function

$$g_0(\mathbf{r}) = \frac{e^{i\bar{k}r}}{4\pi r} \quad (\text{F.5})$$

with an isotropic and exponential correlation function

$$C_{\rho\rho}(\mathbf{r}) = \sigma_\rho^2 e^{-|\mathbf{r}|/l_c}, \quad (\text{F.6})$$

each mass operator can be derived analytically.

The integrals of (F.2-F.4) are solved by changing integration variables to spherical coordinates and orienting \mathbf{k} in the z -direction, so that $\mathbf{k} \cdot \mathbf{r} = kru$ and $u = \cos \theta$.

Since there is only one wave vector \mathbf{k} in (F.1), and it is pointed in the z -direction, only the z -component of the vector $\mathbf{M}_{\kappa\rho}$ and the zz -component of the dyad $\mathbb{M}_{\rho\rho}$ are considered. Therefore, equations (F.2) and (F.3) are rewritten as

$$M_{\kappa\kappa}(\mathbf{k}) = \frac{\mu^2 \sigma_\rho^2}{2} \int_0^\infty \int_{-1}^1 e^{-(1/l_c - i\bar{k} + iku)r} r dr du \quad (\text{F.7})$$

and

$$\mathbf{k} \cdot \mathbf{M}_{\kappa\rho}(\mathbf{k}) = \frac{\mu k \sigma_\rho^2}{2} \int_0^\infty \int_{-1}^1 [i\bar{k}r - 1] e^{-(1/l_c - i\bar{k} + iku)r} u du dr, \quad (\text{F.8})$$

using

$$\frac{\partial}{\partial z} = \frac{\partial r}{\partial z} \frac{\partial}{\partial r} = u \frac{\partial}{\partial r}. \quad (\text{F.9})$$

Through integration by parts, the dyadic mass operator (F.4) is rewritten as

$$\begin{aligned} \mathbf{k} \cdot \mathbb{M}_{\rho\rho}(\mathbf{k}) \cdot \mathbf{k} &= \left[k^2 C_{\rho\rho}(\mathbf{r}) e^{-i\mathbf{k} \cdot \mathbf{r}} \frac{\partial}{\partial z} g_0(\mathbf{r}) \right]_{-\infty}^{\infty} \\ &\quad - k^2 \int \frac{\partial}{\partial z} [C_{\rho\rho}(\mathbf{r}) e^{-i\mathbf{k} \cdot \mathbf{r}}] \frac{\partial}{\partial z} g_0(\mathbf{r}) dr, \end{aligned} \quad (\text{F.10})$$

which after applying the radiation condition and spherical coordinates, is rewritten as

$$\mathbf{k} \cdot \mathbb{M}_{\rho\rho}(\mathbf{k}) \cdot \mathbf{k} = \frac{k^2 \sigma_\rho^2}{2l_c} \int_0^\infty \int_{-1}^1 [i\bar{k}r - 1] [u + ikl_c] e^{-(1/l_c - i\bar{k} + iku)r} u du dr. \quad (\text{F.11})$$

The integration on r and u in all three integrals can now be performed to obtain

$$M_{\kappa\kappa}(\mathbf{k}) = \mu^2 \frac{\sigma_\rho^2 l_c^2}{a^2 - b^2}, \quad (\text{F.12})$$

$$\mathbf{k} \cdot \mathbf{M}_{\kappa\rho}(\mathbf{k}) = \mu \frac{\sigma_\rho^2 k l_c}{2b^2} \left[i\bar{k} l_c \left(c - \frac{2ab}{a^2 - b^2} \right) - (2b - ac) \right], \quad (\text{F.13})$$

and

$$\begin{aligned} \mathbf{k} \cdot \mathbb{M}_{\rho\rho}(\mathbf{k}) \cdot \mathbf{k} &= \frac{\sigma_\rho^2 k^2}{2b^3} \left[i\bar{k} l_c \left[(2b - ac) - (a - b^2) \left(c - \frac{2ab}{a^2 - b^2} \right) \right] \right. \\ &\quad \left. + (2b - ac)(a - b^2) \right], \end{aligned} \quad (\text{F.14})$$

where

$$\begin{aligned} a &= 1 - i\bar{k}l_c, \\ b &= ikl_c, \\ c &= \ln[(a + b)/(a - b)]. \end{aligned} \tag{F.15}$$

REPORT DOCUMENTATION PAGE

Form Approved
OPM No. 0704-0188

Public reporting burden for this collection of information is estimated to average 1 hour per response, including the time for reviewing instructions, searching existing data sources, gathering and maintaining the data needed, and reviewing the collection of information. Send comments regarding this burden estimate or any other aspect of this collection of information, including suggestions for reducing this burden, to Washington Headquarters Services, Directorate for Information Operations and Reports, 1215 Jefferson Davis Highway, Suite 1204, Arlington, VA 22202-4302, and to the Office of Information and Regulatory Affairs, Office of Management and Budget, Washington, DC 20503.

1. AGENCY USE ONLY (Leave blank)		2. REPORT DATE October 1999	3. REPORT TYPE AND DATES COVERED Technical	
4. TITLE AND SUBTITLE High-Frequency Acoustic Volume Scattering from Biologically Active Marine Sediments			5. FUNDING NUMBERS N00014-98-1-0040	
6. AUTHOR(S) Christopher D. Jones				
7. PERFORMING ORGANIZATION NAME(S) AND ADDRESS(ES) Applied Physics Laboratory University of Washington 1013 NE 40th Street Seattle, WA 98105-6698			8. PERFORMING ORGANIZATION REPORT NUMBER APL-UW TR 9903	
9. SPONSORING / MONITORING AGENCY NAME(S) AND ADDRESS(ES) Office of Naval Research 800 N. Quincy Street Arlington, VA 22217-5660			10. SPONSORING / MONITORING AGENCY REPORT NUMBER	
11. SUPPLEMENTARY NOTES				
12a. DISTRIBUTION / AVAILABILITY STATEMENT Approved for public release; distribution is unlimited.			12b. DISTRIBUTION CODE	
13. ABSTRACT (Maximum 200 words) A thesis on high-frequency acoustic volume scattering from marine sediments with application to remote sensing of benthic biological activity is presented. Small perturbation theory is used to describe bistatic volume scattering in a sediment half-space. The sediment is modeled as an acoustic fluid with random fluctuations in density and compressibility. Insight into determining whether single or multiple scattering is significant in the medium is gained by using the bilocal approximation to Dyson's equation. An alternative analysis of volume scattering is made using exact numerical simulations, and a numerical method for two-dimensional volume scattering using the method of moments is presented. Both periodic and nonperiodic random media are considered. Scattering theory is compared with numerical Monte Carlo simulations, and the validity of the small perturbation method is discussed. The effects of the half-space scattering geometry on the coherent field within the sediment and on the bistatic scattering cross section are investigated. Benthic biological activity creates temporal and spatial variations in the sediment physical properties that result in temporal and spatial variations in sediment volume scattering. This acoustic variability is used as a remote sensing tool to infer parameters of biological activity, or bioturbation. To develop a forward model that relates bioturbation to density fluctuations in the sediment and, therefore, to acoustic scattering, a new stochastic model of bioturbation is presented that describes biological mixing as an inhomogeneous (two scale) biodiffusion process. Nonlocal mixing (due to macrofauna) is described as a filtered Poisson process, and local mixing (due to meiofauna) is described as diffusive. Modeling issues such as the spatial stationarity of bioturbation are discussed. The bioturbation and acoustic scattering models are then combined to produce a model for the decorrelation in time of acoustic backscatter. Model predictions are compared with experimental data collected over a two month period during the Orcas Island experiment. The observed decorrelation of acoustic backscattering at the Orcas site is compared to model predictions of temporal decorrelation, and the feasibility of using acoustic remote sensing to detect and study benthic biological activity is discussed.				
14. SUBJECT TERMS Volume scattering, method of moments, bioturbation, small perturbation theory, multiple scattering, half-space effects, remote sensing of benthic biological activity, bilocal approximation			15. NUMBER OF PAGES 193	
			16. PRICE CODE	
17. SECURITY CLASSIFICATION OF REPORT Unclassified	18. SECURITY CLASSIFICATION OF THIS PAGE Unclassified	19. SECURITY CLASSIFICATION OF ABSTRACT Unclassified	20. LIMITATION OF ABSTRACT SAR	